Molecular Level Understanding of Interfaces and Excited State Electronic Structure in Organic Solar Cells Using Soft X-ray Techniques

Matthew Gliboff

A dissertation submitted in partial fulfillment of the requirements for the degree of Doctor of Philosophy, University of Washington 2013

Reading Committee:

David S. Ginger, Chair

Gerald T. Seidler

Marjorie A. Olmstead

Program Authorized to Offer Degree:

Physics

University of Washington

Abstract

Molecular Level Understanding of Interfaces and Excited State Electronic Structure in Organic Solar Cells Using Soft X-ray Techniques

Matthew Gliboff

Chair of the Supervisory Committee:

David S. Ginger, Professor and Lawton Distinguished Scholar

Department of Chemistry

Transparent conductive oxides like indium tin oxide (ITO) are common substrates for optoelectronic devices, including organic light emitting diodes and organic solar cells. Tailoring the interface between the oxide and the active layer by adjusting the work function or wettability of the oxide can improve the performance of these devices in both emissive and photovoltaic applications. Molecular design of self-assembled monolayers (SAMs) allows for a range of surface properties using the same oxide material. The molecular ordering and conformation adopted by the SAMs determine properties such as work function and wettability at these critical interfaces. I use angle-dependent near edge x-ray absorption fine structure (NEXAFS) spectroscopy, to determine the molecular orientations of a variety of dipolar phosphonic acid surface modifiers. For a model system, phenylphosphonic acid on indium zinc oxide, the SAMs prove to be surprisingly well-oriented, with the phenyl ring adopting a well-defined tilt angle of 12-16° from the surface normal. The NEXAFS results agree with polarization modulation infrared reflection absorption spectroscopy (PM-IRRAS) results and orientations calculated from density functional theory (DFT). These results not only provide a detailed picture of the

molecular structure of a technologically important class of SAMs, but they also resolve a long-standing ambiguity regarding the vibrational-mode assignments for phosphonic acids on oxide surfaces, thus improving the utility of PM-IRRAS for future studies.

The effect of fluorination on the orientation of these phosponic-acid SAMs is non-trivial, due to the combined effects of the fluorination on binding mode and steric packing. The latter effects are found to be more dominant in aliphatic SAMs, leading to a more upright orientation in the fluorinated SAM. In the aromatic case, the fluorinated SAM adopted a less upright orientation which I attribute to changes in binding mode.

The relationship between structure and performance in active layer polymers for organic electronics is not yet well understood. To gain insight into the effect of the excited state electronic structure on device performance, we examine two similar donor-acceptor polymers: PCPDTBT and PCDTBT, which produce devices with internal quantum efficiency (IQE) of 70% and 100% respectively. We use time-dependent density functional theory (TD-DFT) in combination with near edge x-ray absorption fine structure (NEXAFS) and resonant Auger spectroscopy to predict the electronic structure of the lowest unoccupied molecular orbital (LUMO). The resonant Auger results are found to be independent of film morphology and likely dominated by monomer structure. We show that the degree of LUMO localization onto the benzothiadiazole acceptor group in each polymer is similar, indicating that that the differences in IQE between these two polymers are driven by larger-scale morphology and not explained by the electronic structure of the excited state.

Acknowledgements

I am grateful to Prof. David S. Ginger and Gerald T. Seidler for their advisement. This work would not have been possible without my collaborators: Kristina M. Knesting, Dana Sulas and Dane W. de Quilettes here at UW; Anthony J. Giordano and Hong Li at Georgia Institute of Technology; and Lingzi Sang at University of Arizona. NEXAFS and resonant Auger measurements were carried out under the helpful guidance of Dennis Nordlund at beamlines 8-2 and 10-1 at Stanford Synchrotron Radiation Lightsource, a national user facility operated by Stanford University on behalf of the U.S. Department of Energy, Office of Basic Energy Sciences. I am also grateful to Prof. Brandi M. Cossairt and Prof. James M. Mayer for discussions of phosphonic acid chemistry. This research is supported in part by the Center for Interface Science: Solar-Electric Materials (CIS:SEM), an Energy Frontier Research Center funded through the U.S. Department of Energy, Office of Science, Office of Basic Energy Sciences, under Award Number DE-SC0001084

Table of Contents

List of Figures

List of Tables

Chapter 1: Introduction

1.1 Statement of purpose

I was drawn to David Ginger's group due to my interests in sustainability and renewable energy. Throughout my time here, I have had the opportunity to work on materials related to organic solar cells (OSCs): a promising, low-cost solution for renewable energy.

The first goal of this dissertation is to address these issues related to charge extraction and energetic alignment of the electrodes. The electronic properties of the organic/electrode interface are crucial to achieving good charge extraction and the energy level alignments. The requirement for transparent and conductive electrodes limits the choice of materials, but this limitation can be circumvented using surface modifiers. I will explore the modification of ITO surfaces with phosphonic acid (PA) self-assembled monolayers (SAMs) with regards to the orientation that the molecules adopt on the ITO surface using near-edge x-ray absorption spectroscopy (NEXAFS) and discuss the impact of molecular orientation on achieving the desired surface properties such as work-function.

The second goal of this research is to examine the electronic structure of the excited state in the active layer of organic solar cell devices. Understanding the femtosecond details of exciton formation and charge extraction is critical to designing better active layer materials, but these details are still poorly understood. Using resonant Auger spectroscopy, I am able to probe the electronic structure of the excited state and compare with density functional theory (DFT) calculations.

1.2 Organic solar cells

Organic electronics are a subject of ongoing research for thin-film device applications. The primary benefit of using an organic material as an active layer are the low-cost solution processing and printing methods and the ease of chemically manipulating the material properties.[1, 2] The ubiquity and variety of plastics in our daily life is a demonstration of their cheap, easy production and their versatility. Currently, organic thin film transistors are used in flat-panel displays, radio frequency identification tags and sensing applications.[2-5] Organic light-emitting diodes(OLEDs) have seen commercial application in the form of active-matrix organic light-emitting diode (AMOLED) displays.[5-7] Organic solar cells (OSC) are a promising technology which has not yet achieved commercial viability. Using organic active-layer materials for power generation is currently limited by their low power generation efficiency and long-term stability issues.[1, 8] Current research is focused on achieving the landmarks of 10% power conversion efficiency outside of the lab and 10 year operational lifetime in real-world conditions to make devices suitable for commercial application.[9]

The power conversion efficiency for state-of-the art organic solar cells as of the time of this writing is about 7-9%, with the record devices achieving 11-12%.[9-11] These state-of-the-art cells use a blend of donor and acceptor materials in a bulk-heterojunction geometry. A typical acceptor would be a fullerene such as [6,6]-phenyl C_{71}-butyric acid methyl ester ($PC_{71}BM$) while a typical donor could be a low-bandgap semiconducting polymer such as poly[[4,8-bis[(2-ethylhexyl)oxy]benzo[1,2-b:4,5-b']dithiophene-2,6-diyl][3-fluoro-2-[(2-ethylhexyl)carbonyl]thieno[3,4-b]thiophenediyl]] (PTB7).[11] Figure 1.1 shows the geometry of a bulk-heterojunction solar cell and Figure 1.2 shows the various active layer materials referred to

in this dissertation. Power conversion efficiency is related to several factors, including how well the absorption of the active layer overlaps with the solar spectrum, the open circuit voltage and short-circuit current of the device, and the so-called fill-factor: a ratio of the peak power to the product of open-circuit voltage and short circuit current. These parameters are related to how well the device converts an absorbed photon to an extracted electron, a measure known as the internal quantum efficiency (IQE).

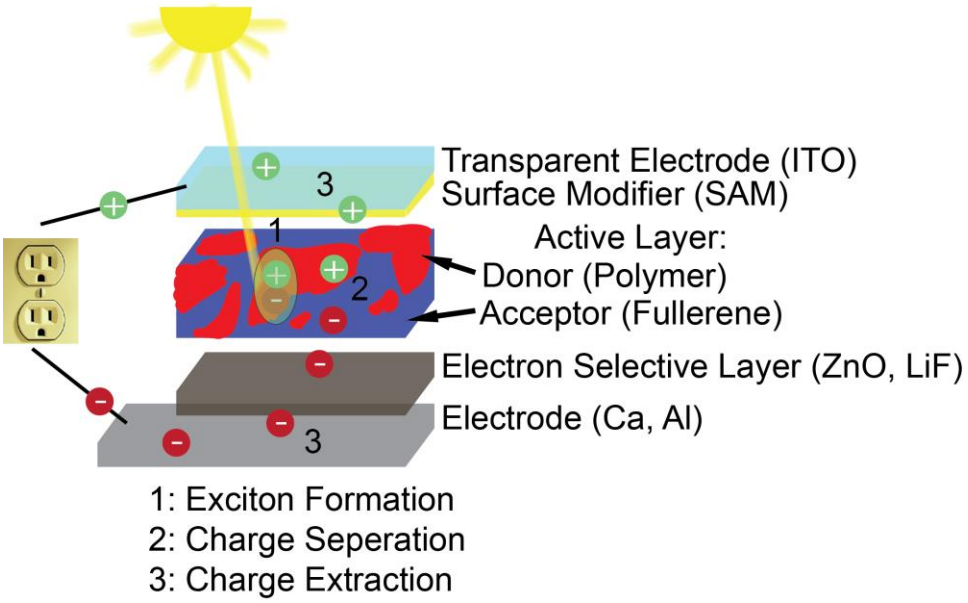

Figure 1.1. A cartoon of a bulk-heterojunction organic solar cell.

Unlike inorganic semiconductors, the primary photoexcitation of conjugated polymer semiconductors at room temperature are bound electron and hole pairs called excitons.[1, 9, 12] These excitons diffuse randomly for a few nanometers before they recombine but can undergo charge separation at the boundary between a donor material and an acceptor material.[13] The portion of the active layer within the exciton diffusion length of the donor-acceptor boundary is

the usable volume of the active layer; only photons absorbed in the usable volume can lead to free charges. The bulk-heterojunction geometry has a much greater usable volume as compared to a bilayer device, and therefore a much improved operating efficiency.[9] The thickness of bulk-heterojunctions remains a compromise between maximizing absorption, achieving exciton dissociation and maximizing charge extraction.

Most OSC active layers are deposited in solution and solvent, deposition conditions and post-processing steps (such as annealing) can lead to large variations in nanoscale morphology. Morphological properties, such as the size and type of polymer and fullerene phases present as well as the degree of phase segregation can impact charge carrier mobility and recombination rates, which in turn affect fill factor and photocurrent.[9, 14-17] For example, in P3HT-$PC_{61}BM$ devices, a highly aggregated fullerene phase, and a high degree of phase segregation were found to improve photocurrent dramatically, helping these blends to achieve 5% power conversion efficiency.[9]

The alignment of energy levels of the active layer materials and electrodes is also critical to achieving efficient devices. Open circuit voltage of an OSC is limited by the energy difference between the HOMO of the donor and the LUMO of the acceptor. The open-circuit voltage can be lower than this ideal due to charge extraction barriers at the contacts. Furthermore, the donor and acceptor domains of the heterojunction are not necessarily in contact with only the appropriate charge-extracting electrode. The presence of both domains at the electrodes leads to the potential for recombination losses at the electrodes. As a result, electrodes must have carefully chosen workfunctions and surface chemistry to achieve charge carrier selectivity, efficient charge extraction and good open-circuit voltage.[18, 19]

P3HT

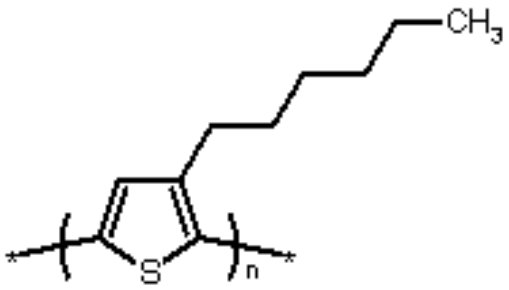

$PC_{61}BM$

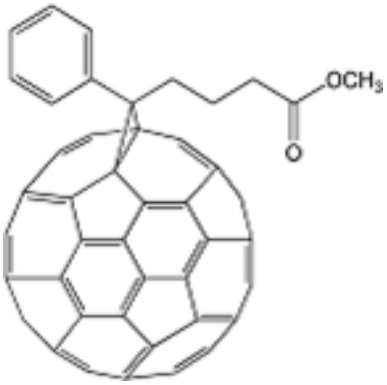

PTB7

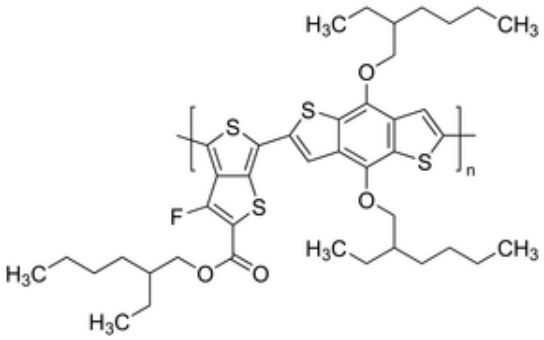

MDMO-PPV

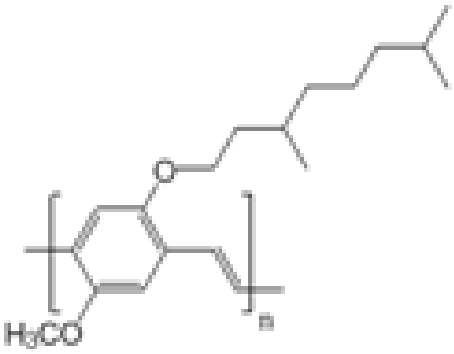

PCPDTBT

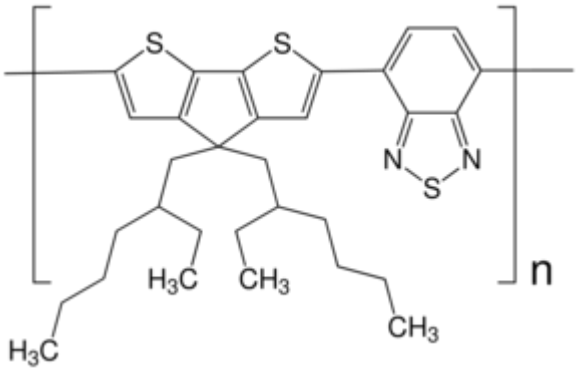

$PC_{71}BM$

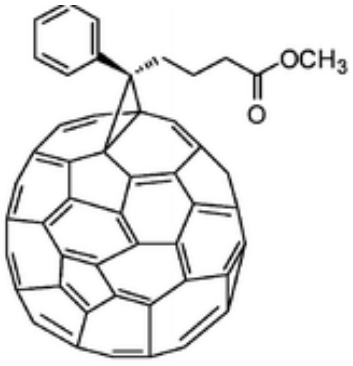

Figure 1.2. Examples of active layer materials for organic solar cells.

1.3 Interface modification

The interface between the active layer and the electrodes is critical for efficient organic electronics. The work function of the contacts partly determines the built-in voltage in an OSC; the built-in voltage provides the driving force for charge extraction.[20, 21] The work-function and surface chemistry also impact the efficiency of charge transport across the interface, the quality of the electrical contact and active-layer morphology.[15, 17, 22]

The most basic goal of interface design is to achieve charge carrier selectivity. In the bulk heterojunction geometry, both the donor and the acceptor are in contact with each electrode. The use of charge selective layers reduces recombination losses at the contacts and improves fill factor, short circuit current and power conversion efficiency.[23] Achieving charge selectivity depends on a rough alignment with the valence band of the donor (hole-selective) or the conduction band of the acceptor (electron-selective). PEDOT:PSS coated ITO is commonly used as a transparent hole-extracting contact[24, 25] while LiF coated metals form an electron-extracting contact.[26] Using ITO modified with self-assembled monolayers (SAMs) in place of PEDOT:PSS can lead to LED devices with higher operating efficiencies and longer operating lifetimes.[25] Other groups have used so-called inverted devices, with transparent electron selective contacts such as ZnO[27, 28] or ITO modified with a thin insulating polymer layer to achieve a low workfunction.[29]

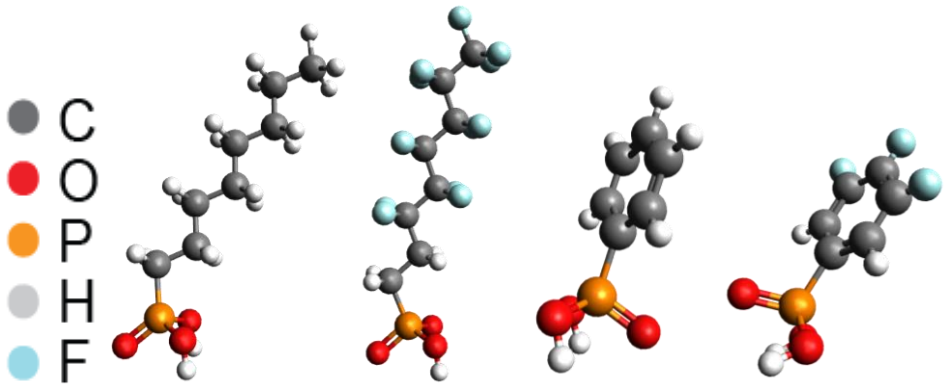

OPA F_{13}OPA PPA F_3PPA

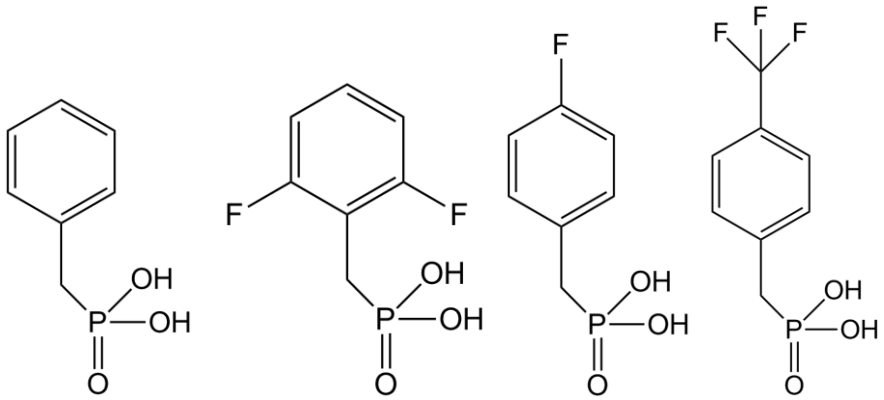

BnPA oF_2BnPA pFBnPA p(CF_3)BnPA

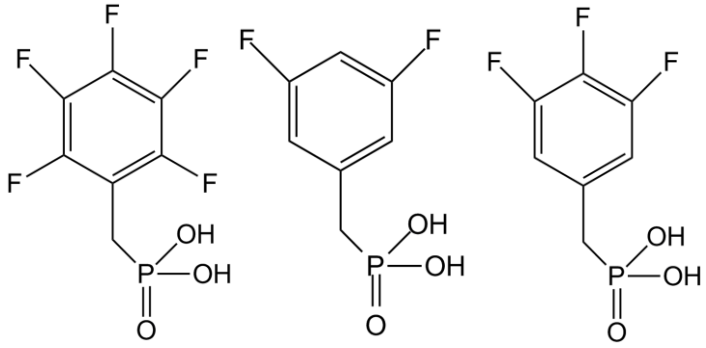

F_5BnPA mF_2BnPA (m,p)-F_3BnPA

Figure 1.3. Examples of PA SAM molecules.

Fine-tuning of the electrode work function is used to maximize built-in voltage and maximize the extraction of charge carriers. In the Schottky–Mott limit, the vacuum level of the active layer and electrode align, and the charge injection barrier is given by the difference between electrode work function and the orbital energy level of the appropriate charge carrier.[30, 31] In this limit, adjusting the work function of the contact yields an equal change in the built-in voltage of the device.[18, 30] A perfectly aligned, or ohmic, contact eliminates the injection barrier and maximizes charge extraction at the interface. Electroabsorption experiments on OLEDs revealed that the built-in voltage changed linearly with anode work-function as the ITO anode was modified with dipolar PA SAMs.[18] However, the change in built-in voltage was less than expected, indicating deviation from the Schottky-Mott limit. The most likely explanation is presence of an interfacial density of states, leading to a vacuum level offset as has been observed in other organic/metal interfaces.[30, 31] Nevertheless, tuning of the electrode work functions is known to improve charge injection into OLEDs[25, 32, 33] and impact charge extraction and built-in voltages in OSCs [2, 18, 23, 34]

ITO is ubiquitous in thin film electronics due to its excellent transparency and conductivity. However, the work function of ITO varies between 4.4-5.0 eV based on preparation[21, 25] and may not be ideally matched to the molecular orbitals of the HOMO of the donor (or LUMO of the acceptor in the case of inverted devices). Fluorinated SAMs are widely used as interface modifiers in organic electronic devices[2, 18, 32, 35, 36] as fluorination is a convenient means of altering both the and the surface energy of the SAM. Fluorinated PA SAMs on plasma-cleaned ITO (4.28 eV) can adjust the work function from 4.17 eV to 5.3 eV.[18, 37, 38] PA SAMs in particular have been used on transparent conductive oxides[21, 22, 39] they are stable and can be patterned using micro-contact printing.[32] Figure 1.3 shows some PA SAMs used in this research

which lead to a variety of work function modifications and surface energies. Surface energy modifications can lead to improved adhesion/wettability of the active layers[22] or induce changes in blend phase separation and morphology.[15, 16] Other modification techniques include thiol and carboxylic acid based SAMs,[23, 40, 41] and thin insulating polymer layers.[29]

$$\Delta\Phi_m = \frac{ne \cdot \mu_{mol} \cos(\alpha)}{\varepsilon_0 \cdot \varepsilon} \qquad [1.1]$$

The mechanism for work function modification by a PA SAM arises from a surface dipole leading to a vacuum level offset.[22, 42, 43] Figure 1.4 shows an energy level diagram depicting a metal-semiconductor interface with SAM modification. The contribution of SAM molecules with molecular dipole moment μ_{mol} to the total work-function change $\Delta\Phi_m$ is given by Equation 1.1: e denotes the fundamental charge; ε, the dielectric constant; ε_0, the vacuum permittivity; n, the coverage density; and α, the angle between the dipole moment and the surface normal. The bond dipole, BD, defined as the variation in electrostatic potential energy across the chemical bond between the oxide surface and the SAM adds to the work function shift, as does the effect of the chemical binding on the surface density of states.[44, 45] In order to predict the work function of the PA SAM modified oxide surface, one must examine molecular dipole, orientation, surface coverage and binding model.[46, 47]

The relative surface coverage of the different SAMs can be determined using x-ray photoelectron spectroscopy (XPS) and DFT calculations can be used to provide insight into molecular dipole moment and details of the binding geometry. My work is focused on determining the orientation of these monolayers using NEXAFS. Using the measured

orientations, along with DFT, XPS and other techniques, one can gain insight into the molecular details of the SAM and how best to design SAMs so as to achieve the desired surface modification.

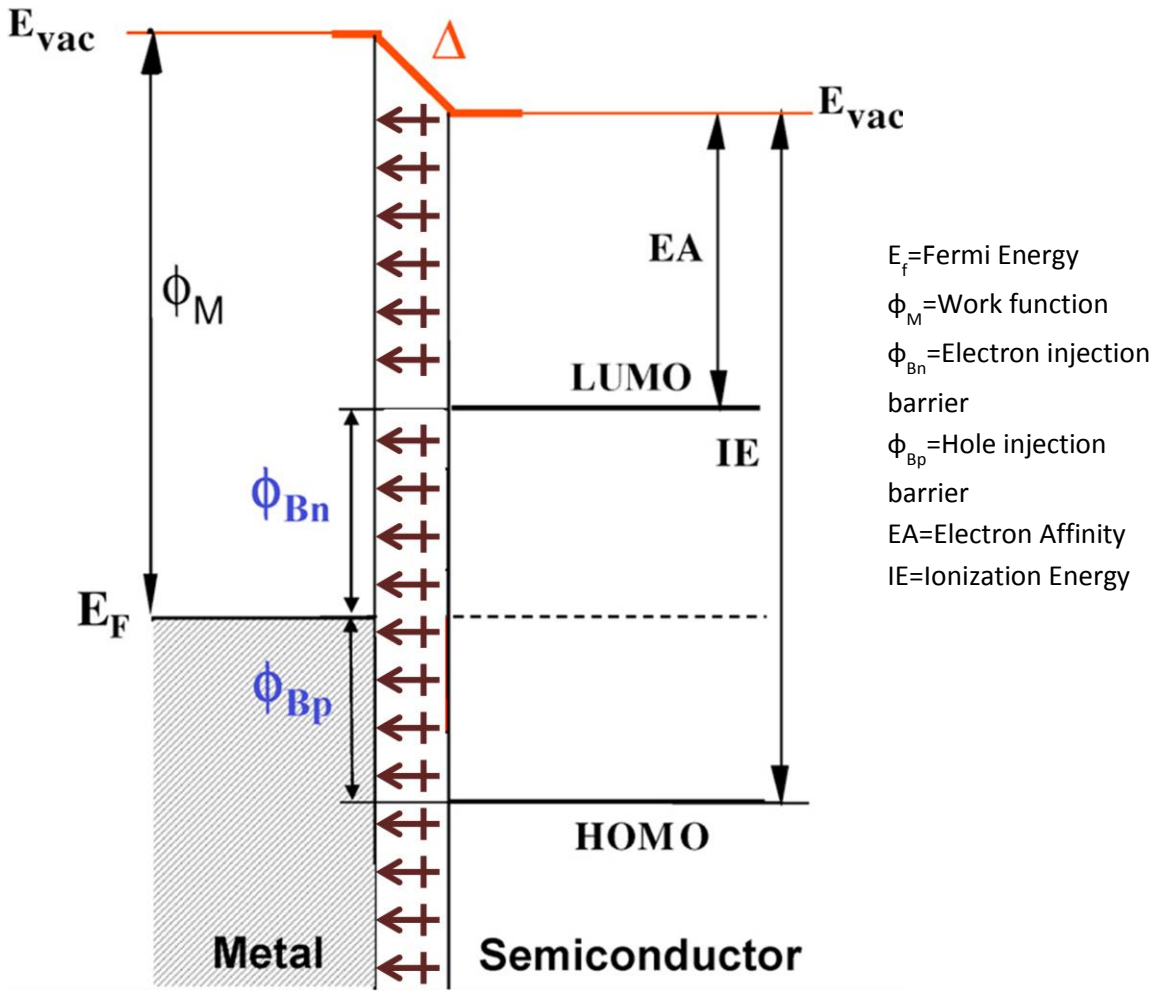

Figure 1.4. Depiction of a semiconductor-metal interface with a vacuum level shift due to a dipolar SAM. Adapted from Ref. 44.

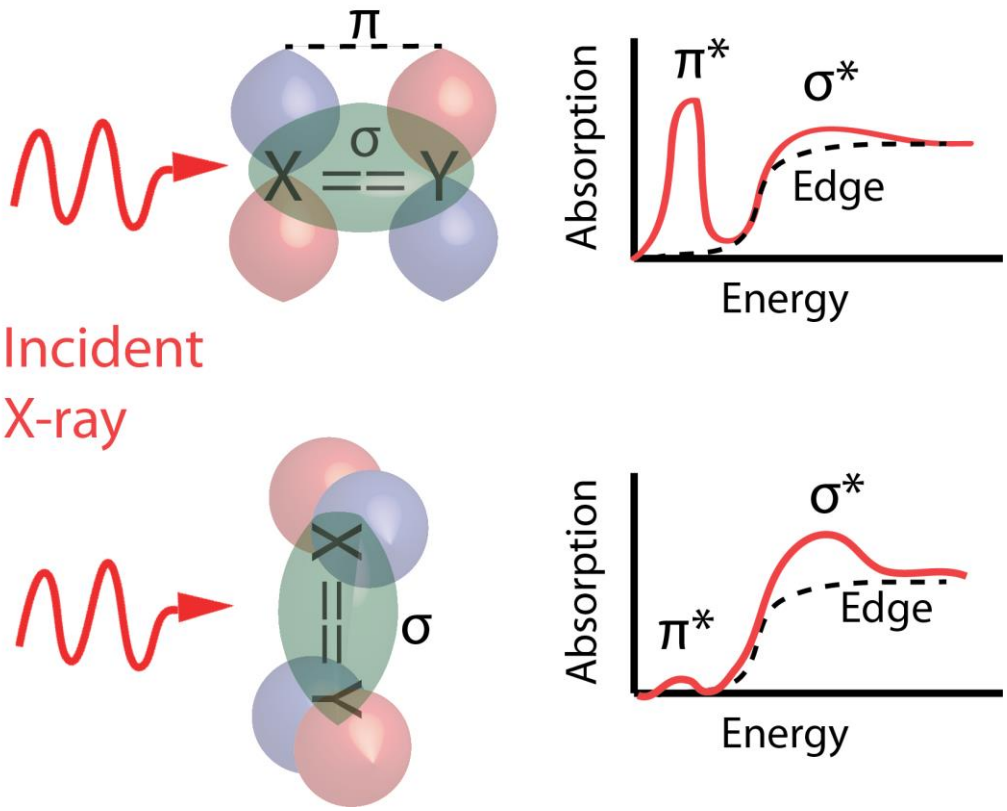

Figure 1.5. Example dependence of NEXAFS spectra on the relative orientation of polarization vector and transition dipole moments.

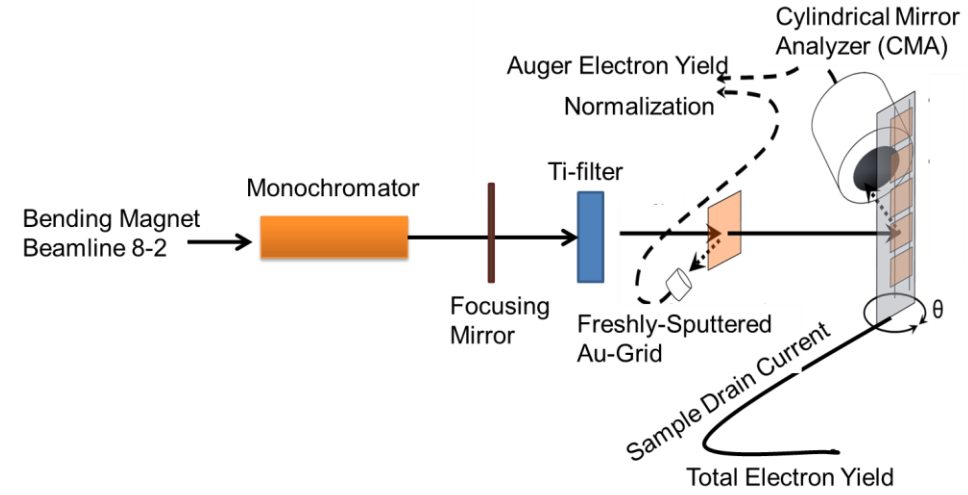

Figure 1.6 Depiction of our experimental setup on beamline 8-2 at SSRL.(top) Photograph of the end station of beamline 8-2.(Bottom)

1.4 NEXAFS

Near edge x-ray absorption fine structure (NEXAFS) is a form of x-ray spectroscopy which uses monochromatic x-rays from a synchrotron. The technique is used to examine fine-structure arising near atomic absorption edges, especially K-edges of low-Z atoms. Every feature in a single NEXAFS spectrum corresponds to an unoccupied molecular orbital involving the selected atomic species. NEXAFS has the ability to resolve changes in the chemical environment, and pick out specific bonds. As a result, NEXAFS makes an excellent fingerprinting technique for organic molecules.[48] In some cases, examining the spectra as a function of incident angle of the radiation, the orientation of specific bonds or even the entire molecule can be determined.[49-51] The features in the NEXAFS region occur at lower energies than the extended x-ray absorption fine structure (EXAFS) regime. The latter contains information on molecular bond lengths and ordering.

The fundamental process involved in NEXAFS is the absorption of an x-ray photon exciting a core electron to an unoccupied molecular orbital. Based the character of the final orbital, each such transition has a particular transition dipole moment. The strength of the absorption depends on the component of the polarization vector of the incoming x-rays parallel to the transition dipole moment. If the system probed is well-ordered, the NEXAFS spectra will exhibit a strong dependence on the incident angle of the x-rays. This angle dependence can, in principle, be observed for each peak in the NEXAFS spectrum. When a feature in the NEXAFS spectrum can be associated with an anti-bonding orbital of known character associated with a particular chemical bond, the orientation of this bond can be determined. This is shown in Figure 1.5 for a σ^* orbital (transition dipole moment along bond axis) and a π^* orbital (transition dipole moment

perpendicular to bond axis. In some cases, this provides enough information to determine the orientation of an entire molecule.[51] In chapters 2 and 3, I discuss how to apply these ideas to particular molecules.

Our NEXAFS data is collected on beamline 8-2 at Stanford Synchrotron Radiation Lightsource (SSRL).[52] Details on the experimental setup (Figure 1.6) are provided in the experimental section in chapter 2. Our data is collected in two primary modes: Auger electron yield (AEY) and total electron yield (TEY). Both methods count electrons that are liberated from the surface, rather than fluorescence. The absorption of an x-ray photon yields a core-hole which typically (in low-Z atoms) decays through an Auger process. The Auger process is a multi-electron non-radiative decay process, resulting in a filled core-hole and an emitted electron with a known kinetic energy. AEY data collection uses a cylindrical mirror analyzer (CMA) to pick out electrons of the appropriate kinetic energy. TEY data collection measures the current from the ground to the sample, thus counting the total number of electrons liberated from the surface. The depth sensitivity in AEY is limited by the electron mean free path, leading to a more surface sensitive collection mode as compared to TEY. For x-rays exciting near the C k-edge these sensitivities are about 1 nm and 10 nm respectively. In both data collection methods, a background arises from low-binding energy photoemission features. In the commonly studies systems, these contributions are typically from the substrate.[51] AEY data has a background made up of a convolution of the photoemission features with the monochromator energy as discussed in chapter 2. TEY, by contrast, has a smooth background as discussed in chapter 3. In both cases, we normalize the data by the intensity of the x-ray beam using the TEY signal from an Au-grid as discussed in chapter 2.

NEXAFS is commonly used to study organics, especially the orientation of molecules chemisorbed onto surfaces.[16, 48, 51, 53] One commonly studied system is the orientation of thiols and derivatives on noble metals.[54] Other than a study on the orientation of aliphatic PA SAMs as a function on chain length,[55] PA SAMs on transparent conductive oxides remained largely unexplored until this work.

1.5 Generation of free charge carriers in polymer films

Before charges can be extracted, some mechanism must exist to convert light to a free electron and hole. As discussed previously, the absorption of a photon leads to bound, neutral excitonic states rather than a free electron in the conduction band and a free hole in the valence band. Some losses occur due to recombination, reducing the photocurrent and operating efficiency. In order to produce efficient OSCs, exciton diffusion to the boundary between donor and acceptor materials must out-compete exciton decay processes. The electronic structure and exciton dynamics of the polymer are as relevant as the morphological issues discussed in section 1.2. Understanding the charge dynamics and nature of the excited state in the femtoseconds following charge absorption is critical to understanding why some polymers make more efficient solar cells than others.

The generation of photocurrent begins with absorption of a photon with energy near the band-gap. The absorption spectrum of the active layer is a critical component to design of OSC materials, as a spectrum similar to the solar spectrum will yield more power conversion efficiency. Incoming photons with energies below the band gap will not be absorbed while the absorption of a photon into a higher vibronic state potentially leads to a hot exciton that thermalizes and loses energy.[9, 56] Polymers usually have a strong vibronic coupling, so that the

absorption spectra can be expressed as a sum of peaks known as a Frank-Condon progression.[57] Each peak corresponds to a transition to a particular vibrational state, designated i-f where i is the initial vibrational state and f is the final vibrational state. 0 is the designation for the vibrational ground state. The ratio of the 0-0 peak to the 0-1 peak depends on the formation of J and H-aggregates in the polymer and contains structure and morphological information.[57, 58] J-aggregation and H-aggregation in polymers can lead to shifts in the absorption to longer and shorter wavelengths respectively.

The time between photon absorption and the extraction of free charges in P3HT/PCBM devices is about 100 ns-1 μs.[59] Time-resolved optical spectroscopy has been used to determine the timescales for numerous processes in P3HT/PCBM, which is considered the fruit fly of OSC research. The lifetime of the exciton is estimated at 300-500 ps.[60] The vibrational reorganization time, also known as the polaron formation time, is believed to be on the order of 10 ps.[60] However, none of these studies reached fast-enough time scales to probe exciton formation, which is now believed to occur within femtoseconds of photon absorption.

The femtosecond details of exciton formation and charge separation in OSCs are a subject of ongoing debate. Previous research on the exciton formation and charge separation processes in bulk-heterojunction OSCs include time resolved spectroscopies such as, photo-induced absorption[61], Raman pump-probe[12]and time-resolved terahertz spectroscopy[62]. Recent studies report that a photon absorbed in a P3HT/PCBM blend creates electrons and holes which are highly delocalized within the first 40 fs after absorption.[62] In this model, the electron and hole undergo dynamic localization within about 100 fs and undergo exciton formation in approximately 1 ps.[60, 62, 63] These processes may compete with dissociation of hot excitons on the sub 100fs time scale.[56] Other groups have reported charge transfer to a fullerene to occur on

timescales faster than 1 ps in P3HT/PCBM[61], to as fast as 45 fs in MDMO-PPV/PCBM,[12] but these charges may not necessarily be free.[62] Collini et al. found coherent charge migration along an MEH-PPV chain in solution to be ~20fs.[64] In PCPDTBT, mobile charge carriers are reportedly created within the first 200 fs, along with charge transfer states.[65]

The sub-50 fs dynamics of electrons in conjugated polymers are still poorly understood, but can be explored using resonant spectroscopies and the core-hole clock method. These techniques do not rely on pump-probe methods and can reveal details of processing at fs timescales.

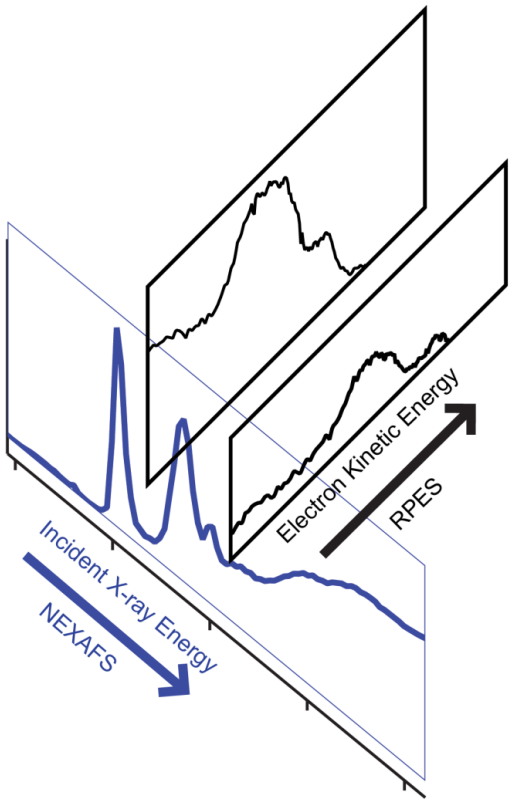

Figure 1.7. Depiction of the resonant electron spectroscopy data.

Besides the time scales involved in these processes, the delocalization of the excited state is of great importance. Resonant spectroscopies can also examine the electronic structure of the active layer and how these relate to the IQE of the device. If highly-delocalized carriers are formed within femtoseconds of photon absorption, then some free charges should escape the device before exciton formation, boosting the IQE and photocurrent. I use this idea to explore why PCDTBT, a state of the art polymer, is able to achieve nearly 100% IQE while a polymer with a similar bandgap, PCPDTBT, does not.[66]

1.6 Resonant spectroscopies

Resonant photoemission spectroscopy (RPES) and resonant Auger spectroscopy provide a synchrotron-based alternative to time-resolved optical spectroscopies in studying charge dynamics in the femtosecond and sub-femtosecond regimes. These techniques reveal details of the structure of occupied and excited state orbitals. In these resonant experiments, I record the photoemission spectra as we tune the incoming photon energy across an atomic absorption edge and the associated resonances (Figure 1.7). RPES and resonant Auger are an extension of NEXAFS and both possess chemical and site specificity.[51 67] When the photon energy is tuned to a resonant excitation, valence band photoemission as well as participator and spectator autoionization channels contribute to the spectrum of emitted electrons. Figure 1.8 demonstrates the available decay channels. RPES is typically the name given to the technique when the focus is on the photoemission and participator pathways. In the participator decay path, the photoexcited electron participates in a two-electron non-radiative auto-ionization process. The participator decay is energetically degenerate with photoemission features and has a Raman-like dispersion (constant binding energy).[68] The presence of the participator feature indicates spatial overlap between the wavefunctions of the excited state, the degenerate valence state and the core-hole. The branching ratio between photoemission and participator features can also be used in a variation of the core-hole clock method discussed later in order to examine femtosecond charge dynamics.

Resonant Auger spectroscopy is usually focused on the Auger and spectator pathways. In contrast to participator decay, spectator autoionization occurs with the photoexcited electron

remaining in the resonance. The resulting screening of the core hole results in a shift of the Auger emission features to a higher kinetic energy. In the absence of the Auger-resonant Raman effect, this spectator feature demonstrates a constant kinetic energy as the photon energy is tuned across a single resonance and exhibits a similar shape as the non-resonant Auger emission.[67] The Auger-resonant Raman effect is a photon-in, electron-out scattering process with no intermediate states. This effect is present when the bandwidth of the excitation is small compared to the width of the resonance and results in one-to-one changes to the kinetic energy of the spectator emission as the photon energy is detuned across a resonance.[67]

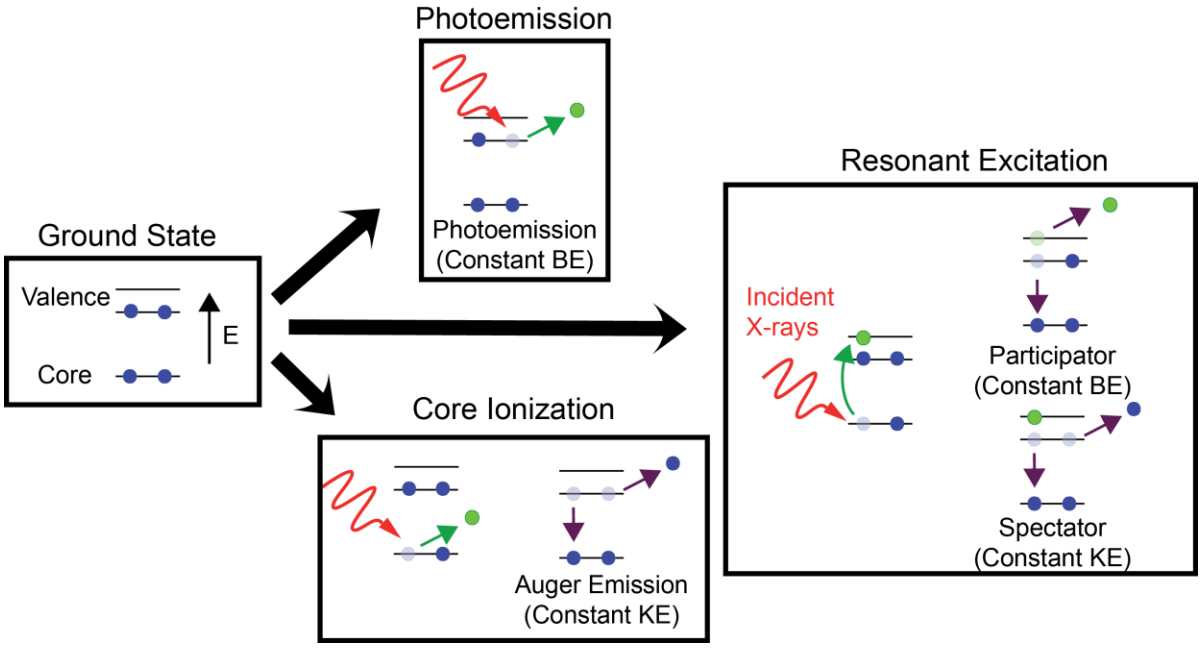

Figure 1.8. Decay pathways for different types of x-ray excitations. Some pathways emit electrons at constant kinetic energy (KE), while others have constant binding energy (BE). Green represents the photoexcited electron and purple arrows represent Auger processes.

If excited electrons can delocalize away from the core hole in times comparable to that of core-hole decay, then the resonant spectra will have a component identical to the non-resonant Auger emission which occurs for photon energies past the atomic absorption edge.[68] The branching ratio between these two paths can be used to measure the time scale of this delocalization process relative to the time scale of the core hole decay (5-6 fs). Using the core-hole clock method, I measure the time constant of the charge transfer, $\tau_{ct} = \tau_{ch} * (I_o/I_{ct})$. Here, τ_{ch} is the lifetime of the core hole and I_{ct}, and I_o are the intensities of Auger emissions that occur with or without charge transfer respectively.[69, 70, 71] The core-hole clock method provides for sub-femtosecond resolution of dynamics, provided the charge transfer occurs on a comparable time scale as the core hole decay. Typically, this technique can resolve dynamics on the ~1-100 fs timescales. A rigorous discussion of the technique can be found in the literature.[67, 68, 72]

Applications of the core-hole clock method to organic systems, especially in the areas of intramolecular charge transfer and organic-organic and organic-metal interfaces are present in the literature.[68, 72-77] Applications of this technique to thick (100nm) polymer films are less common.[78, 79] In P3HT and other polymer films, both the core-hole and the electronic states involved in Auger emission are strongly localized on a single monomer.[79, 80] One difficulty arises due to the presence of multiple charge transfer pathways, as shown in Figure 1.9. In polymer films, both through-space and through-bond charge transfer may be present. Through-bond mechanisms include delocalization of a charge carrier across a group of coupled monomers, referred to as a chromophore.[64] Through-space transport can occur as hopping from one chromophore to another either through a defect in the polymer backbone or across the pi-stacking distance. Some studies have shown tunneling across the pi-stacking distance between polymer chains to be the dominant charge transport process, but monomer-monomer charge

transport may be relevant given the highly local nature of the core hole and the states responsible for Auger emission.[44, 76, 79, 80] These charge transport processes may be dependent on the morphological properties of the film including pi-stacking distance and conjugation length. More troublingly for applications of the core-hole clock method to polymers is the assumption that charge transfer occurs to a final state which has little to no overlap with the initial state. In most core-hole clock experiments the use of a large metallic substrate satisfies this condition. In a polymer film, by contrast, the final state may not necessarily be free of overlap with the initial state, which may render the core-hole clock methodology inapplicable.

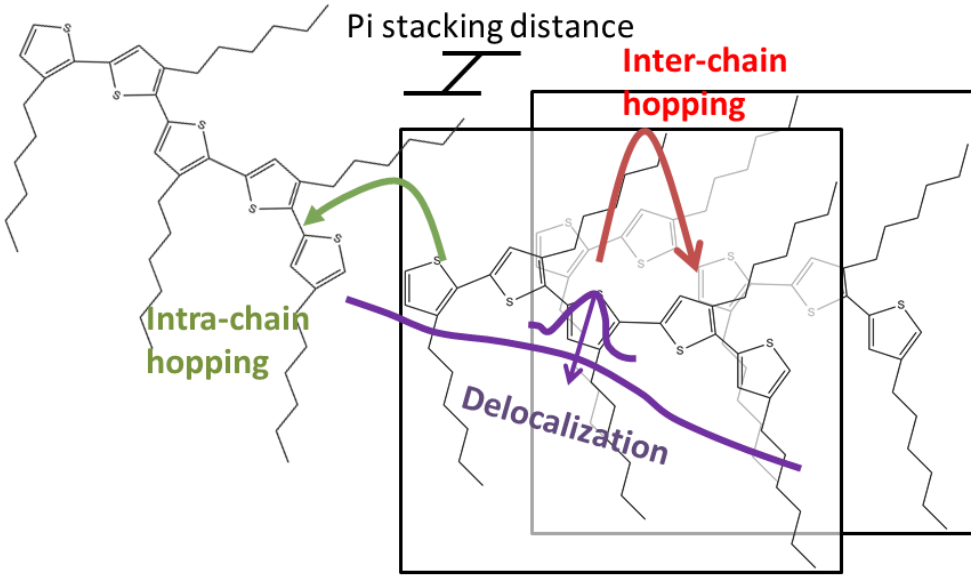

Figure 1.9. Possible charge transfer paths in a polymer film (P3HT).

When the core hole clock method is not applicable, one can still gain information from examining the spectator shift of the resonant Auger spectra. The spectator shift provides a qualitative measure of overlap between the core hole and the excited state orbital. By tuning our

x-ray energy to excite core electrons to the LUMO, I can probe the degree of localization of that LUMO orbital. Gallet et al. has previously performed resonant Auger spectroscopy of a polystyrene derivative and used the spectator shift to examine orbital delocalization and electronic structure.[79]

1.7 Structure of this dissertation

In chapter 2, I combine angle-dependent NEXAFS with polarization modulation infrared reflection absorption spectroscopy (PM-IRRAS) performed by my collaborators. I determine the molecular orientations of a model phenylphosphonic acid on indium zinc oxide, and correlate the resulting values with DFT calculations performed by my collaborators. I find phenylphosphonic acid to be well-oriented, with the phenyl ring adopting a tilt angle of 12-16° from the surface normal. Quantitative agreement between the two experimental techniques and single-molecule DFT calculations indicates that orientations are determined primarily by molecule-substrate interaction.

In chapter 3, I utilize angle-dependent NEXAFS to determine the molecular orientations of octylphosphonic acid, phenylphosphonic acid and fluorinated derivatives on ITO. I correlate the molecular orientations derived from these studies with predictions from DFT calculations performed by my collaborators. I examine quantitatively the effect of surface roughness on the measured orientations. I observe that fluorination of octylphosphonic acid SAMs results in more an upright orientation, possibly due to intermolecular forces and increased steric bulk. In contrast, fluorination of phenylphosphonic acid SAMs leads to a less upright orientation which to changes in binding mode. I further compare PA SAMS deposited on both ITO and indium zinc oxide (IZO) using various commonly used techniques including hot and room temperature

soaking and micro-contact printing. I find no significant difference between the deposition methods for orientation, and attribute substrate differences to surface roughness. Lastly, I present a survey of the orientations of 12 benzylphosphonic acid (BnPA) derivatives which provide a wide range of work-function modification. Most of the BnPA molecules exhibit a large degree of disorder.

In chapter 4, I examine two polymers: PCDTBT and PCPDTBT using resonant Auger spectroscopy. OSCs made using PCDTBT demonstrate an IQE of nearly 100%[66] while devices made with PCPDTBT are about 30 percentage points less efficient.[81] I use DFT and resonant Auger spectroscopy to measure the overlap of the excited state orbitals with the nitrogen atoms on the benzothiadiazole unit. I observe good agreement between DFT calculations and the spectator shifts measured with resonant Auger spectroscopy, but reveal no significant differences between the two polymers.

1.8 References

1. Guenes, S.; Neugebauer, H.; Sariciftci, N. S., Conjugated polymer-based organic solar cells. *Chem. Rev.* **2007,** *107*, 1324-1338.

2. Ma, H.; Yip, H.-L.; Huang, F.; Jen, A. K. Y., Interface Engineering for Organic Electronics. *Adv. Funct. Mater.* **2010,** *20*, 1371-1388.

3. Dimitrakopoulos, C. D.; Malenfant, P. R. L., Organic Thin Film Transistors for Large Area Electronics. *Adv. Mater.* **2002,** *14*, 99-117.

4. Cantatore, E.; Geuns, T. C. T.; Gelinck, G. H.; van Veenendaal, E.; Gruijthuijsen, A. F. A.; Schrijnemakers, L.; Drews, S.; de Leeuw, D. M., A 13.56-MHz RFID System Based on Organic Transponders. *IEEE J. Solid State Circuits* **2007,** *42*, 84-92.

5. Ryu, G. S.; Kim, J. S.; Jeong, S. H.; Song, C. K., A printed OTFT-backplane for AMOLED Display. *Org. Electron.* **2013,** *14*, 1218-1224.

6. Kwon, J. Y.; Son, K. S.; Jung, J. S.; Kim, T. S.; Ryu, M. K.; Park, K. B.; Yoo, B. W.; Kim, J. W.; Lee, Y. G.; Park, K. C.; Lee, S. Y.; Kim, J. M., Bottom-Gate Gallium Indium Zinc

Oxide Thin-Film Transistor Array for High-Resolution AMOLED Display. *IEEE Electron Device Lett.* **2008,** *29*, 1309-1311.

7. Yagi, I.; Hirai, N.; Miyamoto, Y.; Noda, M.; Imaoka, A.; Yoneya, N.; Nomoto, K.; Kasahara, J.; Yumoto, A.; Urabe, T., A Flexible Full-Color AMOLED Display Driven by OTFTs. *Inform. Display J. Soc. I.* **2008,** *16*, 15-20.

8. Reese, M. O.; Gevorgyan, S. A.; Jorgensen, M.; Bundgaard, E.; Kurtz, S. R.; Ginley, D. S.; Olson, D. C.; Lloyd, M. T.; Moryillo, P.; Katz, E. A.; et al. Consensus Stability Testing Protocols for Organic Photovoltaic Materials and Devices. *Sol. Energ. Mat. Sol. Cells* **2011,** *95*, 1253-1267.

9. Brabec, C. J.; Gowrisanker, S.; Halls, J. J. M.; Laird, D.; Jia, S.; Williams, S. P., Polymer-Fullerene Bulk-Heterojunction Solar Cells. *Adv. Mater.* **2010,** *22*, 3839-3856.

10. Small, C. E.; Chen, S.; Subbiah, J.; Amb, C. M.; Tsang, S. W.; Lai, T. H.; Reynolds, J. R.; So, F., High-Efficiency Inverted Dithienogermole-Thienopyrrolodione-Based Polymer Solar Cells. *Nature Photon.* **2012,** *6*, 115-120.

11. He, Z. C.; Zhong, C. M.; Su, S. J.; Xu, M.; Wu, H. B.; Cao, Y., Enhanced Power-Conversion Efficiency in Polymer Solar Cells Using an Inverted Device Structure. *Nature Photon.* **2012,** *6*, 591-595.

12. Brabec, C. J.; Zerza, G.; Cerullo, G.; De Silvestri, S.; Luzzati, S.; Hummelen, J. C.; Sariciftci, S., Tracing Photoinduced Electron Transfer Process in Conjugated Polymer/Fullerene Bulk Heterojunctions in Real Time. *Chem. Phys. Lett.* **2001,** *340*, 232-236.

13. Ren, G. Q.; Schlenker, C. W.; Ahmed, E.; Subramaniyan, S.; Olthof, S.; Kahn, A.; Ginger, D. S.; Jenekhe, S. A., Photoinduced Hole Transfer Becomes Suppressed with Diminished Driving Force in Polymer-Fullerene Solar Cells While Electron Transfer Remains Active. *Adv. Funct. Mater.* **2013,** *23*, 1238-1249.

14. Giridharagopal, R.; Ginger, D. S., Characterizing Morphology in Bulk Heterojunction Organic Photovoltaic Systems. *J. of Phys. Chem. Lett.* **2010,** *1*, 1160-1169.

15. Park, L. Y.; Munro, A. M.; Ginger, D. S., Controlling Film Morphology in Conjugated Polymer: Fullerene Blends with Surface Patterning. *J. Amer. Chem. Soc.* **2008,** *130*, 15916-15926.

16. DeLongchamp, D. M.; Kline, R. J.; Fischer, D. A.; Richter, L. J.; Toney, M. F., Molecular Characterization of Organic Electronic Films. *Adv. Mater.* **2011,** *23*, 319-337.

17. Bredas, J. L.; Norton, J. E.; Cornil, J.; Coropceanu, V., Molecular Understanding of Organic Solar Cells: The Challenges. *Accounts Chem. Res.* **2009,** *42*, 1691-1699.

18. MacLeod, B. A.; Horwitz, N. E.; Ratcliff, E. L.; Jenkins, J. L.; Neal R. Armstrong, N. R.; Giordano, A. J.; Hotchkiss, P. J.; Marder, S. R.; Campbell, C. T.; Ginger, D. S., Built-In

Potential in Conjugated Polymer Diodes with Changing Anode Work Function: Interfacial States and Deviation from the Schottky–Mott Limit. *J. Phys. Chem. Lett.* **2012,** *3*, 1202-1207.

19. Besbes, S.; Ltaief, A.; Reybier, K.; Ponsonnet, L.; Jaffrezic, N.; Davenas, J.; Ben Ouada, H., Injection Modifications by ITO Functionalization with a Self-Assembled Monolayer in OLEDs. *Synthetic Met.* **2003,** *138*, 197-200.

20. Hanson, E. L.; Guo, J.; Koch, N.; Schwartz, J.; Bernasek, S. L., Advanced Surface Modification of Indium Tin Oxide for Improved Charge Injection in Organic Devices. *J. Amer. Chem. Soc.* **2005,** *127*, 10058-10062.

21. Hotchkiss, P. J.; Jones, S. C.; Paniagua, S. A.; Sharma, A.; Kippelen, B.; Armstrong, N. R.; Marder, S. R., The Modification of Indium Tin Oxide with Phosphonic Acids: Mechanism of Binding, Tuning of Surface Properties, and Potential for Use in Organic Electronic Applications. *Accounts Chem. Res.* **2012,** *45*, 337-346.

22. Paniagua, S. A.; Hotchkiss, P. J.; Jones, S. C.; Marder, S. R.; Mudalige, A.; Marrikar, F. S.; Pemberton, J. E.; Armstrong, N. R., Phosphonic Acid Modification of Indium-Tin Oxide Electrodes: Combined XPS/UPS/Contact Angle Studies. *J. Phys. Chem. C* **2008,** *112*, 7809-7817.

23. Beaumont, N.; Hancox, I.; Sullivan, P.; Hatton, R. A.; Jones, T. S., Increased Efficiency in Small Molecule Organic Photovoltaic Cells through Electrode Modification with Self-Assembled Monolayers. *Energy Environ. Sci.* **2011,** *4*, 1708-1711.

24. Pingree, L. S. C.; MacLeod, B. A.; Ginger, D. S., The Changing Face of PEDOT : PSS Films: Substrate, Bias, and Processing Effects on Vertical Charge Transport. *J. Phys. Chem. C* **2008,** *112*, 7922-7927.

25. Wang, M.; Hill, I. G., Fluorinated Alkyl Phosphonic Acid SAMs Replace PEDOT:PSS in Polymer Semiconductor Devices. *Org. Electron.* **2012,** *13*, 498-505.

26. Morana, M.; Wegscheider, M.; Bonanni, A.; Kopidakis, N.; Shaheen, S.; Scharber, M.; Zhu, Z.; Waller, D.; Gaudiana, R.; Brabec, C., Bipolar Charge Transport in PCPDTBT-PCBM Bulk-Heterojunctions for Photovoltaic Applications. *Adv. Funct. Mater.* **2008,** *18*, 1757-1766.

27. White, M. S.; Olson, D. C.; Shaheen, S. E.; Kopidakis, N.; Ginley, D. S., Inverted Bulk-Heterojunction Organic Photovoltaic Device Using a Solution-Derived ZnO Underlayer. *Appl. Phys. Lett.* **2006,** *89*, 143517.

28. Chen, J.; Ruther, R. E.; Tan, Y.; Bishop, L. M.; Hamers, R. J., Molecular Adsorption on ZnO(10(1)over-bar0) Single-Crystal Surfaces: Morphology and Charge Transfer. *Langmuir* **2012,** *28*, 10437−10445.

29. Zhou, Y.; Fuentes-Hernandez, C.; Shim, J.; Meyer, J.; Giordano, A. J.; Li, H.; Winget, P.; Papadopoulos, T.; Cheun, H.; Kim, J.; et al., A Universal Method to Produce Low-Work Function Electrodes for Organic Electronics. *Science* **2012,** *336*, 327-332.

30. Blakesley, J. C.; Greenham, N. C., Charge Transfer at Polymer-Electrode Interfaces: The Effect of Energetic Disorder and Thermal Injection on Band Bending and Open-Circuit Voltage. *J. Appl. Phys.* **2009,** *106,* 03450-034513.

31. Kemerink, M.; Kramer, J. M.; Gommans, H. H. P.; Janssen, R. A. J., Temperature-Dependent Built-in Potential in Organic Semiconductor Devices. *Appl. Phys. Lett.* **2006,** *88,* 192108-192110.

32. Knesting, K. M.; Hotchkiss, P. J.; MacLeod, B. A.; Marder, S. R.; Ginger, D. S., Spatially Modulating Interfacial Properties of Transparent Conductive Oxides: Patterning Work Function with Phosphonic Acid Self-Assembled Monolayers. *Adv. Mater.* **2012,** *24*, 642-646.

33. Sharma, A.; Haldi, A.; Hotchkiss, P. J.; Marder, S. R.; Kippelen, B., Effect of Phosphonic Acid Surface Modifiers on the Work Function of Indium Tin Oxide and on the Charge Injection Barrier into Organic Single-Layer Diodes. *J. Appl. Phys.* **2009,** *105*, 074511-074516.

34. Kouki, F.; Karsi, N.; Lang, P.; Horowitz, G.; Bouchriha, H., Effect of Self Assembled Monolayers on Charge Carrier Photogeneration in Sexithiophene Based Diodes. *Synthetic Met.* **2012,** *162*, 1741-1745.

35. Wu, K.-Y.; Yu, S.-Y.; Tao, Y.-T., Continuous Modulation of Electrode Work Function with Mixed Self-Assembled Monolayers and Its Effect in Charge Injection. *Langmuir* **2009,** *25*, 6232-6238.

36. Marmont, P.; Battaglini, N.; Lang, P.; Horowitz, G.; Hwang, J.; Kahn, A.; Amato, C.; Calas, P., Improving Charge Injection in Organic Thin-Film Transistors with Thiol-Based Self-Assembled Monolayers. *Org. Electron.* **2008,** *9*, 419-424.

37. Hotchkiss, P. J.; Li, H.; Paramonov, P. B.; Paniagua, S. A.; Jones, S. C.; Armstrong, N. R.; Bredas, J. L.; Marder, S. R., Modification of the Surface Properties of Indium Tin Oxide with Benzylphosphonic Acids: A Joint Experimental and Theoretical Study. *Adv.Mater.* **2009,** *21*, 4496-4501.

38. Sharma, A.; Hotchkiss, P. J.; Marder, S. R.; Kippelen, B., Tailoring the Work Function of Indium Tin Oxide Electrodes in Electrophosphorescent Organic Light-Emitting Diodes. *J. Appl. Phys.* **2009,** *105,* 084507-084502.

39. Cecchet, F.; Lis, D.; Guthmuller, J.; Champagne, B.; Fonder, G.; Mekhalif, Z.; Caudano, Y.; Mani, A. A.; Thiry, P. A.; Peremans, A., Theoretical Calculations and Experimental Measurements of the Vibrational Response of p-NTP SAMs: An Orientational Analysis. *J. Phys. Chem. C.* **2010,** *114*, 4106-4113.

40. Cerruti, M.; Rhodes, C.; Losego, M.; Efremenko, A.; Maria, J. P.; Fischer, D.; Franzen, S.; Genzer, J., Influence of Indium-Tin Oxide Surface Structure on the Ordering and Coverage of Carboxylic Acid and Thiol Monolayers. *J. Phys. D.* **2007,** *40,* 4212-4221.

41. Yan, C.; Zharnikov, M.; Golzhauser, A.; Grunze, M., Preparation and Characterization of Self-Assembled Monolayers on Indium Tin Oxide. *Langmuir* **2000,** *16,* 6208-6215.

42. Heimel, G.; Romaner, L.; Zojer, E.; Bredas, J.-L., The Interface Energetics of Self-Assembled Monolayers on Metals. *Accounts Chem. Res.* **2008,** *41*, 721-729.

43. Kronik, L.; Shapira, Y., Surface Photovoltage Phenomena: Theory, Experiment, and Applications. *Surface Science Reports* **1999,** *37*, 1-206.

44. Friedlein, R.; Sorensen, S. L.; Osikowicz, W.; Rosenqvist, L.; Crispin, A.; Crispin, X.; de Jong, M.; Murphy, C.; Fahlman, M.; Salaneck, W. R., Electronic Structure of Conjugated Polymers and Interfaces in Polymer-Based Electronics. *Synthetic Met.* **2003,** *135*, 275-277.

45. Li, H.; Paramonov, P.; Bredas, J. L., Theoretical Study of the Surface Modification of Indium Tin Oxide with Trifluorophenyl Phosphonic Acid Molecules: Impact of Coverage Density and Binding Geometry. *J. Mater. Chem.* **2010,** *20*, 2630-2637.

46. Romaner, L.; Heimel, G.; Zojer, E., Electronic Structure of Thiol-Bonded Self-Assembled Monolayers: Impact of Coverage. *Phys. Rev. B.* **2008,** *77-85*.

47. Alloway, D. M.; Hofmann, M.; Smith, D. L.; Gruhn, N. E.; Graham, A. L.; Colorado, R.; Wysocki, V. H.; Lee, T. R.; Lee, P. A.; Armstrong, N. R., Interface Dipoles Arising from Self-Assembled Monolayers on Gold: UV-Photoemission Studies of Slkanethiols and Partially Fluorinated Alkanethiols. *J. Phys. Chem. B.* **2003,** *107*, 11690-11699.

48. Watts, B.; Swaraj, S.; Nordlund, D.; Luening, J.; Ade, H., Calibrated NEXAFS spectra of common conjugated polymers. *J. Chem. Phys.* **2011,** *134*, 024702-024716.

49. Stohr, J.; Gland, J. L.; Eberhardt, W.; Outka, D.; Madix, R. J.; Sette, F.; Koestner, R. J.; Doebler, U., Bonding and Bond Lengths of Chemisorbed Molecules from near-Edge X-Ray-Absorption Fine-Structure Studies. *Phys. Rev. Lett.* **1983,** *51*, 2414-2417.

50. Stöhr, J.; Outka, D. A., Determination of Molecular Orientations on Surfaces from the Angular-Dependence of Near-Edge X-Ray-Absorption Fine-Structure Spectra. *Phys. Rev. B* **1987,** *36*, 7891-7905.

51. Stöhr, J., *NEXAFS spectroscopy*. Springer-Verlag: Berlin, 1992; p xv, 403 p.

52. Tirsell, K. G.; Karpenko, V. P., A General-Purpose Sub-Kev X-Ray Facility at the Stanford-Synchrotron-Radiation-Laboratory. *Nucl. Instrum. Meth. A* **1990,** *291*, 511-517.

53. Yang, M. X.; Xi, M.; Yuan, H. J.; Bent, B. E.; Stevens, P.; White, J. M., Nexafs Studies of Halobenzenes and Phenyl Groups on Cu(111). *Surf. Sci.* **1995,** *341*, 9-18.

54. Vericat, C.; Vela, M. E.; Benitez, G.; Carro, P.; Salvarezza, R. C., Self-Assembled Monolayers of Thiols and Dithiols on Gold: New Challenges for a Well-Known System. *Chem. Soc. Rev.* **2010,** *39*, 1805-1834.

55. Losego, M. D.; Guske, J. T.; Efremenko, A.; Maria, J.-P.; Franzen, S., Characterizing the Molecular Order of Phosphonic Acid Self-Assembled Monolayers on Indium Tin Oxide Surfaces. *Langmuir* **2011,** *27*, 11883-11888.

56. Guo, J.; Ohkita, H.; Benten, H.; Ito, S., Charge Generation and Recombination Dynamics in Poly(3-hexylthiophene)/Fullerene Blend Films with Different Regioregularities and Morphologies. *J. Amer. Chem. Soc.* **2010,** *132*, 6154–6164.

57. Clark, J.; Silva, C.; Friend, R. H.; Spano, F. C., Role of Intermolecular Coupling in the Photophysics of Disordered Organic Semiconductors: Aggregate Emission in Regioregular Polythiophene. *Phys. Rev. Lett.* **2007,** *98*, 206406-206409.

58. Clark, J.; Chang, J. F.; Spano, F. C.; Friend, R. H.; Silva, C., Determining Exciton Bandwidth and Film Microstructure in Polythiophene Films using Linear Absorption Spectroscopy. *Appl. Phys. Lett.* **2009,** *94*, 163306-163308.

59. Marsh, R. A.; McNeill, C. R.; Abrusci, A.; Campbell, A. R.; Friend, R. H., A Unified Description of Current-Voltage Characteristics in Organic and Hybrid Photovoltaics under Low Light Intensity. *Nano Lett.* **2008,** *8*, 1393-1398.

60. Banerji, N.; Cowan, S.; Vauthey, E.; Heeger, A. J., Ultrafast Relaxation of the Poly(3-hexylthiophene) Emission Spectrum. *J. Phys. Chem. C.* **2011,** *115*,9726–9739.

61. Hwang, I.-W.; Moses, D.; Heeger, A. J., Photoinduced Carrier Generation in P3HT/PCBM Bulk Heterojunction Materials. *J. Phys. Chem. C.* **2008,** *112*, 4350–4354.

62. Cooke, D. G.; Krebs, F. C.; Jepsen, P. U., Direct Observation of Sub-100 fs Mobile Charge Generation in a Polymer-Fullerene Film. *Phys. Rev. Lett.* **2012,** *108*, 056603-056607.

63. Xie, Y.; Li, Y.; Xiao, L.; Qiao, Q.; Dhakal, R.; Zhang, Z.; Gong, Q.; Galipeau, D.; Yan, X., Femtosecond Time-Resolved Fluorescence Study of P3HT/PCBM Blend Films. *J. Phys. Chem. C* **2010,** *114*, 14590–14600.

64. Collini, E.; Scholes, G. D., Coherent Intrachain Energy Migration in a Conjugated Polymer at Room Temperature. *Science* **2009,** 323, 369-373.

65. Hwang, I.-W.; Soci, C.; Moses, D.; Zhu, Z.; Waller, D.; Gaudiana, R.; Brabec, C. J.; Heeger, A. J., Ultrafast Electron Transfer and Decay Dynamics in a Small Band Gap Bulk Heterojunction Material. *Adv. Mater.* **2007,** *19*, 2307-2312.

66. Park, S. H.; Roy, A.; Beaupre, S.; Cho, S.; Coates, N.; Moon, J. S.; Moses, D.; Leclerc, M.; Lee, K.; Heeger, A. J., Bulk Heterojunction Solar Cells with Internal Quantum Efficiency Approaching 100%. *Nature Photon.* **2009,** *3*, 297-302.

67. Bruhwiler, P. A.; Karis, O.; Martensson, N., Charge-Transfer Dynamics Studied using Resonant Core Spectroscopies. *Rev. Mod. Phys.* **2002,** *74*, 703–740.

68. Vilmercati, P.; Cvetko, D.; Cossaro, A.; Morgante, A., Heterostructured Organic Interfaces Probed by Resonant Photoemission. *Surf. Sci.* **2009,** *603*, 1542-1556.

69. Nordlund, D.; Ogasawara, H.; Bluhm, H.; Takahashi, O.; Odelius, M.; Nagasono, M.; Pettersson, L. G. M.; Nilsson, A., Probing the Electron Delocalization in Liquid Water and Ice at Attosecond Time Scales. *Phys. Rev. Lett.* **2007,** *99*, 217406-217409.

70. Foehlisch, A.; Vijayalakshmi, S.; Pietzsch, A.; Nagasono, M.; Wurth, W.; Kirchmann, P. S.; Loukakos, P. A.; Bovensiepen, U.; Wolf, M.; Tchaplyguine, M.; et al. Charge Transfer Dynamics in Molecular Solids and Adsorbates Driven by Local and Non-Local Excitations. *Surf. Sci.* **2012,** *606*, 881-885.

71. Wurth, W.; Menzel, D., Ultrafast Electron Dynamics at Surfaces Probed by Resonant Auger Spectroscopy. *Chem. Phys.* **2000,** *251*, 141-149.

72. Schnadt, J.; Bruhwiler, P. A.; Patthey, L.; O'Shea, J. N.; Sodergren, S.; Odelius, M.; Ahuja, R.; Karis, O.; Bassler, M.; Persson, P.; Siegbahn, H.; Lunell, S.; Martensson, N., Experimental Evidence for Sub-3-fs Charge Transfer from an Aromatic Adsorbate to a Semiconductor. *Nature* **2002,** *418*, 620-623.

73. Ben Taylor, J.; Mayor, L. C.; Swarbrick, J. C.; O'Shea, J. N.; Schnadt, J., Charge-Transfer Dynamics at Model Metal-Organic Solar Cell Surfaces. *J. Phys.Chem. C* **2007,** *111*, 16646-16655.

74. Petraki, F.; Peisert, H.; Biswas, I.; Aygul, U.; Latteyer, F.; Vollmer, A.; Chasse, T., Interaction between Cobalt Phthalocyanine and Gold Studied by X-ray Absorption and Resonant Photoemission Spectroscopy. *J. Phys. Chem. Lett.* **2010,** *1*, 3380-3384.

75. Peisert, H.; Biswas, I.; Zhang, L.; Schuster, B. E.; Casu, M. B.; Haug, A.; Batchelor, D.; Knupfer, M.; Chasse, T., Unusual Energy Shifts in Resonant Photoemission Spectra of Organic Model Molecules. *J. Chem.Phys.* **2009,** *130*, 194705-194711.

76. Friedlein, R.; Braun, S.; de Jong, M. P.; Osikowicz, W.; Fahlman, M.; Salaneck, W. R., Ultra-fast Charge Transfer in Organic Electronic Materials and at Hybrid Interfaces Studied using the Core-Hole Clock Technique. *J. Electron. Spectrosc.* **2011,** *183*, 101-106.

77. Hamoudi, H.; Neppl, S.; Kao, P.; Schupbach, B.; Feulner, P.; Terfort, A.; Allara, D.; Zharnikov, M., Orbital-Dependent Charge Transfer Dynamics in Conjugated Self-Assembled Monolayers. *Phys. Rev. Lett.* **2011,** *107*, 027801-027805.

78. Hintz, H.; Peisert, H.; Aygul, U.; Latteyer, F.; Biswas, I.; Nagel, P.; Merz, M.; Schuppler, S.; Breusov, D.; Allard, S.; Scherf, U.; Chasse, T., Electronic Structure and Interface Properties of a Model Molecule for Organic Solar Cells. *ChemPhysChem.* **2010,** *11*, 269-275.

79. Gallet, J. J.; Jolly, F.; Rochet, F.; Bournel, F.; Dufour, G.; Avila, P. A.; Sirotti, F.; Torelli, P., Resonant Auger Spectroscopy of Poly(4-hydroxystyrene). *J. Electronj Spectrosc.* **2002,** *122*, 11-25.

80. Schmeisser, D., Valence States of Poly(3-hexyl-thiophene) as Probed by Photoelectron Spectra at Resonant Excitation. *Synthetic Met.* **2003,** *138*, 135-140.

81. Clarke, T.; Ballantyne, A.; Jamieson, F.; Brabec, C.; Nelson, J.; Durrant, J., Transient Absorption Spectroscopy of Charge Photogeneration Yields and Lifetimes in a Low Bandgap Polymer/Fullerene Film. *Chem. Commun.* **2009**, 89-91.

Chapter 2: Orientation of Phenylphosphonic Acid Self-Assembled Monolayers on a Transparent Conductive Oxide: A Combined NEXAFS, PM-IRRAS and DFT Study

Adapted from: Gliboff, M.; Sang, L.; Knesting, K. M.; Schalnat, M. C.; Mudalige, A.; Ratcliff, E. L.; Li, H.; Sigdel, A. K.; Giordano, A. J.; Berry, J. J.; Nordlund, D.; Seidler, G. T.; Brédas, J.-L.; Marder, S. R.; Pemberton, J. E.; Ginger, D. S. *Langmuir* **2013,** *29*, 2166-2174.

I am responsible for all NEXAFS data, analysis and comparison with other techniques and the writing of this manuscript.

2.1 Introduction

Self-assembled monolayers (SAMs) have been used to improve the performance of electronic devices including organic light-emitting diodes (OLEDs),[1-3] organic field-effect transistors (OFETs)[4] and organic photovoltaics (OPVs).[5,6] SAMs can improve adhesion/wettability of the active layers,[7] control blend phase separation and morphology[8,9,10] and are useful for tuning work functions and interfacial barrier heights.[1,2,3,11,12] Phosphonic acids in particular are known to form robust monolayers that increase interfacial compatibility between a transparent conductive oxide and the organic device layer in optoelectronic devices.[7,13,14] While the properties of SAMs such as thiols on coinage metals[14] are well-studied, the molecular level details of technologically relevant SAMs such as aromatic phosphonic acids on transparent conductive oxides are comparatively poorly understood. Data such as the molecular tilt of an aromatic phosphonic acid with respect to the surface are virtually unknown.

Nevertheless, these details are critical to the design and performance of SAM-modified interfaces in thin film electronics. Phosphonic acid binding mode, orientation, and surface coverage can affect the contact angle and work function of modified oxide surfaces.[11,16] The

work-function modification can be described as the combination of three effects:[17] (i) the electrostatic potential step (bond dipole) created at the very interface between the oxide surface and the SAM because of the chemical binding; (ii) the possible relaxation of the surface geometry upon binding; and (iii) the electrostatic potential step across the molecular SAM. At the most basic level,[1,10,12,18,19] the magnitude of the latter term, $\Delta\Phi$, is given by:

$$\Delta\Phi = \frac{ne \cdot \mu_{mol} \cos(\theta)}{\varepsilon_0 \cdot \varepsilon} \qquad [2.1]$$

Here, μ_{mol} is the molecular dipole moment, θ is the angle the dipole moment makes with the surface normal, ε is the dielectric constant, n is coverage density, *e* is the charge of an electron and ε_0 is the vacuum permittivity.[20] However, while quantum-chemical calculations can provide the first two terms as well as μ_{mol}, the other parameters needed to calculate $\Delta\Phi$, notably n and θ, are best determined experimentally. Even so, with one exception of an insulating alkane phosphonic acid,[21] the tilt angles of most phosphonic acid SAMs have not, to our knowledge, been measured directly.

In this paper, we present a unique and systematic study of the molecular tilt angle of a model phosphonic acid on a transparent conductive oxide that combines both near edge x-ray absorption fine structure (NEXAFS) spectroscopy and polarization modulation infrared reflection absorption spectroscopy (PM-IRRAS). Cross-correlation of NEXAFS and PM-IRRAS measurements is important for several reasons. Notably, we can both validate the procedures for angle-dependent background subtraction in the NEXAFS data for this class of materials, and we

can confirm the IR vibrational mode assignments of the PM-IRRAS data. Comparison to density functional theory (DFT) calculations further strengthens our results.

We chose phenylphosphonic acid (PPA) as our model SAM because it is the simplest representative of a class of SAMs that are known to improve optoelectronic device performance. We selected indium zinc oxide (IZO) for its optical transparency in the infrared region, its ability to form conformal films on a reflective Au substrate (as described below, both attributes are requirements for PM-IRRAS experiments), and its recent utilization in optoelectronic devices.[22,23] We determine the orientation of the phenyl ring using both NEXAFS and PM-IRRAS, and correlate the resulting values with DFT. After correctly assigning the IR vibrational modes observed in PM-IRRAS, we achieve quantitative agreement in the molecular orientation between the two experimental methods, as well as remarkably good agreement with the theoretical predictions.

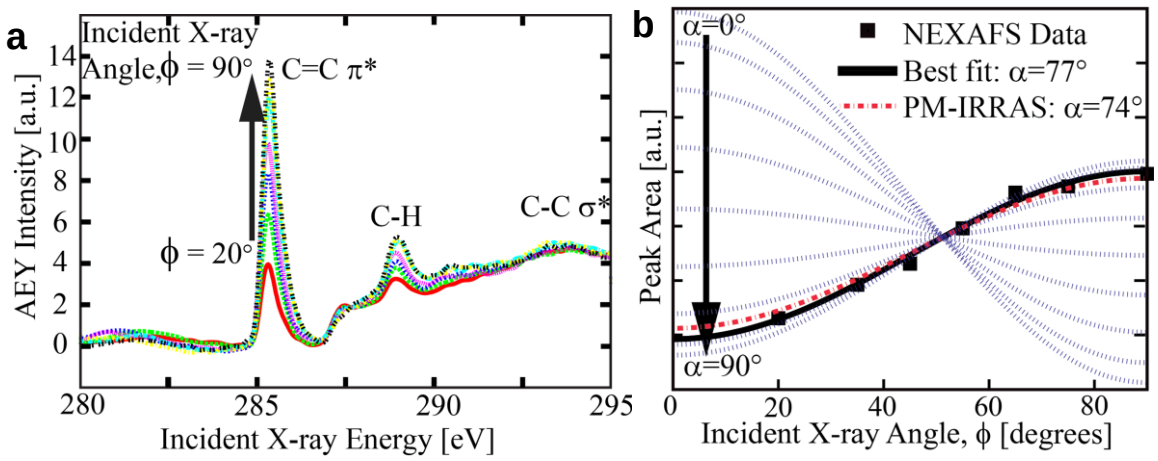

Figure 2.1. a) NEXAFS AEY spectra of PPA on IZO at various incident angles from 20-90°, the angular dependence of the C=C π* feature is highlighted. b) The angular dependence of the peak area under the C=C π* feature. Superposed are the model fits (Eq 2.2) for α = 0-90° in steps of 10° (dashed blue lines) as well as the best fit of the model to our data (solid black). The red dashed line represents the orientation given by the PM-IRRAS results discussed below. The data shown have been corrected for the angle-dependent IZO background, and processed as described in the methodolgy section 6.5.

2.2 NEXAFS

We first consider the molecular orientation as determined by NEXAFS. Figure 2.1a shows NEXAFS AEY spectra obtained at SSRL for PPA on IZO substrates for different incident x-ray angles, ϕ, from 20° to 90° (normal incidence). We assign the prominent peaks at 285.5 and 288.8 eV to transitions from the C1s to the π* antibonding orbital of the phenyl ring, and to features of the C-H bonds, respectively. Other notable features include transitions from the 1s to the C-C σ*

antibonding orbitals at 290-310 eV. All assignments are in good agreement with their expected positions.[24] The transition dipole moment for the C1s to π* anti-bonding orbital of the C=C bonds in an aromatic molecule is normal to the ring structure, and thus provides a convenient peak for determining the orientation of the molecular axis. The strong angular dependence of the C1s to C=C π* shows that the molecules adopt a preferred orientation relative to the surface. The angle that the transition dipole moment makes with the surface normal, α, can be determined quantitatively by analyzing the NEXAFS peak areas, I_v (ϕ), taken for different incident x-ray angles, ϕ (see eq 2.2).[24] We assume no preferred direction in the plane of the monolayer and thus average the data over azimuthal orientation.

$$I_v(\phi) \propto \frac{0.85}{3}\left(1+0.5(3\cos^2(\phi)-1)(3\cos^2(\alpha)-1)\right)+\frac{0.15}{2}\sin^2(\alpha) \qquad [2.2]$$

Figure 2.1b shows the integrated peak area for the C1s to C=C π* peak at 285.5 eV, along with sample curves showing the expected angular dependence for α = 0° to 90° in 10° steps for reference. The black solid line in Figure 2.1b is the best fit to the data, yielding an orientation of the phenyl ring normal of α = 77 ± 5° from the surface normal; from geometric considerations, this gives a tilt angle of the phenyl plane of 13 ± 5° from the surface normal, indicating that the phenylphosphonic acid is standing nearly vertically off the IZO surface.

As noted in section 6.5 of the methodology, the uncertainty ±5° is dominated by potential systematic errors associated with uncertainties in the background subtraction and uncertainty in beam polarization. The quoted uncertainty should not be interpreted as the range of angles which is accessible to a PPA molecule on the IZO surface. Rather, it is the statistical and systematic uncertainty in determining our result, which is a representative value of a distribution of orientations. The width of the distribution of orientations is related to molecule-molecule

variation due to surface roughness and, in this case, changes in binding mode. We note however, that while our surfaces are amorphous, they are very smooth as determined by AFM (RMS roughness < 0.5 nm, Appendix A) and are below the threshold where roughness effects were shown to emerge in studies of alkane phosphonic acids on indium tin oxide (ITO).[21] Nevertheless, these errors are relatively small, and the strong angle dependence of the data, along with the fact that our result is far from the magic angle (~54.7°) is indicative of a well-ordered system.[24] This orientation value is also in excellent agreement with the PM-IRRAS values (see below), further validating both our background subtraction methods, as well as the IR vibrational mode assignments that are discussed in detail in the next section. Though our main goal here is to determine tilt angle, comparison of NEXAFS and density functional theory calculations provide some insight into the nature of PPA-substrate interactions. A calculation performed for a layer of PPA molecules bonded to ITO at the low packing density of ~2.8×10^{13} molecules/cm^2 (as described in methodology section 6.15) suggest the presence of both tridentate and bidentate binding modes (Figure 2.5). The tridentate configuration is defined with all three oxygen atoms in the PO_3 moiety covalently bonded to metals and exhibits an orientation of 11-12°. The bidentate configuration, defined as two oxygen atoms in the PO_3 moiety covalently bonded to metals and the remaining hydrogen bonded to surface hydroxyls, exhibits an orientation of 15-22°. These values, especially the tridentate, are in excellent agreement with the NEXAFS result above and the PM-IRRAS results that follow. Further discussion of binding mode is discussed in Section 2.5.

Computed at the higher coverage density of ~1.1×10^{14} molecules/cm^2, we found that the largest change in the tilt angle for the four PPA molecules is only 6° in comparison with the low

coverage case, and the change in the average tilt angle for the four PPA molecules is only 1.5°. The good agreement between the DFT values for both coverages and our measured values indicates that ignoring intermolecular forces in the monolayer provides for a good first approximation in this system.

2.3 PM-IRRAS

PM-IRRAS measurements provide a valuable complement to the results from NEXAFS. In order to extract quantitative information about the orientation of surface-bound phosphonic acid molecules using PM-IRRAS, spectral lines arising from vibrational modes with well-defined transition dipole moments must first be identified. This requires selection of an appropriate model system for the surface-confined phosphonic acid as well as a thorough understanding of the vibrational behavior of the surface-confined molecules. Figures 2.2a and b show transmission IR spectra of KBr pellets of PPA and its disodium salt, PPA^{2-}, respectively. Section 6.11 in the methodology contains the important peak frequencies and their assignments.

The literature contains a thorough discussion of the vibrational spectroscopy of PPA.[18,41-47] However, given that we use the spectrum of PPA^{2-} as a model for the surface form of chemisorbed PPA on IZO surfaces (see below), we explore here the PPA^{2-} spectrum and differences in its spectrum compared to that of PPA. Upon full deprotonation of PPA, significant spectral changes include disappearance of the ν_s(POH) bands at 925 and 939 cm^{-1} and the ν(P-O) band at 1081 cm^{-1} from the $-PO_3H_2$ moiety, coupled with appearance of the $\nu_s(PO_3)$ bands from the PO_3^{2-} moiety between 1015 and 1080 cm^{-1}, and the corresponding $\nu_{as}(PO_3)$ bands appearing as a split multiplet between 1040 and 1160 cm^{-1}.[7,43-45,48] Also, the spectrum for PPA^{2-} does not

contain the band at 1220 cm^{-1}, which is present in the PPA spectrum, and corresponds to the free ν(P=O) vibration. The ν_{19b}, ν_{19a}, and ν_{8a} phenyl ring modes are present in the spectra for both PPA and PPA^{2-} near 1440, 1490, and 1590 cm^{-1},[49] respectively. The ν_{20b}, ν_2, and ν_{20a} C-H ring modes are also observed near 3020, 3060, and 3080 cm^{-1},[49] respectively, in both spectra.

Figure 2.2c shows the PM-IRRAS spectrum of IZO modified with a monolayer of PPA. It is noted that this spectrum (solid red line in Figure 2.2c) is shown on a y-axis scale in absorbance units; these absorbance values are obtained by proper conversion of the raw PM-IRRAS data as described in detail in the methodology section 6.11.[30-34] This spectrum is noticeably simpler than either of the spectra for PPA or PPA^{2-} due to the confluence of PPA orientation on the IZO surface and IRRAS surface selection rules from the underlying Au substrate. In the fingerprint region, only a single intense band centered at ~1150 cm^{-1} with asymmetry on the high energy side is observed. In addition, weak bands are also distinguishable at 997, 1017, 1438, 1491 and 1598 cm^{-1}. In the ν(C-H) region around 3000 cm^{-1}, only a single band is observed at 3060 cm^{-1}.

A cursory comparison of the spectra for PPA, PPA^{2-}, and the PPA-modified IZO surface indicates that the bands at 925 and 939 cm^{-1} in the PPA spectrum assigned to ν(P-O-H) modes are absent for PPA on the IZO surface, as is the band at 1220 cm^{-1} in the PPA spectrum assigned to the free ν(P=O) vibration. In the literature, the absence of these bands indicates the oxide surface-confined PPA exists in the PPA^{2-} form with either bidentate or tridentate binding to the oxide surface.[7,18,42,44,45,50]

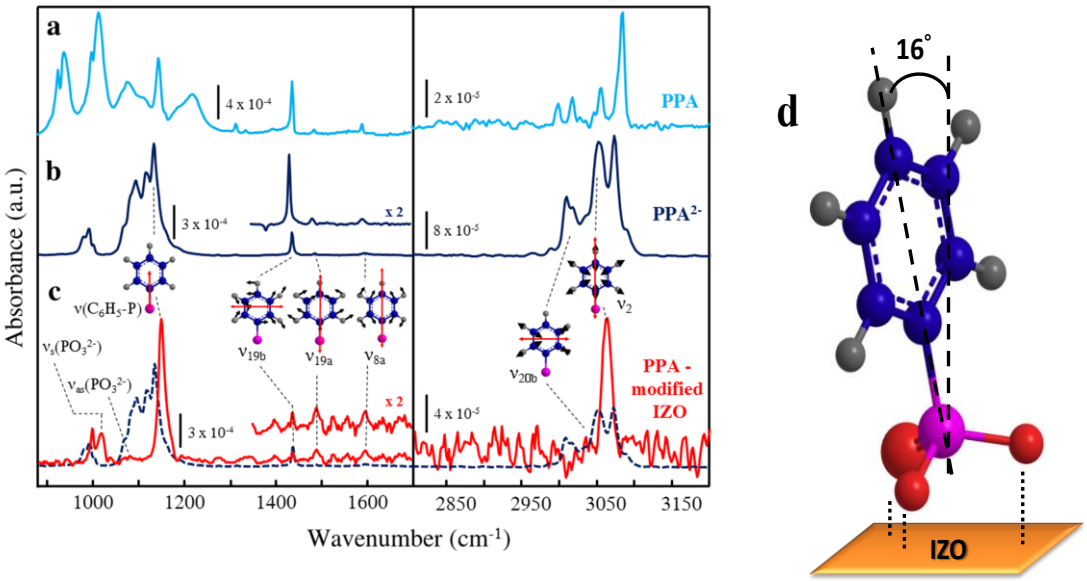

Figure 2.2. FTIR transmission spectra of a) PPA (aqua), and b) PPA^{2-} (dark blue), c) PM-IRRAS spectrum of PPA-modified IZO (red) and calculated spectrum for 7.4 Å-thick isotropic PPA^{2-} layer (dark blue dashed), and d) proposed orientation for PPA on IZO from PM-IRRAS.

Further consideration of the spectrum of PPA on the IZO surface reveals that the intense mutiplet of bands between 1060 and 1100 cm^{-1} assigned to $\nu_{as}(PO_3^{2-})$ modes in the PPA^{2-} spectrum is absent from the PM-IRRAS spectrum; we expect this vibration in the vicinity of 1090-1100 cm^{-1} based on the spectral behavior of metal phosphonates.[51,52] The ν_{19b}, ν_{19a}, and ν_{8a} normal phenyl ring modes, near 1440, 1490, and 1590 cm^{-1} respectively,[49] appear in all three spectra shown in Figure 2.2, but the ν_{19b} is especially weak and the ν_{19a} is enhanced in the spectrum of surface PPA. The ν_{20b}, ν_2, and ν_{20a} C-H modes are observed near 3020, 3060, and 3080 cm^{-1}, respectively.[49] The ν_{20a} and ν_{20b} bands are also especially weak in the spectrum of

surface PPA. We hypothesize that these low intensities to be the result of IRRAS surface selection rules and the high degree of order in the PPA monolayer on the IZO surface.

The presence of oriented electric fields at the surface of the IZO/Au substrate allows evaluation of the PM-IRRAS spectral data quantitatively, so that an average tilt angle for the PPA molecules on the IZO surface can be determined. Previous vibrational spectroscopy studies of PPA on a variety of metal oxide substrates have collectively resulted in two conclusions about surface binding and orientation:[18,43,44,53] (1) the spectral signature for oxide-bound PPA is similar to that of PPA^{2-} and the metal phosphonates; and (2) qualitatively, the molecule is oriented in a largely upright position. However, no studies have quantitatively established the average tilt angle of the molecular axis for a phosphonic acid on any metal oxide using PM-IRRAS.

Comparing previous studies and the data reported here, we emphasize the importance of the type of IR spectroscopy used to acquire the spectral data. For example, in several previous studies, simple transmission or diffuse reflectance FTIR spectroscopies were utilized to investigate phosphonic acid layers on oxide particles or powders.[42-44,50] In these studies, all IR-allowed vibrational modes of the phosphonic acid surface species are observed in the surface spectra. In contrast, due to the existence of surface selection rules in IRRAS studies at reflective metal substrates,[7,18] certain IR-allowed vibrational bands may disappear from a spectrum depending on the orientation of the molecule with respect to the surface. We use the observed IRRAS intensities resulting from the operation of these surface selection rules at IZO-covered Au substrates to extract the average molecular tilt angle for monolayers of PPA on IZO.

We now proceed to interpret the IRRAS data in order to determine the average molecular tilt angle. We define the tilt angle as the angular deviation of the molecular axis, the line through the

P atom-C1-C4 ring atoms, from the surface normal. In order to determine average molecular orientation within the modifier layer, the experimental IR absorbance spectrum calculated by conversion of the baseline-corrected PM-IRRAS data as described above must be compared to a spectrum that is calculated for an isotropic film of comparable thickness. This is accomplished according to published protocols[54,55] as described in methodology section 6.11. The spectrum for an isotropic layer of absorber of a given thickness is calculated using a three-phase model, as reported previously.[54,55] For the PPA monolayer on IZO, we use a thickness of 7.4 Å as determined from x-ray crystallographic data for related metal phosphonates[56-59] and theory.[13] Figure 2.2c shows the calculated spectrum for an isotropic layer of PPA of this thickness as the dashed line. With the calculated spectrum of an isotropic layer in hand, subsequent data analysis starts from the assumption that the surface-bound PPA exists as the PPA^{2-} form, such that any differences in intensities between the IRRA spectrum and the calculated spectrum for vibrational modes with transition dipole moments along different coordinates indicate a preferred orientation of the surface-bound molecules. From these relative intensity changes, the average orientation of surface-confined molecules is deduced as follows.

For a collection of oriented surface molecules in an external-reflection geometry, there is electric field amplitude at infrared frequencies only normal to the surface. Thus, the integrated absorbance for a vibrational band is proportional to the square of the electric field amplitude at the surface, the magnitude of the transition dipole moment (μ), and the tilt angle θ of μ from the surface normal:[60]

$$A \propto (\mu \cdot \cos\theta)^2 \qquad [2.3]$$

As shown by Hansen[54] and McIntyre,[55] due to this anisotropy of surface electric field amplitude, the integrated absorbance of a mode with a transition moment oriented along the surface normal will be three times as large as the integrated absorbance of the same vibrational band for an isotropic collection of identical molecules in a thin film of equivalent thickness and molecular density. Thus, the tilt angle of a given transition dipole moment can be calculated using:

$$\cos\ \theta = \frac{A_{film}}{3 \cdot A_{simulated}} \qquad [2.4]$$

Here, A_{film} is the integrated absorbance of a PPA band from the IZO surface spectrum. In order to properly ratio A_{film} to the value of $A_{simulated}$, the integrated absorbance of the identical PPA^{2-} band from the calculated spectrum for an isotropic thin film of comparable thickness, both A_{film} and $A_{simulated}$ must be corrected for molecular density. For A_{film}, this requires a value for surface coverage of PPA on the oxide as well as a monolayer thickness. Here we use a surface number density of 1.56×10^{14} molecules/cm^2 for monolayer coverage from past experimental studies of alkylphosphonic acids and related systems[7,17,18] and a monolayer thickness of 7.4 Å as determined from x-ray crystallographic data for related metal phenylphosphonates[56-59] and theory.[13] $A_{simulated}$ is the integrated absorbance of the identical PPA^{2-} band from the calculated spectrum for an isotropic thin film of comparable thickness, corrected for a bulk molecular density of 1.6 g/cm^3.[59]

Quantification of the average tilt angle for PPA molecules on IZO requires identification of appropriate vibrational modes. Suitable spectral bands for this purpose are those which arise from a vibrational mode with a well-defined transition dipole moment, are spectrally well-

isolated and clearly identifiable, and are not complicated by splitting. The latter requirement eliminates use of the $\nu_s(PO_3^{2-})$ and $\nu_{as}(PO_3^{2-})$ bands, since they exhibit significant splitting in the spectrum of the model PPA^{2-} and similar metal phosphonates. Spectral bands that meet these requirements are those corresponding to vibrations of the phenyl ring and the C_6H_5-P stretch. The ν_{19b}, ν_{19a}, and ν_{8a} phenyl ring modes near 1440, 1490, and 1590 cm^{-1}, respectively,[49] are excellent choices for tilt angle determination. Each of these vibrations is an in-plane ring vibration with the well-defined transition dipole moments shown on the spectrum in Figure 2.2c. Moreover, these modes are close in frequency and are spectrally discrete, and hence, their utility for tilt angle determination.

As noted above, the ν_{19b} mode is especially weak in the surface spectrum for PPA on IZO. This observation immediately suggests that the molecules are oriented such that the transition moment for this mode is largely parallel to the surface. However, given that the transition moment for this mode is orthogonal to the molecular axis, little insight into tilt angle of the molecular axis can be deduced from this conclusion, since PPA could be oriented at a range of tilt angles from 0 to 90° while still maintaining the transition moment of the ν_{19b} mode parallel to the surface. Thus, we exclude this band from further consideration, and proceed to compute the tilt angle here using the ν_{19a} and ν_{8a} phenyl modes along with the $\nu(C_6H_5\text{-P})$ mode.

Using the $\nu(C_6H_5\text{-P})$ mode for tilt angle quantification relies on its unambiguous assignment in the surface spectrum. The 1150 cm^{-1} band in the surface spectrum can be fit to two bands with maxima at 1149 and 1166 cm^{-1}, but the assignment of these bands has been controversial in the literature. The more intense of the two bands has been previously assigned to either the $\nu(C_6H_5\text{-P})$[18,43,44] or the $\nu(P{=}O)_{associated}$[45]. Given that the transition dipole moments of these modes are

almost orthogonal, both assignments cannot be correct. We proceed here on the assumption (based on recent density functional theory calculations of the vibrational spectroscopy of PPA[46,47]) that the 1140 cm^{-1} band arises from a combination of the $\nu(C_6H_5\text{-}P)$ and in-plane ring modes, all with transition dipole moments largely parallel to the molecular axis. We validate this assumption by checking the consistency of the results calculated using this vibrational band with those calculated with other bands with similarly oriented transition dipole moments, as well as against the orientations determined by NEXAFS as described above.

To summarize, the three modes that are used for tilt angle determination are the ν_{19a} and ν_{8a} phenyl modes and the $\nu(C_6H_5\text{-}P)$ mode, all of which have transition moments along the molecular axis. Utilizing integrated areas determined from peak fitting of the PPA surface spectrum and the PPA^{2-} calculated spectrum, and in the case of the $\nu(C_6H_5\text{-}P)$ band, spectral decomposition of the complex multiplet envelope in the calculated PPA spectrum, Eq. 2.3 can be used to determine the tilt angle, θ. Table 2.1 summarizes the results of orientation analysis from these three spectral bands. Tilt angles of 16, 16 and 15° are determined from analysis of the spectral intensities from the $\nu(C_6H_5\text{-}P)$, ν_{19a}, and ν_{8a} modes, respectively.

From this collective analysis, an average tilt angle of 16 ± 1° is calculated (Figure 2.2d), which is in excellent agreement with the value of the angle of the ring plane with respect to the surface normal of 13 ± 5° determined from the NEXAFS, as described above, as well as the theoretically calculated value of 11-12° for PPA on ITO for low surface coverage. As with NEXAFS, this uncertainty should not be interpreted as the range of orientations each PPA molecule can adopt relative to the surface. This uncertainty reflects the confidence interval in the average orientation adopted by a PPA molecule on the surface. The width of the distribution is

inaccessible to us, and can be affected by surface roughness. We further note that the agreement of the tilt angle calculated using the $\nu(C_6H_5\text{-}P)$ band at 1149 cm^{-1} serves both to validate our peak assignment and analysis procedures, while also resolving discrepancies of this peak assignment in the literature.

Table 2.1. PM-IRRAS and calculated spectral data from Figure 3 in text for determination of PPA tilt angle.

Frequency (cm^{-1})	Assignment	Simulated Spectrum Integrated Abs. (a.u.-cm^{-1})	Surface Spectrum Integrated Abs. (a.u.-cm^{-1})	θ
1149	$\nu(C_6H_5\text{-}P)$	0.0080	0.022	16°
1491	ν_{19a}	0.000074	0.00021	16°
1598	ν_{8a}	0.00012	0.00033	15°

2.4 UPS

Ultraviolet photoemission spectroscopy (UPS) was used to measure the work function and characterize the valence band density of states of the oxygen plasma treated IZO soaked in ethanol. Figure 2.3 shows the UPS spectrum (left panel) and estimated energy band diagrams (right panel) of the unmodified substrate on a binding energy scale relative to the Fermi level, calibrated to the Fermi edge of a freshly sputtered gold foil. UPS spectra and band diagrams are shown for the unmodified substrate (Figures 2.3a and 2.3c) and upon modification of the IZO with PPA (Figures 2.3b and 2.3d). The work function was determined by the position of the half

height of the secondary electron cutoff with respect to gold. We obtained the valence band maximum using linear extrapolation of the leading edge of the O 2p band, whereas the ionization potential was defined as the onset of the low density of mid-gap states that extend from the valence band into the band gap, typical in amorphous oxides. These final state effects have often been associated with extensive disorder within the system, implying a poorly defined oxygen sub-lattice and a lack of long range order.[61]

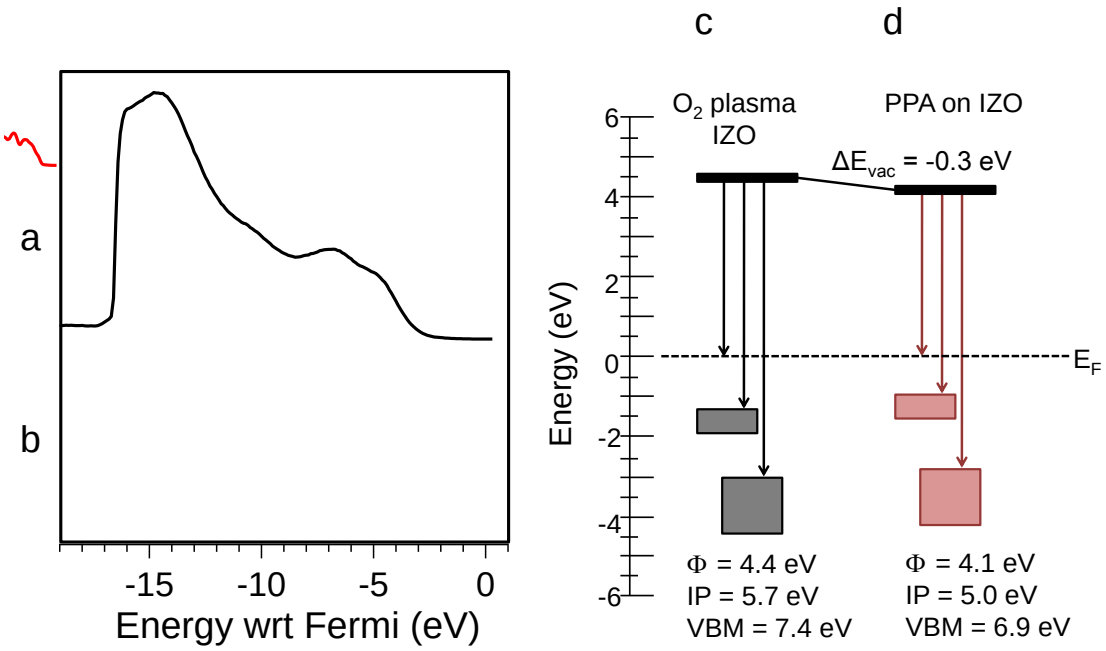

Figure 2.3. Ultraviolet photoemission spectroscopy (UPS) of (a) O_2-plasma treated IZO soaked in ethanol and (b) PPA-modified IZO. (c,d) Energy band diagram inferred from the spectra in (a,b).

In Figure 2.3a, the UPS demonstrates typical metal oxide valence structure with oxygen 2pσ and 2pπ orbitals at ~4eV and ~7eV binding energy, respectively. A subtle feature at ~10 eV below the Fermi level is indicative of the Zn 3d valence peaks. A work function of 4.4 eV and a valence band maximum of 7.4eV (Figure 2.3c) is found for unmodified plasma cleaned IZO, in agreement with the literature.[62]

Modification of the IZO with the PPA results in a significant change in the UPS spectrum of the oxide. New features appear in the UPS spectrum, attributed to the C 2p band of the aromatic ring at ~9 eV below the Fermi level (Figure 2.3c). Modification does not eliminate the presence of the mid-gap states, but does appear to decrease the net density at the near surface-composition, shifting the onset closer to the Fermi level. There is a negative shift in the secondary electron cutoff, yielding a work function of 4.1 eV. Conversely, the valence band maximum is found at 6.9 eV (Figure 2.3d), approaching the Fermi level relative to the native oxide. Such changes to the local density of states that comprise the valence band may have direct impact on the relative rates of free carrier injection (OLEDs) and extraction (OPVs), aside from a simple modification of the work function.

Table 2.2: Density functional theory calculated binding geometries for PPA on indium tin oxide.

Binding Mode	Tilt angle (°)	P-O bond length (Å)			O-In(Sn) bond length (Å)		
Tridentate	12	1.57	1.54	1.55	2.13	2.16	2.33
Tridentate	11	1.58	1.53	1.56	2.21	2.31	2.25
Bidentate	15	1.55	1.59	1.56	2.25	2.21	--
Bidentate	22	1.56	1.59	1.53	2.31	2.24	--

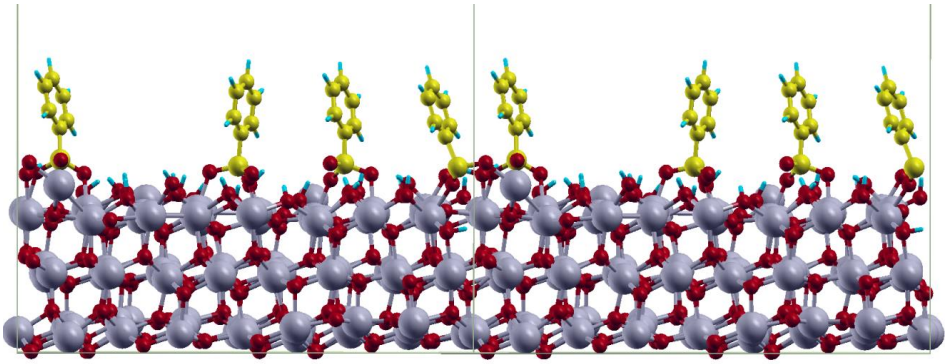

Figure 2.4. Structure showing four PPA molecules adsorbed on one unit cell of the ITO surface, with grey solid lines indicating the boundaries of each unit cell.

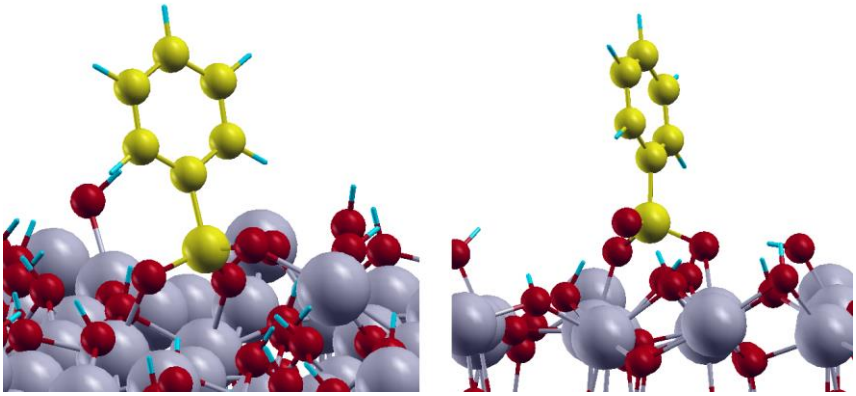

(a) (b)

Figure 2.5. Side view of tridentate binding (a) and bidentate binding (b) geometries of PPA molecules on the ITO surface.

2.5 Discussion of binding geometry

The published literature on the binding mode of phosphonic acids to metal oxide surfaces is somewhat contradictory.[63-66] We believe our system of PPA on IZO to exhibit a mixture of bidentate and tridentate binding geometries, with the majority being tridentate. We can examine this idea using first a combination of our NEXAFS results and DFT calculations. Table 2.2 gives the results of the calculation, which suggest that in the tridentate binding mode PPA has a narrow distribution of orientations of 11-12° while in the bidentate binding mode PPA has a wider distribution of orientations from 15-22°. We note that if there is a non-trivial distribution of angles, the NEXAFS data give the expected value of $\cos^2(\theta)$ for this distribution.[24] The surface roughness will affect the width of this distribution. The measured orientation represents a convolution of the orientation relative to a local surface normal with the distribution of orientations of the local surface normals relative to a global or average surface normal. This

convolution will lead to an actual orientation which is more upright than the measured value. This is discussed in greater detail in chapter 3. Unlike alkylphosphonic acids, which crystalize[21], we expect to see a non-trivial distribution of angles even on a perfectly smooth surface, due to variations in binding mode and low inter-molecular forces. One cannot specify a unique distribution of angles using a NEXAFS measurement. We interpret quantitative agreement with the calculated orientation for the tridentate binding mode as indicative of a narrow distribution of orientations given by a predominantly tridentate population. If we make a simplistic assumption that the SAM comprises two sub-populations, one ordered at the theoretically predicted angle for tridentate binding, and one completely disordered, then the maximum possible "disordered" fraction of the film, given our uncertainty, is 18%, with the fraction of the film "ordered" at 12° as 82%.

We also use the PM-IRRAS spectrum of PPA on IZO, shown in Figure 2.2c to examine our interpretation of predominantly tridentate bonding. First, the absence of the ν_s(POH) mode in this spectrum implies at least bidentate binding, since monodentate binding would require the presence of at least one P-OH moiety.[67] The disappearance of the ν(P=O) band, present in the spectra in Figures 2.2a and b at 1260 cm^{-1}, is also strong evidence for coordination of the phosphoryl group to the surface in a configuration that involves bidentate or tridentate binding.

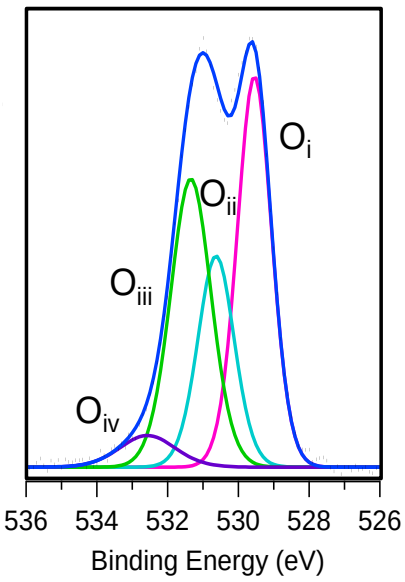

Figure 2.6. O 1s core spectrum of the IZO surface control: O_2-plasma treated, soaked in ethanol. Chemical contributions from different components (O_i-O_{iv}) are discussed in the text.

Table 2.3. Binding energies and relative near-surface compositions for the species in Figure 2.6. Chemical contributions from different components (O_i-O_{iv}) are discussed in the text.

Peak	Binding Energy (eV)	Percent Composition
O_i	529.5	38.9
O_{ii}	530.6	22.2
O_{iii}	531.3	33.8
O_{iv}	532.6	5.1

Lastly, we would like to examine XPS data in this same context. Such characterization was a multi-step process and includes contributions from the PPA on IZO as well as the neat PPA and salt of PPA^{2-}. In order to effectively discuss the XPS results in the context of binding mode, we must first discuss the contributions in each of the spectra.

Figure 2.6 gives the O 1s core level spectrum for the IZO surface that has been oxygen plasma treated for 10 minutes followed by soaking in ethanol for one week. As both ITO and

IZO are predominantly In (>90%), a previously described model for the O 1s surface states of ITO was extrapolated to the O 1s near-surface composition of the thin film amorphous IZO.[68]

Table 2.3 gives the binding energies and relative compositors for each of the peaks in Figure 2.6. Peak O_i (~529.5 eV) is attributed to In_2O_3-like oxygen and peak O_{ii} is associated with defect states (oxygen vacancy-like species) which contribute to the conductivity of the oxide (~530.6 eV).[3] Peak O_{iii} is the near-surface contribution from hydroxide and/or oxy-hydroxide species, correlating well with standards for InOOH (531.2 eV) and $In(OH)_3$ (531.3 eV). Finally, peak O_{iv} is due to adventitious contaminants or to final state effects, as with ITO (532.6 eV). These results confirm that the surface chemistry of the oxide is complex and must be considered when modifying the oxide with the PPA.

Figure 2.7 a-c shows the high resolution XPS for O 1s, C 1s and P 2p spectra for PPA on IZO, respectively. Binding energies were referenced to the C 1s core level at 284 eV (Figure 2.7b). Binding energies and relative percent compositions for the fits are given in Table 2.4. The O 1s data for the PPA attached to the IZO has five components (Figure 2.7a), with components i-iv consistent with those of the native oxide in Figure 2.6a. However, there is clear evidence for a new feature at 531.0 eV, O_v, indicative of the phosphoryl moiety.[69-71] Previous theoretical calculations have predicted the binding energies of the O 1s peaks for three different binding modes of the phosphonic acid,[17] referenced to the well-documented In_2O_3-like peak at 529.5 eV.[68] The first binding mode involves bidentate binding of PPA with two In atoms while the P=O bond remains unbound. The PO_3 oxygen atoms participating in the bonding are predicted to exhibit O 1s binding energies of 530.2-530.4 eV, while the unbound O atom has binding energy 530.9 eV. A second form of bidentate bonding has metal-oxygen geometries that include the

P=O bond and involve additional hydrogen bonding between the PO_3 moiety and the surface (P-O···H-O). In this case, we predict relative binding energies for all three oxygen atoms to be in the range of 530.6 to 530.8 eV. Finally, we predict true tridentate bonding of PO_3^{2-} groups to exhibit O 1s binding energies of 530.4 to 530.8 eV. Furthermore, from the O 1s spectrum of Figure 2.7, we may conclude that the near-surface region is not comprised exclusively of phosphonic acid modifier (O_v) and that there is direct competition of binding sites with surface hydroxyls (O_{iii}) and waters of hydration (O_{iv}).

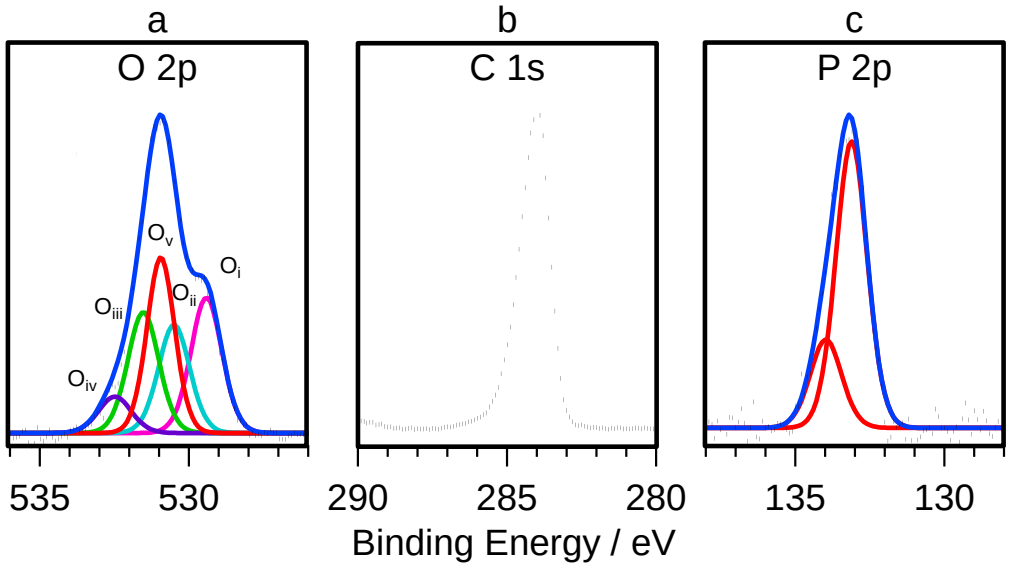

Figure 2.7. High-resolution XPS spectra of O2-plasma treated IZO modified with PPA (a) O 1s, (b) C 1s and (c) P 2p spectra. Components Oi-Ov are discussed in the text.

Insight into the local electronic environment of constituent atoms and how these environments change between PPA and the PPA^{2-} salt is also useful to understanding the average binding mode of the PPA. Figure 2.8 shows high resolution spectra acquired on films of solid

powders for the O 1s (Figures 2.8a and c) and P 2p (Figures 2.8b and d) core levels for PPA and the disodium salt of PPA^{2-}. Table 2.4 provides the relative compositions and binding energies of these features.

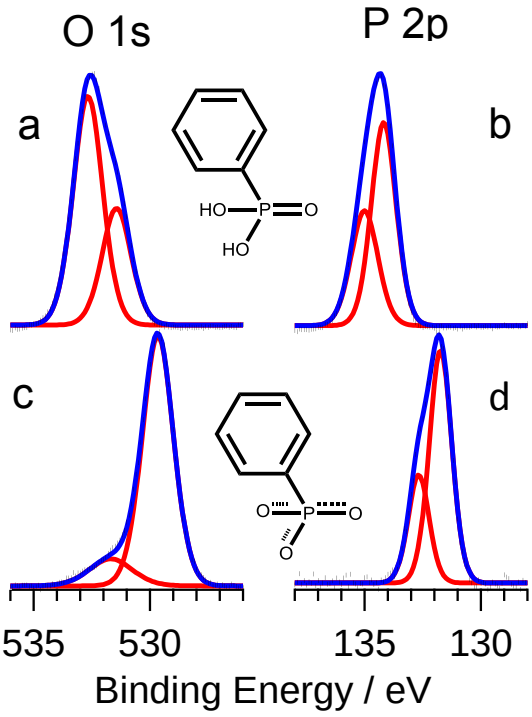

Figure 2.8. High resolution XPS spectra of the O 1s (a,c) and P 2p (b,d) peaks for neat PPA (a,b) and PPA^{2-} (c,d).

Table 2.4. Binding energies (BE) and relative near-surface compositions (% Comp) for the XPS spectra in Figure 2.7 (Top) and 2.8(Bottom)

	PPA on IZO	
Peak	BE (eV)	% Comp
O 1s i	529.4	24.2
O 1s ii	530.5	19.4
O 1s iii	531.6	21.6
O 1s iv	532.5	6.9
O 1s v	531.0	27.9
P $2p_{3/2}$	133.1	66.7
P $2p_{1/2}$	134.0	33.3

	PPA neat		PPA^{2-}	
Peak	BE (eV)	% Comp	BE (eV)	% Comp
O 1s P=O	531.4	35.6	N/A	N/A
O 1s P-OH	532.7	66.4	N/A	N/A
O 1s PO_3^{2-}	N/A	N/A	529.7	87.0
O 1s H_2O	N/A	N/A	531.7	13.0
P $2p_{3/2}$	134.2	66.7	131.7	66.7
P $2p_{1/2}$	135.0	33.3	132.7	33.3

The O 1s spectrum of PPA in Figure 2.8a shows evidence for two oxygen environments: the phosphoryl oxygen exhibits a peak at a binding energy of 531.4 eV[71] while the two oxygen atoms of the P-OH groups exhibit a binding energy of 532.7 eV.[71] The ratio of the phosphoryl oxygen peak area to the P-OH oxygen peak area is 1:2 as expected. For the PPA^{2-} salt, we expect a single O 1s band due to resonance stabilization, which makes all three oxygen atoms equivalent with a partial of charge (δ) of -2/3. The increased electron density on these oxygen atoms resulting from their partial negative charge should decrease the binding energy of their O 1s electrons; thus, we assign the O 1s peak at 529.7 eV to these oxygen atoms.[70] However, there is a clear tail on the high binding energy edge of this band at 531.7 eV indicative of a second O 1s environment. Given the relatively low intensity of this peak, we assign it to waters of hydration in the PPA^{2-} disodium salt structure, consistent with observed waters of hydration in other phosphonate species in the literature.[56-59,72-74] The relative intensities of these two O 1s bands suggest that approximately one water of hydration is shared between two PPA^{2-} species, or a molecular formula of approximately $C_6H_5PO_3Na_2 \bullet 0.5\ H_2O$.

The P 2p peak is a doublet composed of the $2p_{3/2}$ and higher binding energy $2p_{1/2}$ peaks with a ratio of 2:1, as predicted from spin-orbit splitting. We find that the binding energies systematically decreased upon deprotonating from PPA to PPA^{2-}, which is consistent with increased electron density on the phosphorus upon formation of the weak Lewis base species.

Interpretation of the local environment involved in binding is extremely complicated in XPS, due predominantly to the signal overlap from multiple near-surface components of the oxide (Figures 2.6,2.7). However, clear insight into local changes in electron density is achieved via

comparison with the salts, shown in Figure 2.8. First, in Figure 2.7, the O_V and P2p peaks are shifted slightly negative of the corresponding components of the fully protonated salt (PPA) in Figure 2.8a. Differences in relative binding energy of PPA on IZO to neat PPA indicate that binding to the surface increases the net electron density of the PO_3 moiety. Second, an increase in relative electron density could be due to (a) a difference in the strength of the ionic nature of the P-O-H bond compared to the P-O-In bond (implies bidentate or tridentate), (b) complete loss of P=O character to form three P-O-M bonds (implies tridentate), or (c) transition from P=O to more P-O like, via formation of P-O…H-O with surface hydroxyls (implies bidentate).

Also, from Figures 2.7 and \2.8c, we observe that the O_v peak is higher in binding energy than the O 1s for PPA^{2-}, and likewise, the P 2p in Figure 2.7c has a slightly higher binding energy than the P 2p in Figure 2.8d. This indicates that the PO_3 moiety has a lower net electron density upon binding to the surface than the fully deprotonated derivative (PPA^{2-}). The lower electron density is hypothesized to be via donation to Lewis acid cationic metal centers on the IZO. Lastly, there are still a significant number of hydroxyls on the surface, implying that either there is (a) tridentate binding with hydroxyls in between tethered molecules (Figure 2.5a) or (b) bidentate binding with hydrogen bonding with the hydroxyls on the surface (Figure 2.5b). From the XPS results, we can suggest that the surface is composed of tridentate and bidentate bonding, comprised of both metal-oxygen and hydrogen bonding species. This is in direct agreement with both the theoretical and vibrational spectroscopic results on this system.

2.6 Conclusions

We have determined orientation of a model SAM, phenylphosphonic acid, on a smooth transparent conductive oxide, IZO, using NEXAFS and PM-IRRAS. Surprisingly, these populations have a well-defined orientation, with the phenyl ring plane tilted at an angle of 15 ± 4° from the surface normal, given by the uncertainty-weighted average of the NEXAFS and PM-IRRAS experiments, in quantitative agreement with DFT calculations for PPA on ITO for low surface coverage. The fact that these molecules form well-oriented SAMs may help explain why these molecules have found notable success in surface modification for organic electronics device applications requiring high quality thin films.

Experimentally, the combination of both NEXAFS and PM-IRRAS was critical to determining the molecular orientation with confidence. We anticipate that the cross-validation of protocols for analyzing phosphonic acids on transparent conductive oxides provided by this study will enable more rapid future studies of these useful compounds with a high degree of confidence under a range of conditions. Notably, as part of these studies, we were able to correct earlier vibrational peak assignments in the IR spectra of phosphonic acids that are critical to determining molecular orientation via IRRAS.

Finally, we note that the excellent agreement between the experimental and theoretically predicted tilt angles is particularly striking considering that the simulations involved only non-interacting phenylphosphonic acid molecules. This agreement suggests that the phenylphosphonic acid tilt angle is dominated by the substrate/phosphonic acid interaction rather than intermolecular interactions. It will be interesting for future experiments to determine at what

point intermolecular interactions begin to alter the orientation of aromatic phosphonic acid SAMs bound to metal oxides.

2.7 References

1. Sharma, A.; Haldi, A.; Hotchkiss, P. J.; Marder, S. R.; Kippelen, B. Effect of Phosphonic Acid Surface Modifiers on the Work Function of Indium Tin Oxide and on the Charge Injection Barrier into Organic Single-Layer Diodes. *J. Appl. Phys.* **2009**, *105*, 074511-074516.

2. MacLeod, B. A.; Horwitz, N. E.; Ratcliff, E. L.; Jenkins, J. L.; Armstrong, N. R.; Giordano, A. J.; Hotchkiss, P. J.; Marder, S. R.; Campbell, C. T.; Ginger, D. S. Built-In Potential in Conjugated Polymer Diodes with Changing Anode Work Function: Interfacial States and Deviation from the Schottky–Mott Limit. *J. Phys. Chem. Lett.* **2012**, *3*, 1202-1207.

3. Knesting, K. M.; Hotchkiss, P. J.; MacLeod, B. A.; Marder, S. R.; Ginger, D. S. Spatially Modulating Interfacial Properties of Transparent Conductive Oxides: Patterning Work Function with Phosphonic Acid Self-Assembled Monolayers. *Adv. Mater.* **2012**, *24*, 642-646.

4. Miozzo, L.; Yassar, A.; Horowitz, G. Surface Engineering for High Performance Organic Electronic Devices: the Chemical Approach. *J. Mater. Chem.* **2010**, *20*, 2513-2538.

5. Beaumont, N.; Hancox, I.; Sullivan, P.; Hatton, R. A.; Jones, T. S. Increased Efficiency in Small Molecule Organic Photovoltaic Cells Through Electrode Modification with Self-Assembled Monolayers. *Ener. Environ. Sci.* **2011**, *4*, 1708-1711.

6. Bulliard, X.; Ihn, S. G.; Yun, S.; Kim, Y.; Choi, D.; Choi, J. Y.; Kim, M.; Sim, M.; Park, J. H.; Choi, W.; Cho, K. Enhanced Performance in Polymer Solar Cells by Surface Energy Control. *Adv. Funct. Mater.* **2010**, *20*, 4381-4387.

7. Paniagua, S. A.; Hotchkiss, P. J.; Jones, S. C.; Marder, S. R.; Mudalige, A.; Marrikar, F. S.; Pemberton, J. E.; Armstrong, N. R. Phosphonic acid Modification of Indium-Tin Oxide Electrodes: Combined XPS/UPS/Contact Angle Studies. *J. Phys. Chem. C* **2008**, *112*, 7809-7817.

8. Park, L. Y.; Munro, A. M.; Ginger, D. S. Controlling Film Morphology in Conjugated Polymer: Fullerene Blends with Surface Patterning. *J. Amer. Chem. Soc.* **2008**, *130*, 15916-15926.

9. Wei, J. H.; Coffey, D. C.; Ginger, D. S. Nucleating Pattern Formation in Spin-Coated Polymer Blend Films with Nanoscale Surface Templates. *J. Phys. Chem. B.* **2006**, *110*, 24324-24330.

10. DeLongchamp, D. M.; Kline, R. J.; Fischer, D. A.; Richter, L. J.; Toney, M. F., Molecular Characterization of Organic Electronic Films. *Adv. Mater.* **2011**, *23*, 319-337.

11. Hotchkiss, P. J.; Li, H.; Paramonov, P. B.; Paniagua, S. A.; Jones, S. C.; Armstrong, N. R.; Bredas, J.- L.; Marder, S. R. Modification of the Surface Properties of Indium Tin Oxide with Benzylphosphonic Acids: A Joint Experimental and Theoretical Study. *Adv. Mater.* **2009**, *21*, 4496-4501.

12. Heimel, G.; Romaner, L.; Zojer, E.; Bredas, J.-L. The Interface Energetics of Self-Assembled Monolayers on Metals. *Accounts Chem. Res.* **2008**, *41*, 721-729.

13. Cecchet, F.; Lis, D.; Guthmuller, J.; Champagne, B.; Fonder, G.; Mekhalif, Z.; Caudano, Y.; Mani, A. A.; Thiry, P. A.; Peremans, A. Theoretical Calculations and Experimental Measurements of the Vibrational Response of p-NTP SAMs: An Orientational Analysis. *J. Phys. Chem. C* **2010**, *114*, 4106-4113.

14. Hotchkiss, P. J.; Jones, S. C.; Paniagua, S. A.; Sharma, A.; Kippelen, B.; Armstrong, N. R.; Marder, S. R. The Modification of Indium Tin Oxide with Phosphonic Acids: Mechanism of Binding, Tuning of Surface Properties, and Potential for Use in Organic Electronic Applications. *Accounts Chem. Res.* **2012**, *45*, 337-346.

15. Vericat, C.; Vela, M. E.; Benitez, G.; Carro, P.; Salvarezza, R. C. Self-Assembled Monolayers of Thiols and Dithiols on Gold: New Challenges for a Well-Known System. *Chem. Soc. Rev.* **2010**, *39*, 1805-1834.

16. Wood, C.; Li, H.; Winget, P.; Brédas, J.-L. Binding Modes of Fluorinated Benzylphosphonic Acids on the Polar ZnO Surface and Impact on Work Function. *J. Phys. Chem. C*, **2012**, *116*, 19125-19133.

17. Li, H.; Paramonov, P.; Bredas, J.-L. Theoretical Study of the Surface Modification of Indium Tin Oxide with Trifluorophenyl Phosphonic Acid Molecules: Impact of Coverage Density and Binding Geometry. *J. Mater. Chem.* **2010**, *20*, 2630-2637.

18. Koh, S. E.; McDonald, K. D.; Holt, D. H.; Dulcey, C. S.; Chaney, J. A.; Pehrsson, P. E. Phenylphosphonic Acid Functionalization of Indium Tin Oxide: Surface Chemistry and Work Functions. *Langmuir* **2006**, *22*, 6249-6255.

19. Crispin, X.; Geskin, V.; Crispin, A.; Cornil, J.; Lazzaroni, R.; Salaneck, W. R.; Bredas, J.-L. Characterization of the Interface Dipole at Organic/ Metal Interfaces. *J. Amer. Chem. Soc.* **2002**, *124*, 8131-8141.

20. Koch, N. Energy Levels at Interfaces Between Metals and Conjugated Organic Molecules. *J. Phys. Condens. Matter* **2008**, *20*, 184008-1840019.

21. Losego, M. D.; Guske, J. T.; Efremenko, A.; Maria, J. P.; Franzen, S. Characterizing the Molecular Order of Phosphonic Acid Self-Assembled Monolayers on Indium Tin Oxide Surfaces. *Langmuir* **2011**, *27*, 11883-11888.

22. Kang, J. W.; Jeong, W. I.; Kim, J. J.; Kim, H. K.; Kim, D. G.; Lee, G. H. High-Performance Flexible Organic Light-Emitting Diodes Using Amorphous Indium Zinc Oxide Anode. *Electrochem. Solid-State Lett.* **2007**, *10*, J75-J78.

23. Cheun, H.; Kim, J.; Zhou, Y.; Fang, Y.; Dindar, A.; Shim, J.; Fuentes-Hernandez, C.; Sandhage, K. H.; Kippelen, B. Inverted Polymer Solar Cells with Amorphous Indium Zinc Oxide as the Electron-Collecting Electrode. *Optics Express* **2010**, *18*, A506-A512.

24. Stöhr, J. *NEXAFS spectroscopy*; Springer-Verlag: Berlin, 1992.

25. Dubey, M.; Weidner, T.; Gamble, L. J.; Castner, D. G. Structure and Order of Phosphonic Acid-Based Self-Assembled Monolayers on Si(100). *Langmuir* **2010**, *26*, 14747-14754.

26. Willey, T. M.; Lee, J. R. I.; Fabbri, J. D.; Wang, D.; Nielsen, M. H.; Randel, J. C.; Schreiner, P. R.; Fokin, A. A.; Tkachenko, B. A.; Fokina, N. A.; et al. Determining Orientational Structure of Diamondoid Thiols Attached to Silver Using Near-Edge X-ray absorption Fine Structure Spectroscopy. *J. Electron Spectrosc.* **2009**, *172*, 69-77.

27. Vahlberg, C.; Linares, M.; Villaume, S.; Norman, P.; Uvdal, K. Noradrenaline and a Thiol Analogue on Gold Surfaces: An Infrared Reflection-Absorption Spectroscopy, X-ray Photoelectron Spectroscopy, and Near-Edge X-ray Absorption Fine Structure Spectroscopy Study. *J. Phys. Chem. C.* **2011**, *115*, 165-175.

28. Tirsell, K. G.; Karpenko, V. P. A General-Purpose Sub-Kev X-Ray Facility at the Stanford-Synchrotron-Radiation-Laboratory. *Nucl. Instrum. Meth. A.* **1990**, *291*, 511-517.

29. Batson, P. E. Carbon-1s Near-Edge-Absorption Fine-Structure in Graphite. *Phys. Rev. B* **1993**, *48*, 2608-2610.

30. Frey, B.L.; Corn, R.M.; Weibel, S.C. In *Handbook of Vibrational Spectroscopy,* Vol. 2; Chalmers, J.M.; Griffiths, P.R., Eds.; John Wiley: United Kingdom, **2001**; pp. 1042-1056.

31. Barner, B. J.; Green, M. J.; Saez, E. I; Corn, R. M. Polarization Modulation Fourier Transform Infrared Reflectance Measurements of Thin Films and Monolayers at Metal Surfaces Utilizing Real-Time Sampling Electronic. *Anal. Chem.*, **1991**, *63*, 55-60.

32. Buffeteau, T.; Desbat, B.; Turlet, J. M., Polarization Modulation FT-IR Spectroscopy of Surfaces and Ultra-thin Films: Experimental Procedure and Quantitative Analysis. *Appl. Spectrosc.* **1991**, *45*, 380-389.

33. Bradley, M.S. A New Approach to Quantitative Spectral Conversion of PM-IRRAS: Theory, Experiments and Performance Comparisons with Conventional IRRAS. Application Note: 51368, ThermoFisher Scientific: Madison, WI, 2008.

34. Buffeteau, T.; Desbat, B.; Blaudez, D.; Turlet, J.M. Calibration Procedure to Derive IRRAS Spectra from PM-IRRAS Spectra. *Appl. Spectrosc.* **2000**, *54*, 1646-1650.

35. Paramonov, P. B.; Paniagua, S. A.; Hotchkiss, P. J.; Jones, S. C.; Armstrong, N. R.; Marder, S. R.; Bredas, J.-L. Theoretical Characterization of the Indium Tin Oxide Surface and of Its Binding Sites for Adsorption of Phosphonic Acid Monolayers. *Chem. Mater.* **2008**, *20*, 5131-5133.

36. Kresse, G.; Furthmuller, J. Efficiency of Ab-Initio Total Energy Calculations for Metals and Semiconductors Using a Plane-Wave Basis Set. *Comp. Mater. Sci.* **1996**, *6*, 15-50.

37. Kresse, G.; Furthmuller, J. Efficient Iterative Schemes for Ab Initio Total-Energy Calculations Using a Plane-Wave Basis Set. *Phys. Rev. B* **1996**, *54*, 11169-11186.

38. Perdew, J. P.; Burke, K.; Ernzerhof, M. Generalized Gradient Approximation Made Simple. *Phys. Rev. Lett.* **1996**, *77*, 3865-3868.

39. Blöchl, P. E. Projector Augmented-Wave Method. *Phys. Rev. B* **1994**, *50*, 17953-17979.

40. Blöchl, P. E.; Jepsen, O.; Andersen, O. K. Improved Tetrahedron Method For Brillioun-Zone Integrations. *Phys. Rev. B* **1994**, *49*, 16223-16233.

41. Daasch, L. W.; Smith, D. C. Infrared Spectra of Phosphorous Compounds. *Anal. Chem.* **1951**, *23*, 853-868.

42. Randon, J.; Blanc, P.; Paterson, R. Modification of Ceramic Membrane Surfaces Using Phosphoric Acid and Alkyl Phosphonic Acids and its Effects on Ultrafiltration of BSA Protein. *J. Membrane Sci.* **1995**, *98*, 119-129.

43. Persson, P.; Laiti, E.; Ohman, L. O. Vibration Spectroscopy Study of Phenylphosphonate at the Water-Aluminum (Hydr)Oxide Interface. *J. Colloid Interface Sci.* **1997**, *190*, 341-349.

44. Guerrero, G.; Mutin, P. H.; Vioux, A. Anchoring of Phosphonate and Phosphinate Coupling Molecules on Titania Particles. *Chem. Mater.* **2001**, *13*, 4367-4373.

45. Botelho do Rego, A. M.; Ferraria, A. M.; El Beghdadi, J.; Debontridder, F.; Brogueira, P.; Naaman, R.; Rei Vilar, M. Adsorption of Phenylphosphonic Acid on GaAs (100) Surfaces. *Langmuir* **2005**, *21*, 8765-8773.

46. Forner, W.; Badawi, H. M. Phenylphosphonic and Phenylthiophosphonic Acid and Their Complete Assignment. *Z. Naturforsch.* **2010**, *65b*, 357-366.

47. Forner, W.; Badawi, H. M. Study of Vibrational Spectra and Their Assignments for Phenylphosphonic Acid and Phenylthiophosphonic Acid and Comparison to Experiments. *J. Struct. Chem.* **2011**, *52*, 471-479.

48. John, A.; Philip, D.; Cabeza, A.; Devanarayanan, S. Devanarayanan, S. Vibrational Analysis of Lead(II) Phenylphosphonate Pb(O3PC6H5). *Indian J. Phys.* **2002**, *76B*, 213-215.

49. Varsanyi, G. *Vibrational Spectra of Benzene Derivatives*; Academic Press: New York, 1969.

50. Gao, W.; Dickinson, L.; Grozinger, C.; Morin, F. G.; Reven, L. Self-Assembled Monolayers of Alkylphosphonic Acids on Metal Oxides. *Langmuir* **1996**, *12*, 6429-6435.

51. Seip, C. T.; Granroth, G. E.; Meisel, M. W.; Talham, D. R. Langmuir-Blodgett Films of Known Layered Solids: Preparation and Structural Properties of Octadecylphosphonate Bilayers with Divalent Metals and Characterization of a Magnetic Langmuir-Blodgett Film. *J. Am. Chem. Soc.* **1997**, *119*, 7084-7094.

52. Fanucci, G. E.; Petruska, M. A.; Meisel, M. W.; Talham, D. R. Structural Characterization and Magnetic Order in Phenoxy-Substituted Divalent Metal Phosphonate Langmuir-Blodgett Films. *J. Solid State Chem.* **1999**, *145*, 443-451.

53. Ganbold, E.-O.; Lee, Y.; Lee, K.; Kwon, O.; Joo, S.-W. Interfacial Behavior of Benzoic Acid and Phenylphosphonic Acid on Nanocrystalline TiO2 Surfaces. *Chem. Asian J.* **2010**, *5*, 852-858.

54. Hansen, W. N. Electric Fields Produced by the Propagation of Plane Coherent Electromagnetic Radiation in a Stratified Medium. *J. Opt. Soc. Am.* **1968**, *58*, 380-388.

55. McIntyre, J. D. E.; Aspnes, D. E. Differential Reflection Spectroscopy of Very Thin Surface Films. *Surf. Sci.* **1971**, *24*, 417-434.

56. Alberti, G.; Constantino, U.; Allulli, S.; Tomassini, N. Crystalline Zr(R-PO3)2 and Zr(R-OPO3)2 Compounds (R = Organic Radical): A New Class of Materials Having Layered Structure of the Zirconium Phosphate Type. *J. Inorg. Nucl. Chem.* **1978**, *40*, 1113-1117.

57. Cao, G.; Lee, H.; Lynch, V. M.; Mallouk, T. E. Synthesis and Structural Characterization of a Homologous Series of Divalent Metal Phosphonates, M(II)(O3PR)-H2O and M(II)(HOPR)2. *Inorg. Chem.* **1988**, *27*, 2781-2785.

58. Martin, K. J.; Squattrito, P. J.; Cleafield, A. The Crystal and Molecular Structure of Zinc Phenylphonsphonate. *Inorg. Chim. Acta* **1989**, *155*, 7-9.

59. Rao, K. P.; Vidyasagar, K. Syntheses, Structure and Intercalation Properties of Low-Dimensional Phenylphosphonates, A(HO3PC6H5)(H2O3PC6H5) (A = Alkali metal, NH4, and Tl). *Eur. J. Inorg. Chem.* **2005**, *2005*, 4936-4943.

60. Allara, D. L.; Nuzzo, R. G. Spontaneously Organized Molecular Assemblies. 2. Quantitative Infrared Spectroscopic Determination of Equilibrium Structures of Solution-Adsorbed n-Alkanoic Acids on an Oxidized Aluminum Surface. *Langmuir* **1985**, *1*, 52-66.

61. Yaglioglu, B.; Huang, Y. J.; Yeom, H. Y.; Paine, D. C. A study of Amorphous and Crystalline Phases in In_2O_3-10 wt.% ZnO Thin Films Deposited by DC Magnetron Sputtering. *Thin Solid Films* **2006,** *496*, 89-94.

62. Klein, A.; Körber, C.; Wachau, A.; Säuberlich, F.; Gassenbauer, Y.; Schafranek, R.; Harvey, S.P.; Mason, T.O. Surface Potentials of Magnetron Sputtered Transparent Conducting Oxides. *Thin Solid Films*, **2009**, *518*, 1197-1203 and references contained therein.

63. Brodard-Severac, F.; Guerrero, G.; Maquet, J.; Florian, P.; Gervais, C.; Mutin, P. H. High-Field O-17 MAS NMR Investigation of Phosphonic Acid Monolayers on Titania. *Chem. Mater.* **2008,** *20*, 5191-5196.

64. Ganbold, E.-O.; Lee, Y.; Lee, K.; Kwon, O.; Joo, S.-W. Interfacial Behavior of Benzoic Acid and Phenylphosphonic Acid on Nanocrystalline TiO_2 Surfaces. *Chem. Asian J.* **2010,** *5*, 852-858.

65. Luschtinetz, R.; Frenzel, J.; Milek, T.; Seifert, G. Adsorption of Phosphonic Acid at the TiO(2) Anatase (101) and Rutile (110) Surfaces. *J. Phys. Chem. C* **2009,** *113*, 5730-5740.

66. Pawsey, S.; Yach, K.; Reven, L., Self-assembly of carboxyalkylphosphonic acids on metal oxide powders. *Langmuir* **2002,** *18*, 5205-5212.

67. Yagyu, S.; Yoshitake, M.; Tsud, N.; Chikyow, T. Adsorption Structure of Phenylphosphonic Acid on an Alumina Surface. *Appl. Surf. Sci.* **2009,** *256*, 1140-1143.

68. Donley, C.; Dunphy, D.; Paine, D.; Carter, C.; Nebesny, K.; Lee, P.; Alloway, D.; Armstrong, N. R. Characterization of Indium-Tin Oxide Interfaces Using X-ray Photoelectron Spectroscopy and Redox Processes of a Chemisorbed Probe Molecule: Effect of Surface Pretreatment Conditions. *Langmuir* **2002,** *18*, 450-457.

69. Wang, K.; Haga, M.; Hossain, M. D.; Shindo, H.; Hasebe, K.; Monjushiro, H. Effect of Subphase pH and Metal Ion on the Molecular Aggregates of Amphiphilic Ru Complexes Containing 2,2':6',2"-Terpyridine-4`-phosphonic Acid at the Air-Water Interface. *Langmuir* **2002,** *18*, 3528-3536.

70. Viinikanoja, A.; Lukkari, J.; Aaritalo, T.; Laiho, T.; Kankare, J. A Building Block for Metal Phosphonate and Polyelectrolyte Multilayers. *Langmuir* **2003,** *19*, 2768-2775.

71. Zorn, G.; Adadi, R.; Brener, R.; Yakovlev, V. A.; Gotman, I.; Gutmanas, E. Y.; Sukenik, C. N. Tailoring the Surface of NiTi Alloy Using PIRAC Nitriding Followed by Anodization and Phosphonate Monolayer Deposition. *Chem. Mater.* **2008,** *20*, 5368-5374.

72. Zhang, Y.; Cleafield, A. Synthesis, Crystal Structures, and Coordination Intercalation Behavior of Two Copper Phosphonates. *Inorg. Chem.* **1992,** *31*, 2821-2826.

73. Zima, V.; Svoboda, J.; Benes, L.; Melanova, K.; Trchova, M. New Strontium Phenylphosphonate: Synthesis and Characterization. *Solid State Sci.* **2006,** *8*, 1380-1385.

74. Svoboda, J.; Zima, V.; Benes, L.; Melanova, K.; Vlcek, M.; Trchova, M. Synthesis and Characterization of New Potential Intercalation Hosts: Barium Arylphosphonates. *J. Phys. Chem. Solids* **2008,** *69*, 1439-1443.

Chapter 3: Competing Effects of Fluorination on the Orientation of Aromatic and Aliphatic Phosphonic Acid Monolayers on Indium Tin Oxide

Adapted from: Gliboff, M.; Li, H.; Knesting, K. M.; A. K.; Giordano, A. J.; Nordlund, D.; Seidler, G. T.; Brédas, J.-L.; Marder, S. R.; Ginger, D. S. *J Phys. Chem C.* **2013**, *117*, 15139-15147

I am responsible for all NEXAFS data, analysis, AFM and quantitative treatment of surface roughness and the writing of this manuscript.

3.1 Introduction

Interfacial properties are critical in the design of efficient thin-film organic semiconductor devices. Self-assembled monolayers (SAMs) are often used to control interface properties.[1] SAMs can adjust surface energy, leading to improved adhesion/wettability of the active semiconductor layers[2] or induce changes in blend phase separation and morphology.[3, 4] Dipolar SAMs are commonly used to adjust the work function of transparent conductive substrates in order to improve injection efficiencies in organic light-emitting diodes (OLEDs),[5-7] and control charge extraction and built-in voltages in organic photovoltaics (OPVs).[1, 8-11] Phosphonic acid (PA) based SAMs, for example, have been used to modify the interface between an organic active layer and a transparent conductive oxide surface leading to improved efficiency in optoelectronic devices.[2, 12, 13]

In a simple model,[2, 14, 15] the contribution of the molecules composing the SAM with molecular dipole moment μ_{mol} , to the total work-function change, is given by:

$$\Delta\Phi = \frac{ne \cdot \mu_{mol} \cos(\theta)}{\varepsilon_0 \cdot \varepsilon} \qquad [3.1]$$

Here, e denotes the fundamental charge; ε, the dielectric constant; ε_0, the vacuum permittivity; n, the coverage density; and θ, the angle between the dipole moment and the surface normal. The variation in electrostatic potential energy across the chemical bond between the oxide surface and the SAM, known as the bond dipole, also contributes to the work function shift, as do changes to the surface geometry upon binding.[16, 17] Therefore, binding mode, orientation, and surface coverage each affect the work function of PA SAM modified oxide surfaces.[18, 19]

Fluorinated SAMs are widely used as interface modifiers in organic electronic devices[1, 5, 11, 20, 21] as fluorination is a convenient means of altering both μ_{mol} and the surface energy of the SAM. Previously, work on fluorinated thiols has shown that fluorination can lead to changes in orientation due to intermolecular interactions in a densely packed SAM.[19, 22-24] Thus, understanding the interplay between fluorination, molecular dipole moment, and molecular orientation is critical to obtaining a molecular-level understanding of the impact of PA SAMs on device performance.

Here, we use near edge x-ray absorption fine structure (NEXAFS) spectroscopy to study the effects of fluorination on the orientations of an aliphatic and an aromatic SAM. We use PA-based molecules which form robust monolayers on transparent conductive oxides. We select indium tin oxide (ITO)[2, 12, 13] as our substrate due to ITO's ubiquity in the field of thin-film optoelectronics. Octylphosphonic acid (OPA) has been used in contact modification for organic thin-film transitors[25] and similar molecules have been studied previously using NEXAFS.[26] Intermolecular forces and molecular packing details are known to play a key role in controlling the orientation of similar alkanethiol SAMs on metal substrates.[27] Therefore, by comparing OPA

\and its fluorinated counterpart, 3,3,4,4,5,5,6,6,7,7,8,8,8-tridecafluorooctylphosphonic acid (F_{13}OPA), we can examine the effect of fluorination on the intermolecular forces and molecular packing details of PA monolayers on ITO substrates. Phenylphosphonic acid (PPA), in contrast, is believed to have an orientation determined predominately by molecule-substrate interactions.[17, 28] We thus compare the orientation of PPA and its fluorinated derivative, 3,4,5-trifluorophenylphosphoic acid (F_3PPA) with the support of density functional theory (DFT) calculations to examine the effects that fluorination has on molecule-substrate interaction and binding mode.

3.2 Surfaces modified with 3,3,4,4,5,5,6,6,7,7,8,8,8-tridecafluorooctylphosphonic acid

NEXAFS excites core electrons, in our case the C K-shell electrons, to unoccupied molecular orbitals. By varying the incident angle of x-rays onto our surface and observing the changing amplitude of these transitions, we can determine the orientation of various transition dipole moments.[34, 40] Figure 3.3a shows NEXAFS TEY spectra obtained at SSRL for F_{13}OPA on ITO substrates for different incident x-ray angles, θ, from 20° to 90° (normal incidence). We assign the prominent peak at 292.8 eV to transitions from the C1s to the σ*-antibonding orbital of the C-F bonds, which is similar to the location of this feature in other molecules.[34] Other notable features include transitions from the C1s to the C-C σ*-antibonding orbitals at 290-310 eV and a C-H feature at 288.5 eV, all of which agree with previously published values for similar molecules.[26, 34, 41]

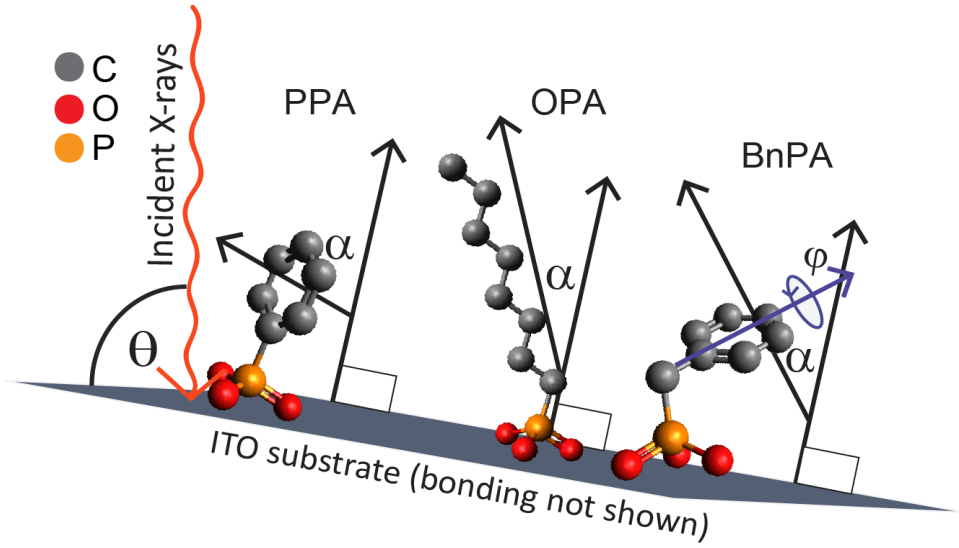

Figure 3.1. Ball and stick models of PPA, OPA and BnPA (H atoms not shown). α is defined relative to the ITO surface normal and the geometry of the molecule as shown. θ is defined as the angle the propagation direction of the incident x-ray radiation makes with the ITO substrate.

As shown in Figure 3.2 the transition dipole moments for the C-F σ* feature orient along the bond axis and span parallel planes oriented with a normal along the axis of the alkyl-chain.[34] The strong angular dependence of the C1s to C-F σ* transition in Figure 3.3a shows that the molecules adopt a preferred orientation relative to the surface. As shown in Figure 3.1, we define α as the angle between the axis of the alkyl-chain and the surface normal. We analyze the area of the peak associated with these transitions, $I_{p,}$ based on both α and the incident angle of radiation, θ, using Equation 3.2.

$$I_p(\theta) \propto \frac{1.7}{3}\left(1-0.25(3\cos^2(\theta)-1)(3\cos^2(\alpha)-1)\right)+\frac{0.15}{2}(1+\cos^2(\alpha)) \qquad [3.2]$$

In this equation, as well as Equations 3.3 and 3.4 to follow, our linear polarization is 0.85 as discussed in the experimental section and we have averaged over azimuthal orientations.

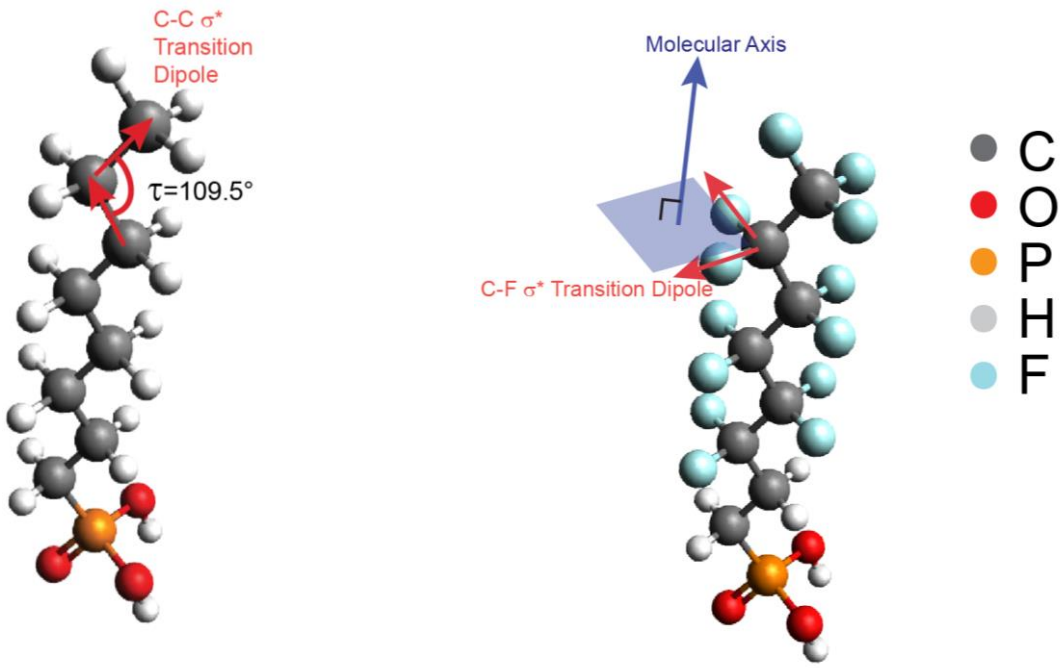

Figure 3.2. Cartoon showing transition dipole moments and molecular axis for F_{13}OPA (left) and OPA (right).

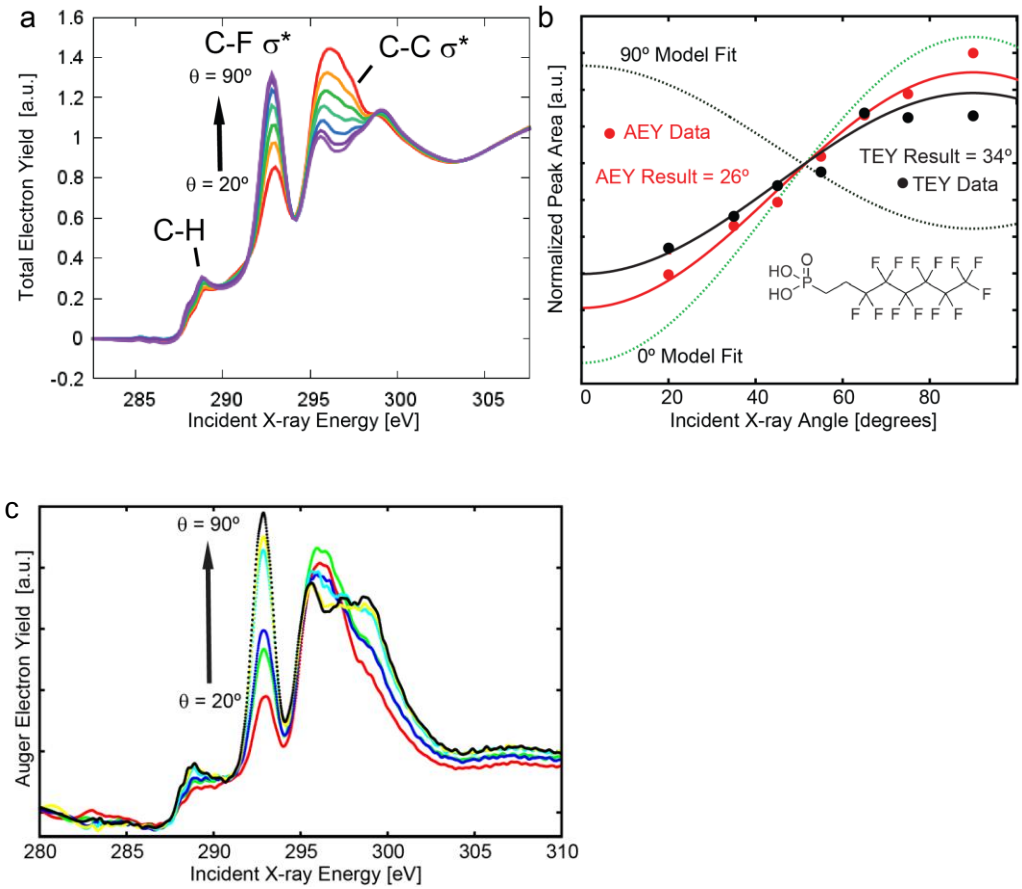

Figure 3.3. a) NEXAFS TEY spectra of F_{13}OPA on ITO at incident angles of θ = 20°, 35°, 45°, 55°, 65°, 75° and 90°. The angular dependence of the C-F σ* feature is highlighted. c) AEY spectra of F_{13}OPA on ITO at incident angles of 20°, 35°, 45°, 55°, 65°, 75° and 90°. The angular dependence of the C-F σ* feature is highlighted. b) The angular dependence of the peak area normalized by the edge step under the C-F σ* feature for both TEY (black) and AEY (red) data. Superposed are the model fits (Equation 3.2) for α = 0° (dotted green line) and 90° (dotted black line) as well as the best fit of the model to our data (solid lines).

We decompose these spectra into a sum of Gaussian peaks and an edge step. We then normalize the peak areas using the height of the C1s absorption edge jump (at 287.6 eV). Figure 3.3b shows these peak areas for various incident angles. The black solid line in Figure 3.3b is the best fit to the TEY data. The average of both AEY and TEY results yields an orientation of the axis of the alkyl-chain $\alpha = 30° \pm 5°$ from the surface normal. The strong angular dependence of the data, and the fact that our α value is far from the magic angle ($\alpha = 54.7°$) are both indicative of a well-ordered system.[34] The quoted uncertainty is dominated by the systematic uncertainty with contributions from the beam polarization (discussed in the methods section 6.4) and the background subtraction. As discussed in the methods section, we process the AEY and TEY data using different background removal techniques. We take the discrepancy between the orientations provided by the AEY and TEY data as a measure of the systematic uncertainty associated with the background removal. This systematic uncertainty should not be interpreted as the range of angles which is accessible to the molecule on the ITO surface. Some molecule-molecule variation occurs due in part to surface roughness, gauche defects in the alkyl-chain, or binding mode changes. Our result and uncertainty correspond to a representative value of this distribution, specifically the expected

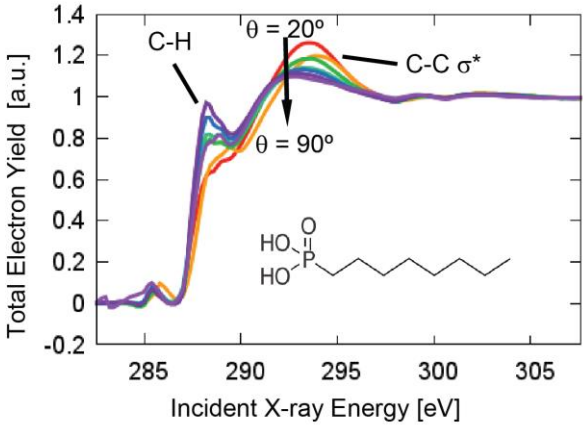

Figure 3.4. NEXAFS TEY spectra of OPA on ITO at incident angles of 20°, 35°, 45°, 55°, 65°, 75° and 90°, the angular dependence of the C-C σ* feature is highlighted.

value of $\cos^2(\alpha)$ (Equation 3.2). We note that our ITO surfaces are relatively smooth as determined by atomic force microscopy (AFM) (RMS roughness ~ 0.7 nm) and are below the threshold where roughness effects have been shown to emerge in studies of alkane PAs on ITO.[26]

Figure 3.4 shows NEXAFS TEY spectra for the non-fluorinated OPA on ITO substrates for values of θ from 20° to 90°. We observe strong angular dependence in the transitions to the C-C σ*, which is broad and occupies a region from 290 to 298 eV. Other notable features include a C-H feature appearing between 288.4-289 eV. The C1s absorption edge appears at 287.4 eV. Again, all assignments are in good agreement with their expected positions.[26, 34, 41] The transition dipole moment for the C1s to σ* anti-bonding orbital of the C-C bonds are directed along the bond axis. Figure 3.2 demonstrates the orientation of the transition dipole moments. The strong angular dependence of the C1s to C-C σ* shows that the molecules adopt a preferred orientation relative to the surface. The angle that the alkyl-chain makes with the surface normal, α, is determined quantitatively by analyzing the NEXAFS peak areas in a similar way as performed for F_{13}OPA above. The normalized peak areas, I_{tc} (θ), are modeled using Equation 3.3. This tilted-chain model has an additional parameter, τ, which is the angle between subsequent C-C bonds on the alkyl-chain and is taken to be 109.5°.[26, 40] Fitting the normalized peak areas to this model yields an orientation of the axis of the alkyl-chain $\alpha = 41° \pm 8°$ from the surface normal. This value is similar to that measured previously for this molecule[26] and other aliphatic SAMs on ITO.[41]

$$I_{tc}(\theta) \propto \frac{0.85}{3}\left((1-3\cos^2(\theta))\cos(2\alpha)\cos(2\tau)+\cos^2(\theta)+1\right) - \frac{0.15}{2}(\cos(2\alpha)\cos(2\tau)-1) \quad [3.3]$$

Significantly, the tilt angles calculated from data in Figures 3.3 and 3.4 demonstrate that the OPA molecule is lying flatter (larger α), and F_{13}OPA is standing up more vertically (smaller α). The fact that the observed orientation of OPA is closer to the magic angle could also be indicative of increased disorder in the OPA films as compared to F_{13}OPA. However, the measured orientations of OPA and F_{13}OPA are both similar to those observed for alkane thiols on noble metals.[22, 42, 43] Importantly, we note that the relative change in tilt angle between OPA and F_{13}OPA on ITO is very similar to that which has previously been reported for alkanethiol and fluorinated alkanethiol SAMs on gold, despite the significant differences in binding chemistry and surface mobility between thiols and phosphonic acids.[19, 23]

Given the similarity in changes in average tilt angles we observe upon fluorination of our aliphatic PA, OPA, and that reported in the literature for fluorination of aliphatic thiols, we suggest that similar fluorine-induced changes in chain packing can be inferred to explain our data. In this context, we rationalize the more upright orientation of F_{13}OPA in our NEXAFS experiments due to two closely-related factors, both of which are based on changes in intermolecular interactions and molecular packing details. First, the increase in steric radius (5.6 Å for a fluorinated chain versus 4.8 Å for the non-fluorinated chain) should lead to a more upright orientation of fluorinated alkane thiols due to space-filling arguments.[19, 22, 23] Previous measurements[2, 17, 44] suggest that surface coverage densities of alkyl-PAs on ITO are similar

(~1 × 10^{14} molecules/cm^2) to those of alkanethiols on gold, making a similar space-filling argument reasonable for our PA system. Second, using structural rigidity measurements, an increased resistance to gauche defects in fluorinated alkanethiols has been reported as compared to their non-fluorinated counterparts.[22] Both the increase in steric radius of the fluorinated chains, and a decrease in density of gauche defects would be consistent with the orientation of the fluorinated molecule being farther from the magic angle and more upright than its non-fluorinated counterpart, as we observe experimentally.

We note that our fluorinated SAM (F_{13}OPA) is substantially, but not fully, fluorinated. Nevertheless, our data are consistent with expectations based on the behavior of fully and partially fluorinated alkanethiols. Colorado et al. showed that for $CF_3(CF_2)_n(CH_2)_x$ alkanethiols, values of $n \geq 6$ gave identical wettability and surface energy.[45] Previous work[46] has suggested that as x increases, for a constant n, the van der Waals packing of the unfluorinated part of the alkyl chain will dominate, while below a certain x value, the fluorinated contributions will dominate. Our well-ordered SAMs suggest that F_{13}OPA is in the regime where the packing of the fluorinated chains is dominant, and as such we would predict a similar orientation to a fully fluorinated chain.

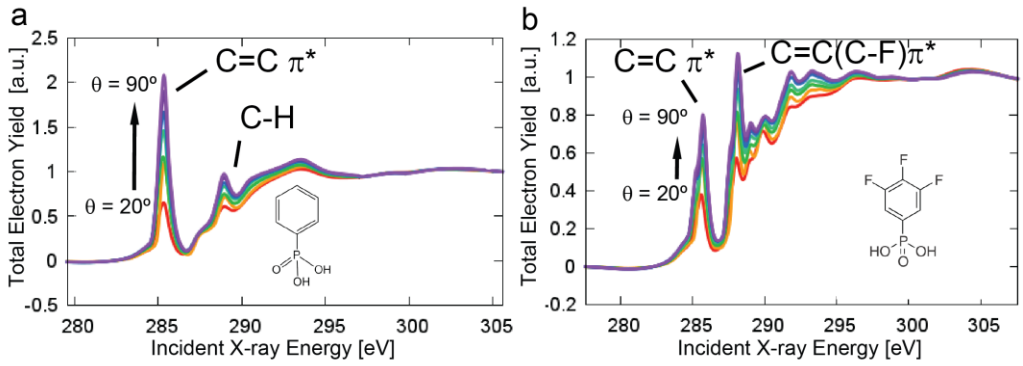

Figure 3.5. NEXAFS TEY spectra of a)PPA and b) F_3PPA on ITO at incident angles of 20°, 35°, 45°, 55°, 65°, 75° and 90°, the angular dependence of the C=C π * feature is highlighted.

3.3 Surfaces modified with phenylphosphonic acid derivatives

Small aromatic PA SAMs are important interface modifiers in optoelectronics, since their small size enables easy tunneling of charges across the layer.[47] In principle, aromatic molecules have stronger intermolecular interactions than aliphatic molecules. However, intermolecular interactions in SAMs composed of a single aromatic ring have been shown to be less important in determining orientation than molecule-substrate interactions.[28, 48] Therefore, we examine aromatic SAMs to address the impact of SAM fluorination on binding geometry.

Figure 3.5a shows NEXAFS TEY spectra for the non-fluorinated PPA on ITO substrates for values of θ from 20° to 90°. We observe strong angular dependence in the transitions to the C=C π*, located at 285.5 eV. Other notable features include a C-H feature at 288.8 eV and C-C σ* features at 290-300 eV. The C1s absorption edge appears at 287.3 eV. Each feature is in good

agreement with expected locations.[28, 34] The strong angular dependence of the C=C π* transition demonstrates a preferred, upright orientation on ITO, in good agreement with our previous study of PPA on indium zinc oxide.[28] Figure 3.5b shows TEY spectra for the F_3PPA molecule for values of θ from 20° to 90°. These spectra exhibit features similar to those for PPA with additional features due to the different chemical environments of carbon atoms in the ring. The fluorinated carbon give rise to a distinctly shifted C=C π* feature at 288.3eV, with a similar weight as the non-fluorinated aromatic carbon, where the shift in energy is mainly ascribed to the difference in ionization potential for carbon bonded to F.[40, 49, 50]

Other additional structures (in the C-C σ* region, e.g.) can also be seen due to the distinct chemical environments. There is strong angular dependence in the C=C π* features (H-bonded and F-bonded π*), though not as strong as in the non-fluorinated molecule.

The transition dipole moment for the C1s to π* anti-bonding orbital of the C=C ring is directed normal to the plane of the phenyl ring. As shown in Figure 3.1, α is the angle between the normal to the phenyl ring plane and the surface normal. The α value is determined quantitatively by analyzing the NEXAFS peak in a similar way as performed above with the OPA derivatives. The normalized area under the π* features, I_v (θ), are modeled using Equation 3.4.[34] Fitting the normalized peak areas to this model yields an orientation of the phenyl ring normal, α = 71° ± 4° from the surface normal for PPA and 63° ± 4° for F_3PPA.

$$I_v(\theta) \propto \frac{0.85}{3}\left(1 + 0.5(3\cos^2(\theta) - 1)(3\cos^2(\alpha) - 1)\right) + \frac{0.15}{2}(1 - \cos^2(\alpha)) \quad [3.4]$$

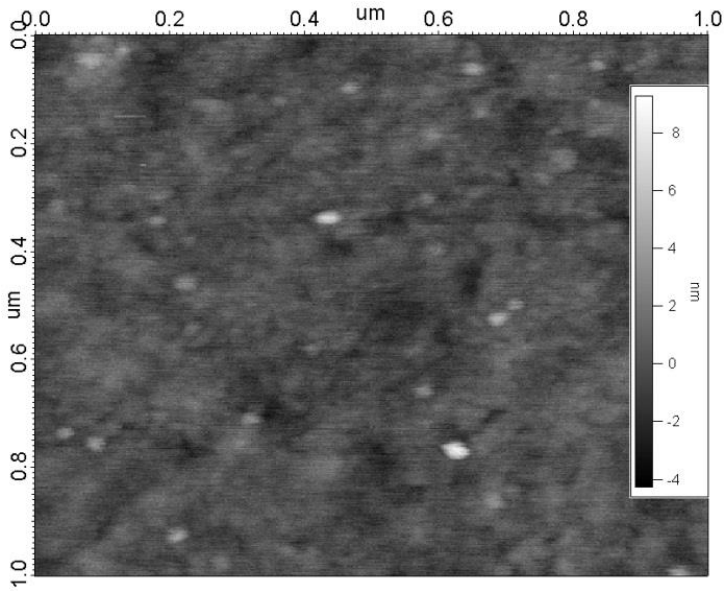

Figure 3.6. Contact mode atomic force microscopy scan of bare ITO. The RMS surface roughness for our ITO is between 0.7-0.8 nm over 100 nm.

We have previously reported a similar orientation of PPA on amorphous indium zinc oxide: 77± 5°.[28] We believe that the small apparent difference in orientation between the value of 71° ± 4° measured here and our previous result is due to the substrates used in the two experiments. Specifically, we attribute the smaller alpha measured on ITO to the larger distribution of local surface normals created by increased surface roughness of ITO relative to that of the ultrasmooth indium zinc oxide substrates used in the previous study (<0.3 nm RMS roughness). Our ITO substrates have a surface roughness of 0.7-0.8 nm RMS over 100 nm, as measured with AFM (Figure 3.6). Consistent with previously patterned SAM work,[5] we were unable to resolve differences in surface roughness before and after SAM deposition. We expect NEXAFS-derived orientations to represent a convolution of the molecular orientation relative to the local surface

normal with the distribution of orientations of the local surface normals relative to a global or average surface normal. When molecules have a wide distribution of orientations, the NEXAFS result is the expected value of $\cos^2(\alpha)$ of this distribution (Equation 3.4). We can model this convolution using Equation 3.5:

$$\cos^2(\alpha_{measured}) = \int_0^{2\pi}\int_0^{C} [\cos(\alpha_{rc})\cos(\arctan(s)) - \cos(\gamma)\sin(\alpha_{rc})\sin(\arctan(s))]^2 f(s) ds \frac{d\gamma}{2\pi} \quad \textbf{[3.5a]}$$

$$s = \frac{\Delta height}{PixelSize} \quad \textbf{[3.5b]} \qquad \eta = \langle s^2 \rangle \quad \textbf{[3.5c]} \qquad f(s) = \frac{1}{N(C)} \exp(-s^2/\eta^2) \quad \textbf{[3.5d]}$$

Equation 3.5a is an expectation value of cosine squared, expanded using the sum/difference formula. $\alpha_{measured}$ is the NEXAFS result and α_{rc} is the corrected value, which corresponds to the orientation that the molecules adopt relative to a local surface normal. The local slope, *s*, is defined to be the change in height of the ITO surface, as measured by AFM, from one pixel to another, divided by the pixel size equal to 1/512 μm (Equation 3.5b); γ is a dummy variable which accounts for the azimuthal relationship between the planes subtended by 1) the molecule axis and local surface normal and 2) the local and global surface normals. A value $C = 1 >> \eta$ was used as the upper bound of the integral in Equation 3.5a. f(*s*) is the distribution of local slopes (Equation 3.5d) and is approximated as Gaussian with variance η and no azimuthal dependence (Equation 3.5c). Naturally the normalization, *N*, is dependent on *C,* the chosen upper bound.

The value of *s* is used to estimate the angle between the local surface normal and the global surface normal at that pixel. η is calculated using Equation 3.5b from the distribution of measured values of *s*. A rougher surface should have a larger value for η. The integral in

Equation 3.5a was done numerically in quadrature to produce a one-to-one function relating each value of $\alpha_{measured}$ to a value of α_{rc} (Figure 3.7). Applying this model to the range of values that fall within our uncertainty yields α_{rc} = ~69-79° for PPA, which agrees with the previous result on IZO, and 60-69° for F_3PPA. The limitations of this model are that it ignores any internal degrees of freedom in the molecule, which are not significant in PPA and F_3PPA. Further, we assume that intermolecular interactions are weaker than surface interactions. This assumption is supported by the results of the DFT calculations presented below. Because of this latter limitation, we chose not to apply this model to the OPA SAMs based on the reported importance of intermolecular interactions in that system and previous work indicating invariance of orientation with respect to small changes in surface roughness.[26, 51]

We observe a less upright orientation of F_3PPA relative to PPA. We cannot explain this trend using the same reasoning as in the OPA derivatives. Unlike the aliphatic SAMs, which can have gauche defects, PPA and F_3PPA do not have internal degrees of freedom which can affect the orientation. Furthermore, the molecular packing forces that appear to play a role in the more upright orientation of the fluorinated OPA molecules do not seem to have a similar effect on these aromatic SAMs. Thus, in order to examine possible changes in binding geometry, we turn to computation to compare our measured orientations with the results of DFT calculations.

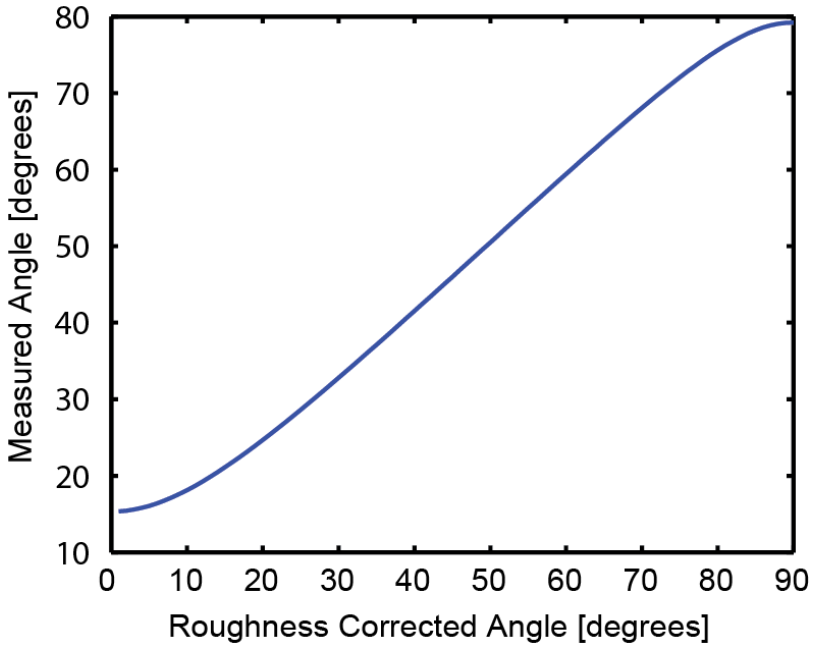

Figure 3.7. Numerical solution of Equation 3.5, based on the AFM image given in Figure 3.6

3.4 Comparison of PPA deposition methods

Table 1 shows NEXAFS data taken for PPA deposited using various soaking methods and Micro-contact printing onto both ITO and IZO substrates. All data reported in chapter 2 utilize the 168 hour soak, while data in this chapter utilize the 48 hour room temperature soak. Additional details are provided in the methodology section 6.2. No significant difference is observed between the different deposition methods used here. In each case, the difference between the ITO and IZO orientations can be accounted for using the surface roughness correction discussed previously.

Table 3.1. NEXAFS calculated molecular tilt angles (in degrees) for PPA deposited using various methods onto ITO and IZO. Includes IZO values with roughness correction applied.

Deposition Method	ITO	IZO	IZO (RC)
48 Hour (RT)	71+/-4	75+/-5	74+/-6
48 Hour (70°C)	70+/-3	71+/-6	73+/-5
168 hour Soak	72+/-4	77+/-5	74+/-5
Microcontact-printed	72+/-3		

3.5 Calculated orientations of PPA and F_3PPA

We have previously reported DFT calculations for PPA on ITO.[28] As the calculation assumes a smooth surface, these results should be compared to the α_{rc} values. The tridentate configuration, with all three oxygen atoms in the PO_3 moiety covalently bonded to metals, exhibits a calculated orientation of 78-79°. The bidentate configuration, defined as two oxygen atoms in the PO_3 moiety covalently bonded to metals and the remaining oxygen hydrogen bonded to surface hydroxyls, exhibits an orientation of 68-75°. Our experimental result falls in between these values, which would be consistent with a mixture of both binding modes. The monodentate binding mode for PA SAMs on ITO has previously been ruled out on the basis of DFT geometry optimizations and the agreement between the DFT values of O 1s binding energy shifts and the XPS measurements.[35] The calculations gave similar results for both low (2.8×10^{13} molecules/cm^2) and high (1.1×10^{14} molecules/cm^2) packing densities, suggesting that, at least in

theory, intermolecular interactions are not dominating the tilt angles at those densities, consistent with previous work.[28]

Table 3.2 shows the calculated orientation, binding geometry, and dipole moment of the SAM projected to the surface normal direction for F_3PPA. Binding sites 1-4 correspond to the available binding positions for PA SAMs in our ITO surface model.[28] We observe no significant difference between the calculated tilt angles of PPA and F_3PPA for a specific binding mode. At low packing density, 2.8×10^{13} molecules/cm^2, the tridentate binding geometry (site 2) shows a larger tilt angle (78°) than the bidentate binding geometry (68°-76°). At higher packing density, 1.1×10^{14} molecules/cm^2, we observe the same trend, with a larger range of orientations available in the tridentate binding mode (73°-81°). Our measured orientation for F_3PPA agrees with the DFT-calculated orientation for a predominantly bidentate bonding mode, regardless of packing density.

Based on these observations, we proposed that F_3PPA is more likely to exhibit bidentate binding geometries on ITO than PPA. This indicates a reduced likelihood of a PA molecule forming a third O-metal bond to the substrate. Currently, the preferential formation of hydrogen bonds with surface hydroxyls instead of covalent bonds has only been explained using coverage of surface hydroxyls before PA binding.[13] Previous studies suggest that two of the P-O-metal bonds are formed by hetero-condensation with surface hydroxyls, driven by the electrophilicity of the phosphor atom.[13] Previous studies of PA SAMs using surface-sensitive IR spectroscopy[28] or calorimetry[52] were not able to determine binding mode definitively.

Table 3.2. Binding geometries of PPA and F_3PPA computed at various packing density. The values for $\mu_{SAM,z}$ for F_3PPA are reproduced from Ref. 17.

PPA Packing density	sites	tilt angle	$\mu_{SAM,z}$ (D/unit cell)[17]	P-O bond length (Å)			O-In(Sn) bond length (Å)		
2.8×10^{13} molecules/cm^2	(1)	78°	0.24	1.57	1.54	1.55	2.13	2.16	2.33
	(2)	79°	0.71	1.58	1.53	1.56	2.21	2.31	2.25
	(3)	75°	0.36	1.55	1.59	1.56	2.25	2.21	--
	(4)	68°	0.02	1.56	1.59	1.53	2.31	2.24	--
1.1×10^{14} molecules/cm^2	(1)	72°	2.57	1.57	1.54	1.55	2.14	2.15	2.28
	(2)	81°		1.57	1.53	1.57	2.20	2.31	2.26
	(3)	71°		1.55	1.59	1.55	2.27	2.19	--
	(4)	70°		1.55	1.59	1.54	2.29	2.25	--
F_3PPA Packing density	Sites	tilt angle	$\mu_{SAM,z}$ (D/unit cell)[17]	P-O bond length (Å)			O-In(Sn) bond length (Å)		
2.8×10^{13} molecules/cm^2	(1)	69°	3.56	1.58	1.55	1.56	2.17	2.27	--
	(2)	78°	3.04	1.58	1.53	1.55	2.20	2.32	2.24
	(3)	76°	3.37	1.55	1.58	1.55	2.22	2.26	--
	(4)	68°	3.53	1.55	1.58	1.52	2.32	2.26	--
1.1×10^{14} molecules/cm^2	(1)	73°	9.47	1.57	1.54	1.54	2.15	2.16	2.29
	(2)	81°		1.58	1.53	1.55	2.20	2.32	2.24
	(3)	71°		1.55	1.59	1.55	2.27	2.19	--
	(4)	70°		1.55	1.59	1.54	2.29	2.25	--

Based on these observations, we propose that F_3PPA is more likely to exhibit bidentate binding geometries on ITO than PPA. This indicates a reduced likelihood of a PA molecule forming a third O-metal bond to the substrate. The preferential formation of hydrogen bonds with surface hydroxyls instead of covalent bonds has primarily been explained in the context of relative coverage of surface hydroxyls before PA binding.[13] Previous studies suggest that two of

the P-O-metal bonds are formed by hetero-condensation with surface hydroxyls, driven by the electrophilicity of the phosphorous atom.[13]

We consider two straightforward explanations for the increased likelihood of bidentate bonding of the fluorinated molecule: the first of which is intermolecular electrostatic interactions, and the second of which is Lewis base character. Based on the upright orientation of the molecules, we do not consider van der Waals interactions between the fluorine atoms and the ITO surface. Previous calculations of F_3PPA SAM orientations have shown no significant changes in binding geometry over a range of surface coverages.[17] We observe the effect of intermolecular dipole-dipole interactions as depolarization within the SAM, which can be seen in the calculation of the perpendicular dipole moment, $\mu_{SAM,z}$ at high packing density which is 9.47 D (Table 1). Without depolarization, this number should be four times the $\mu_{SAM,z}$ value of 3.04-3.56 D for low packing density. Despite the presence of these intermolecular electrostatic interactions, we do not observe significantly different calculated orientations as we vary the packing density of the SAM, and thus consider the electrostatic effects unlikely to result in changes in binding mode.

This leaves us to speculate on a change in Lewis basicity as a possible explanation for the increased tilt angle of the F_3PPA. The inductive effect of ring fluorination should reduce the Lewis base character of the lone oxygen and decrease its likelihood to act as an electron donor to a surface metal atom, thus increasing the propensity of the PA for bidentate binding. Our measurements of both the first and second pK_a values for PPA and F_3PPA (see Methodology section 6.12) do show a decrease in acidity (~0.8 change in pK_a) for F_3PPA relative to PPA. While this trend is qualitatively consistent with a reduction in electron density on the oxygen

atoms of F_3PPA, it is not yet clear if the effect is large enough to account for a change in orbital occupation sufficient to favor bidentate binding over tridentate binding. Nevertheless, such a change would be consistent with the increased tendency for a less upright orientation of F_3PPA that we observe in our experiments.

3.6 Surfaces modified with BnPA derivatioves

Figure 1.3 shows various benzyl-phosphonic acid (Bn PA) derivatives that have been used to modify ITO work functions. To determine the orientation of the BnPA molecules, we use the transition from the C1s to the C=C π^* orbital, which occurs at an incident photon energy of about 285 eV. The addition of R-groups to the benzyl ring induced some shifts or broadening of this feature in some cases. For example, in F_5BnPA, the (C-F)C=C π^* occurs at 288 eV. The orientation of the transition dipole moment for this excitation is perpendicular to the bond axis and therefore normal to the benzene ring.[40] For these molecules, we define α as the angle between this transition dipole moment and the surface normal similar to the PPA derivatives. The amplitude of these transitions is described in Equation 3.4. The angle-dependent spectra are given in appendix B.

In NEXAFS, if molecules are oriented randomly, this corresponds to and orientation of 54.7°, the magic angle. At the magic angle of orientation, we see no dependence on the angle of incident radiation.[40] Using the expectation of cosine squared, as in Equation 3.5, we consider a two-population distribution of orientations, with one population at the roughness-corrected DFT value, α', and the other population at the magic angle (Equation. 3.6). The disorder fraction, δ, can be used to quantify the deviation of the measured value, α, from the theory result.

Table 3.3. Results for angle α of our phosphonic-acid SAMs with various functional groups. DFT calculated values are provided for a packing density of 2.8×10^{13} molecules/cm^2**.** Disorder values quantify the deviation of measured and theory values when both are on the same side of the magic angle.

Molecule	α	DFT α	Disorder
BnPA	47 ± 3°	41	16 - 62%
2-FBnPA	52 ± 2°	46	39 - 88%
3-FBnPA	60 ± 2°	52	*
p-FBnPA	59 ± 2°	51	*
2,3-F_2BnPA	61 ± 3°	46	*
3,4-F_2BnPA	60 ± 2°	52	*
m-F_2BnPA	58 ± 3°	51	*
m,p-F_3BnPA	58 ± 5°	51	> 55%
F_5BnPA	60+/-5°	48	*
o-F_2BnPA	53 ± 4°	50	0 - 100%*
2-CF_3BnPA	59 ± 2°	44	*
3-CF_3BnPA	62 ± 3°	51	*
o-$(CF_3)_2$BnPA	50 ± 5°	33	> 50%
p-CF_3BnPA	53 ± 5°	51	0 - 100%*
p-NO_2BnPA	60 ± 3°		
p-CNBnPA	52 ± 3°		

* Disorder model breaks down, see discussion section.

$$\cos^2(\alpha) = (1-\delta)\cos^2(\alpha') + \delta\cos^2(55°) \quad [3.6]$$

The range of disorder values for each calculated value is given in Table 3.3. A value of 0 in this range indicates that the calculated values are in good agreement with the measured result.

The orientations of BnPA derivatives show a large divergence from theory values in some cases. Orientations of these molecules might be complicated by an additional degree of freedom, φ, which is the rotation of the benzyl ring about the C1-C4 axis, hereafter referred to as twist angle (Figure 3.1). Vibrations along this degree of freedom lead to greater disorder than PPA derivatives. This disorder leads to measured orientations in between the theory value and the magic angle, as observed in BnPA, 2-FBnPA and o-$(CF_3)_2$BnPA.

Due to a measured and calculated orientation near the magic angle, we cannot distinguish whether o-F_2BnPA and p-CF_3BnPA adopt orientations very similar to theory results, or if those molecules are largely disordered. Most BnPA derivatives deviate from theory values in ways that cannot be explained by disorder alone, specifically those with measured orientations farther from (F_5BnPA) or on the other side of (3-FBnPA; p-FBnPA; 2,3-F_2BnPA; 3,4-F_2BnPA; m-F_2BnPA, m,p-F_3BnPA; 2-CF_3BnPA; 3-CF_3BnPA) the magic angle as compared to the calculated values. Future studies include detailed XPS, PM-IRRAS and UPS measurements to determine if these unexplained deviations from theory values are due to differences in binding mode or intermolecular forces.

3.7 Summary and conclusions

We have measured the orientation of an aliphatic SAM, OPA and its fluorinated derivative F_{13}OPA on the transparent conductive oxide ITO. Our measured orientation of OPA is similar to previous observations of similar SAMs. Each of our molecules has a well-defined orientation far from the magic angle, indicating well-ordered SAMs. We find that fluorination of the OPA molecule leads to a more upright orientation, due to steric intramolecular and intermolecular

forces, as anticipated from similar trends that have been observed in the literature for alkanethiols on Au.

In contrast however, the aromatic SAM PPA was found to be more upright than its fluorinated counterpart, F_3PPA. The orientations of PPA and F_3PPA were found to be similar to those calculated using DFT at various surface coverages. This agreement suggests that intermolecular interactions are less critical to determining the orientation of these SAMs than molecule-substrate interactions. Surprisingly, we observe well-oriented SAMs, even though the surface roughness is of the same order as the molecule size. We find changes in orientation with fluorination that we suggest may be due to changes in binding geometry. Our data are consistent with reduced tridentate and increased bidentate binding for the fluorinated aromatic SAM, as might be explained by a reduction in Lewis basicity of the lone oxygen. The effect of fluorine position on aromatic SAMs is largely unexplored. Future studies may explore the effect of fluorination position in aromatic phosphonic acids to better understand the interplay between intermolecular and head-group binding effects.

We conclude that the orientation of SAMs does not vary in a simple way with fluorination; multiple competing effects are likely present. Fluorination of a SAM will change the magnitude of the molecular dipole, but might also provoke changes in binding mode and molecular packing details. These changes can affect both the orientation of the molecule and the bond dipole, leading to a deviation in the expected work function shift. Consideration of the changes in orientation and binding mode brought on by fluorination of SAMs can inform surface modifier design rules and, ultimately, improve device performance through better engineering of interfaces.

3.8 References

1. Ma, H.; Yip, H.-L.; Huang, F.; Jen, A. K. Y., Interface Engineering for Organic Electronics. *Adv. Funct. Mater.* **2010,** *20*, 1371-1388.

2. Paniagua, S. A.; Hotchkiss, P. J.; Jones, S. C.; Marder, S. R.; Mudalige, A.; Marrikar, F. S.; Pemberton, J. E.; Armstrong, N. R., Phosphonic Acid Modification of Indium-Tin Oxide Electrodes: Combined XPS/UPS/Contact Angle Studies. *J. Phys. Chem. C* **2008,** *112*, 7809-7817.

3. Park, L. Y.; Munro, A. M.; Ginger, D. S., Controlling Film Morphology in Conjugated Polymer: Fullerene Blends with Surface Patterning. *J. Amer. Chem. Soc.* **2008,** *130*, 15916-15926.

4. DeLongchamp, D. M.; Kline, R. J.; Fischer, D. A.; Richter, L. J.; Toney, M. F., Molecular Characterization of Organic Electronic Films. *Adv. Mater.* **2011,** *23*, 319-337.

5. Knesting, K. M.; Hotchkiss, P. J.; MacLeod, B. A.; Marder, S. R.; Ginger, D. S., Spatially Modulating Interfacial Properties of Transparent Conductive Oxides: Patterning Work Function with Phosphonic Acid Self-Assembled Monolayers. *Adv. Mater.* **2012,** *24*, 642-646.

6. Sharma, A.; Haldi, A.; Hotchkiss, P. J.; Marder, S. R.; Kippelen, B., Effect of Phosphonic Acid Surface Modifiers on the Work Function of Indium Tin Oxide and on the Charge Injection Barrier into Organic Single-Layer Diodes. *J. Appl. Phys.* **2009,** *105*, 074511-074516.

7. Wang, M.; Hill, I. G., Fluorinated Alkyl Phosphonic Acid SAMs Replace PEDOT:PSS in Polymer Semiconductor Devices. *Org. Electron.* **2012,** *13*, 498-505.

8. Kouki, F.; Karsi, N.; Lang, P.; Horowitz, G.; Bouchriha, H., Effect of Self Assembled Monolayers on Charge Carrier Photogeneration in Sexithiophene Based Diodes. *Synthetic Met.* **2012,** *162*, 1741-1745.

9. Beaumont, N.; Hancox, I.; Sullivan, P.; Hatton, R. A.; Jones, T. S., Increased Efficiency in Small Molecule Organic Photovoltaic Cells through Electrode Modification with Self-Assembled Monolayers. *Energy Environ. Sci.* **2011,** *4*, 1708-1711.

10. Bulliard, X.; Ihn, S. G.; Yun, S.; Kim, Y.; Choi, D.; Choi, J. Y.; Kim, M.; Sim, M.; Park, J. H.; Choi, W. et al., Enhanced Performance in Polymer Solar Cells by Surface Energy Control. *Adv. Func. Mater.* **2010,** *20*, 4381-4387.

11. MacLeod, B. A.; Horwitz, N. E.; Ratcliff, E. L.; Jenkins, J. L.; Armstrong, N. R.; Giordano, A. J.; Hotchkiss, P. J.; Marder, S. R.; Campbell, C. T.; Ginger, D. S., Built-In Potential in Conjugated Polymer Diodes with Changing Anode Work Function: Interfacial States and Deviation from the Schottky–Mott Limit. *J. Phys. Chem. Lett.* **2012,** *3*, 1202-1207.

12. Cecchet, F.; Lis, D.; Guthmuller, J.; Champagne, B.; Fonder, G.; Mekhalif, Z.; Caudano, Y.; Mani, A. A.; Thiry, P. A.; Peremans, A., Theoretical Calculations and Experimental Measurements of the Vibrational Response of p-NTP SAMs: An Orientational Analysis. *J. Phys. Chem. C* **2010,** *114*, 4106-4113.

13. Hotchkiss, P. J.; Jones, S. C.; Paniagua, S. A.; Sharma, A.; Kippelen, B.; Armstrong, N. R.; Marder, S. R., The Modification of Indium Tin Oxide with Phosphonic Acids: Mechanism of Binding, Tuning of Surface Properties, and Potential for Use in Organic Electronic Applications. *Accounts Chem. Res.* **2012,** *45*, 337-346.

14. Heimel, G.; Romaner, L.; Zojer, E.; Bredas, J.-L., The Interface Energetics of Self-Assembled Monolayers on Metals. *Accounts Chem. Res.* **2008,** *41*, 721-729.

15. Kronik, L.; Shapira, Y., Surface Photovoltage Phenomena: Theory, Experiment, and Applications. *Surface Science Reports* **1999,** *37*, 1-206.

16. Crispin, X.; Geskin, V.; Crispin, A.; Cornil, J.; Lazzaroni, R.; Salaneck, W. R.; Bredas, J.-L., Characterization of the Interface Dipole at Organic/ Metal Interfaces. *J. Am. Chem. Soc.* **2002,** *124*, 8131-8141.

17. Li, H.; Paramonov, P.; Bredas, J. L., Theoretical Study of the Surface Modification of Indium Tin Oxide with Trifluorophenyl Phosphonic Acid Molecules: Impact of Coverage Density and Binding Geometry. *J. Mater. Chem.* **2010,** *20*, 2630-2637.

18. Romaner, L.; Heimel, G.; Zojer, E., Electronic Structure of Thiol-Bonded Self-Assembled Monolayers: Impact of Coverage. *Phys. Rev. B.* **2008,** *77*.

19. Alloway, D. M.; Hofmann, M.; Smith, D. L.; Gruhn, N. E.; Graham, A. L.; Colorado, R.; Wysocki, V. H.; Lee, T. R.; Lee, P. A.; Armstrong, N. R., Interface Dipoles Arising from Self-Assembled Monolayers on Gold: UV-Photoemission Studies of Slkanethiols and Partially Fluorinated Alkanethiols. *J. Phys. Chem. B.* **2003,** *107*, 11690-11699.

20. Wu, K.-Y.; Yu, S.-Y.; Tao, Y.-T., Continuous Modulation of Electrode Work Function with Mixed Self-Assembled Monolayers and Its Effect in Charge Injection. *Langmuir* **2009,** *25*, 6232-6238.

21. Marmont, P.; Battaglini, N.; Lang, P.; Horowitz, G.; Hwang, J.; Kahn, A.; Amato, C.; Calas, P., Improving Charge Injection in Organic Thin-Film Transistors with Thiol-Based Self-Assembled Monolayers. *Org. Electron.* **2008,** *9*, 419-424.

22. Alves, C. A.; Porter, M. D., Atomic-Force Microscopic Characterization of a Fluorinated Alkanethiolate Monolayer at Gold and Correlations to Electrochemical and Infrared Reflection Spectroscopic Structural Descriptions. *Langmuir* **1993,** *9*, 3507-3512.

23. Kim, H. I.; Koini, T.; Lee, T. R.; Perry, S. S., Systematic Studies of the Frictional Properties of Fluorinated Monolayers with Atomic Force Microscopy: Comparison of CF3- and CH3-Terminated Films. *Langmuir* **1997,** *13*, 7192–7196.

24. Vericat, C.; Vela, M. E.; Benitez, G.; Carro, P.; Salvarezza, R. C., Self-Assembled Monolayers of Thiols and Dithiols on Gold: New Challenges for a Well-Known System. *Chem. Soc. Rev.* **2010,** *39*, 1805-1834.

25. Acton, O.; Dubey, M.; Weidner, T.; O'Malley, K. M.; Kim, T.-W.; Ting, G. G.; Hutchins, D.; Baio, J. E.; Lovejoy, T. C.; Gage, A. H. et al., Simultaneous Modification of Bottom-Contact Electrode and Dielectric Surfaces for Organic Thin-Film Transistors Through Single-Component Spin-Cast Monolayers. *Adv. Funct. Mater.* **2011,** *21*, 1476-1488.

26. Losego, M. D.; Guske, J. T.; Efremenko, A.; Maria, J. P.; Franzen, S., Characterizing the Molecular Order of Phosphonic Acid Self-Assembled Monolayers on Indium Tin Oxide Surfaces. *Langmuir* **2011,** *27*, 11883-11888.

27. Laibinis, P. E.; Whitesides, G. M.; Allara, D. L.; Tao, Y. T.; Parikh, A. N.; Nuzzo, R. G., Comparison of the Structures and Wetting Properties of Self-Assembled Monolayers of Normal-Alkanethiols on the Coinage Metal-Surfaces, Cu, Ag, Au. *J. Amer. Chem. Soc.* **1991,** *113*, 7152-7167.

28. Gliboff, M.; Sang, L.; Knesting, K. M.; Schalnat, M. C.; Mudalige, A.; Ratcliff, E. L.; Li, H.; Sigdel, A. K.; Giordano, A. J.; Berry, J. J. et al., Orientation of Phenylphosphonic Acid Self-Assembled Monolayers on a Transparent Conductive Oxide: A Combined NEXAFS, PM-IRRAS, and DFT Study. *Langmuir* **2013,** *29*, 2166-2174.

29. Bravo-Altamirano, K.; Montchamp, J.-L., A Novel Approach to Phosphonic Acids from Hypophosphorous Acid. *Tetrahedron Lett.* **2007,** *48*, 5755-5759.

30. Schulmeyer, T.; Paniagua, S. A.; Veneman, P. A.; Jones, S. C.; Hotchkiss, P. J.; Mudalige, A.; Pemberton, J. E.; Marder, S. R.; Armstrong, N. R., Modification of BaTiO3 Thin Films: Adjustment of the Effective Surface Work Function. *J. Mater. Chem.* **2007,** *17*, 4563-4570.

31. Hotchkiss, P. J.; Li, H.; Paramonov, P. B.; Paniagua, S. A.; Jones, S. C.; Armstrong, N. R.; Bredas, J. L.; Marder, S. R., Modification of the Surface Properties of Indium Tin Oxide with Benzylphosphonic Acids: A Joint Experimental and Theoretical Study. *Adv.Mater.* **2009,** *21*, 4496-4501.

32. Tirsell, K. G.; Karpenko, V. P., A General-Purpose Sub-Kev X-Ray Facility at the Stanford-Synchrotron-Radiation-Laboratory. *Nucl. Instrum. Meth. A* **1990,** *291*, 511-517.

33. Batson, P. E., Carbon-1s near-Edge-Absorption Fine-Structure in Graphite. *Phys. Rev. B* **1993,** *48*, 2608-2610.

34. Stöhr, J., *NEXAFS Spectroscopy*. Springer-Verlag: Berlin, 1992; p xv, 403 p.

35. Paramonov, P. B.; Paniagua, S. A.; Hotchkiss, P. J.; Jones, S. C.; Armstrong, N. R.; Marder, S. R.; Bredas, J. L., Theoretical Characterization of the Indium Tin Oxide Surface and of

Its Binding Sites for Adsorption of Phosphonic Acid Monolayers. *Chem. Mater.* **2008,** *20,* 5131-5133.

36. Kresse, G.; Furthmuller, J., Efficiency of Ab-Initio Total Energy Calculations for Metals and Semiconductors Using a Plane-Wave Basis Set. *Computational Materials Science* **1996,** *6,* 15-50.

37. Kresse, G.; Furthmuller, J., Efficient Iterative Schemes for Ab Initio Total-Energy Calculations Using a Plane-Wave Basis Set. *Phys. Rev. B.* **1996,** *54,* 11169-11186.

38. Blöchl, P. E., Projector Augmented Wave Method. *Phys. Rev. B.* **1994,** *50,* 17953-17979.

39. Perdew, J. P.; Burke, K.; Ernzerhof, M., Generalized Gradient Approximation Made Simple. *Phys. Rev. Lett.* **1996,** *77,* 3865-3868.

40. Stöhr, J.; Outka, D. A., Determination of Molecular Orientations on Surfaces from the Angular-Dependence of near-Edge X-Ray-Absorption Fine-Structure Spectra. *Phys. Rev. B* **1987,** *36,* 7891-7905.

41. Yan, C.; Zharnikov, M.; Golzhauser, A.; Grunze, M., Preparation and Characterization of Self-Assembled Monolayers on Indium Tin Oxide. *Langmuir* **2000,** *16,* 6208-6215.

42. Ulman, A., Formation and Structure of Self-Assembled Monolayers. *Chem. Rev.* **1996,** *96,* 1533-1554.

43. Porter, M. D.; Bright, T. B.; Allara, D. L.; Chidsey, C. E. D., Spontaneously Organized Molecular Assemblies. 4. Structural Characterization of Normal-Alkyl Thiol Monolayers of Gold by Optical Ellipsometry, Infrared-Spectroscopy and Electrochemistry. *J. Amer. Chem. Soc.* **1987,** *109,* 3559-3568.

44. Koh, S. E.; McDonald, K. D.; Holt, D. H.; Dulcey, C. S.; Chaney, J. A.; Pehrsson, P. E., Phenylphosphonic Acid Functionalization of Indium Tin Oxide: Surface Chemistry and Work Functions. *Langmuir* **2006,** *22,* 6249-6255.

45. Colorado, R.; Lee, T. R., Wettabilities of Self-Assembled Monolayers on Gold Generated from Progressively Fluorinated Alkanethiols. *Langmuir* **2003**, *19,* 3288-3296.

46. Tamada, K.; Ishida, T.; Knoll, W.; Fukushima, H.; Colorado, R.; Graupe, M.; Shmakova, O. E.; Lee, T. R., Molecular Packing of Semifluorinated Alkanethiol Self-Assembled Monolayers on Gold: Influence of Alkyl Spacer Length. *Langmuir* **2001**, *17,* 1913-1921.

47. Holmlin, R. E.; Haag, R.; Chabinyc, M. L.; Ismagilov, R. F.; Cohen, A. E.; Terfort, A.; Rampi, M. A.; Whitesides, G. M., Electron Transport Through Thin Organic Films in Metal-Insulator-Metal Junctions Based on Self-Assembled Monolayers. *J. Amer. Chem. Soc.* **2001,** *123,* 5075-5085.

48. Frey, S.; Stadler, V.; Heister, K.; Eck, W.; Zharnikov, M.; Grunze, M.; Zeysing, B.; Terfort, A., Structure of Thioaromatic Self-Assembled Monolayers on Gold and Silver. *Langmuir* **2001,** *17*, 2408-2415.

49. Davis, D. W.; Shirley, D. A.; Thomas, D. T., X-Ray Photoelectron Spectroscopy of Fluorinated Benzenes. *J. Amer. Chem. Soc.* **1972,** *94*, 6565-6575.

50. Hitchcock, A. P.; Fischer, P.; Cedanken, A.; Robin, M. B., Antibonding σ* Valence MOs in the Inner-Shell and Outer-Shell Spectra of the Fluorobenzenes. *J. Phys. Chem.* **1987,** *91***,** 531-540.

51. Chockalingam, M.; Darwish, N.; Le Saux, G.; Gooding, J. J., Importance of the Indium Tin Oxide Substrate on the Quality of Self-Assembled Monolayers Formed from Organophosphonic Acids. *Langmuir* **2011,** *27*, 2545-2552.

52. Hotchkiss, P. J., The Design, Synthesis, and Use of Phosphonic Acids for the Surface Modification of Metal Oxides. Ph.D. Thesis, Georgia Institute of Technology. Atlanta, GA. 2008.

Chapter 4: Direct measurement of Acceptor Group Localization on Donor Acceptor Polymers using Resonant Auger Spectroscopy

Adapted from an in progress manuscript with contributions from: Matthew Gliboff, Dana Sulas, Dennis Nordlund, Dane W. de Quilettes, Phu Nguyen, Xiaosong Li, David S. Ginger

I am responsible for all NEXAFS and resonant Auger data and analysis, and the writing of this manuscript.

4.1 Introduction

Conjugated polymers are the critical components of modern organic optoelectronics, forming the active layer of thin-film transistors, organic light-emitting diodes and organic solar cells.[1-4] Organic electronics are light-weight, flexible and potentially cheaper to mass-produce than their inorganic counterparts.[5] Production of more efficient devices depends on understanding the mechanisms of dynamic processes including exciton formation, free-charge generation, recombination, and charge transport both through the conjugated polymer itself and to electrodes or electron acceptors.[6, 7] For instance, the degree of excited state delocalization and its relationship to the prevalence of free charges versus excitons as the primary product of photoexcitation is still under discussion.[8-11] Recently, donor-acceptor co-polymers have gained popularity as a molecular design strategy for facilitating planar polymer backbones with higher pi-electron delocalization and lower band gaps.[12] Evaluating the excited state electronic structure in these materials may provide insight into their varying device performance.

In principle, angle-resolved photoemission can provide information on the spatial extent of occupied states, such as the HOMO.[13-15] The addition of pump-probe and femtosecond time-resolution provides the capability to examine delocalization of excited states, predominately at interfaces, but becomes experimentally complex.[16, 17] Resonant Auger spectroscopy provides a

synchrotron-based alternative to time-resolved optical spectroscopies for studying excited state electronic structure. Few previous studies have applied this technique to polymer films.[18, 19]

In resonant Auger spectroscopy, we record photoemission spectra while tuning the incoming photon energy across an atomic absorption edge and the associated resonances. Resonant Auger is an extension of near-edge x-ray absorption fine structure (NEXAFS) and possesses the same chemical and site specificity.[20, 21] Resonant Auger spectroscopy is an excitation-decay technique. Provided that the involved core orbitals have significant spatial overlap with the LUMO, the lowest energy resonance in the NEXAFS corresponds to an optical bandgap excitation, although a core hole remains rather than a valence hole. Resonant Auger spectroscopy can be used to probe the electronic structure of this excitation, without the complexities of pump-probe techniques.

Figure 4.1 shows the decay paths that appear in the photoemission spectrum for resonant and non-resonant excitations. The spectator feature appears for a resonant excitation and is shifted to higher emitted electron kinetic energy relative to the non-resonant Auger pathway (spectator shift). This shift is due to the screening of the core hole by the excited electron and therefore provides a qualitative measure of the overlap of the excited state wavefunction with the 1s orbital of the photoexcited atom. If excited electrons can delocalize away from the core hole in times comparable to that of core-hole decay, then the resonant spectra will also have a contribution identical to non-resonant Auger emission.[22] The branching ratio of the resonant and non-resonant auger channels can be used to calculate the time scales of charge transfer processes using the core-hole clock method.[21, 23-25]

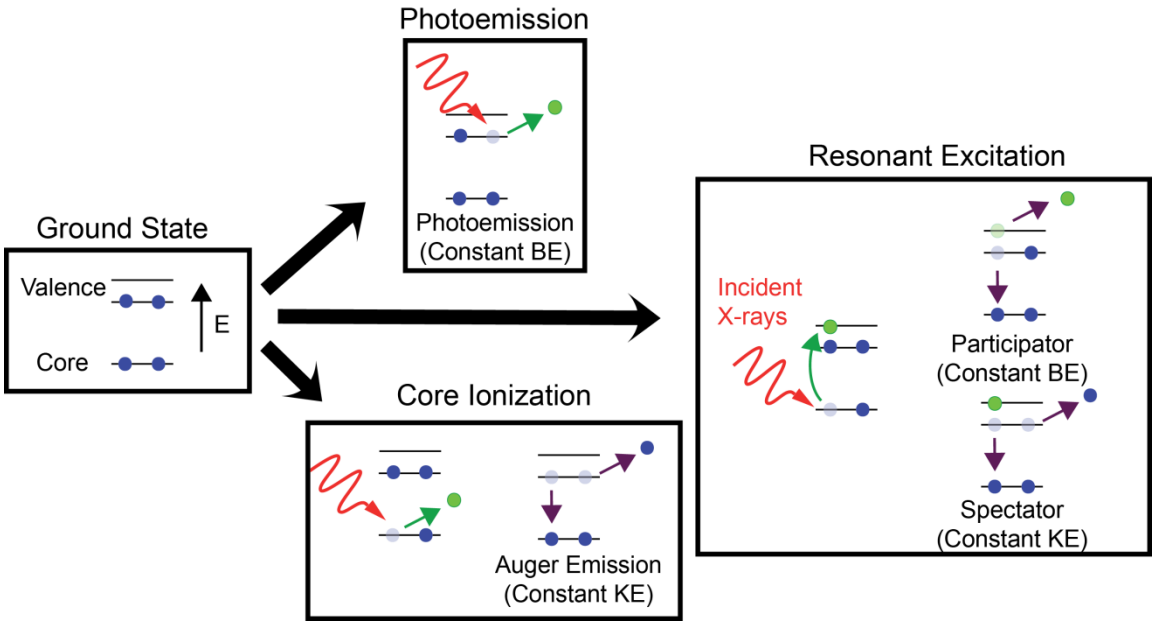

Figure 4.1. Decay pathways for different types of x-ray excitations. Some pathways emit electrons at constant kinetic energy (KE), while others have constant binding energy (BE). Green represents the photoexcited electron and purple arrows represent Auger processes. (Reprint of Figure 1.8)

In order to explore the possible impact of LUMO structure on IQE and free charge generation, we examined two conjugated polymers: poly[2,1,3-benzothiadiazole-4,7-diyl[4,4-bis(2-ethylhexyl)-4H-cyclopenta[2,1-b:3,4-b']dithiophene-2,6-diyl]] (PCPDTBT) and poly[[9-(1-octylnonyl)-9H-carbazole-2,7-diyl]-2,5-thiophenediyl-2,1,3-benzothiadiazole-4,7-diyl-2,5-thiophenediyl] (PCDTBT). Both polymers have alternating electron-donating (dithiophene or carbazole for PCPDBT and PCDTBT, respectively) and electron-accepting (benzothiadiazole) units along the polymer backbone, and are known to make efficient organic photovoltaic devices.[26, 27] The IQE for PCDTBT devices is nearly 100%,[27] which is 30 percentage points higher than PCPDTBT devices.[28]

We use time-dependent density functional theory (TD-DFT) to calculate the N 1s x-ray absorption spectra of these polymers and compare to N k-edge NEXAFS data. We examine the calculated electronic structure of the first x-ray resonance as a sum of density functional theory (DFT) calculated virtual orbitals. We find similar electronic structure of the excited state in both PCPDTBT and PCDTBT. We perform resonant Auger spectroscopy and measure spectator shifts of the first x-ray resonance for both polymers, providing qualitative experimental confirmation of the calculated results.

4.2 Quantum chemical calculations

We use DFT and TD-DFT to optimize the polymer structure and understand the electron density distribution in PCPDTBT and PCDTBT excited states. Figures 4.2 and 4.3 show the core and unoccupied molecular orbitals (MOs) involved in the first excitation of the N1s NEXAFS spectra for PCPDTBT and PCDTBT, respectively. Each red line represents the oscillator strength for a transition of an electron in the nitrogen 1s orbital on a benzothiadiazole unit of the monomer to a virtual orbital. X-ray absorption spectra (blue solid lines) are simulated through the convolution of the vertical transition energies and oscillator strengths with Gaussian functions characterized by a full width at half maximum (FWHM) of 0.2 eV. These calculated spectra are compared to the actual NEXAFS N K-edge spectra (black lines). We observe a characteristic red-shift in the simulated spectra due to limitations based within Hartree-Fock/DFT theory and the B3LYP functionals.[29]

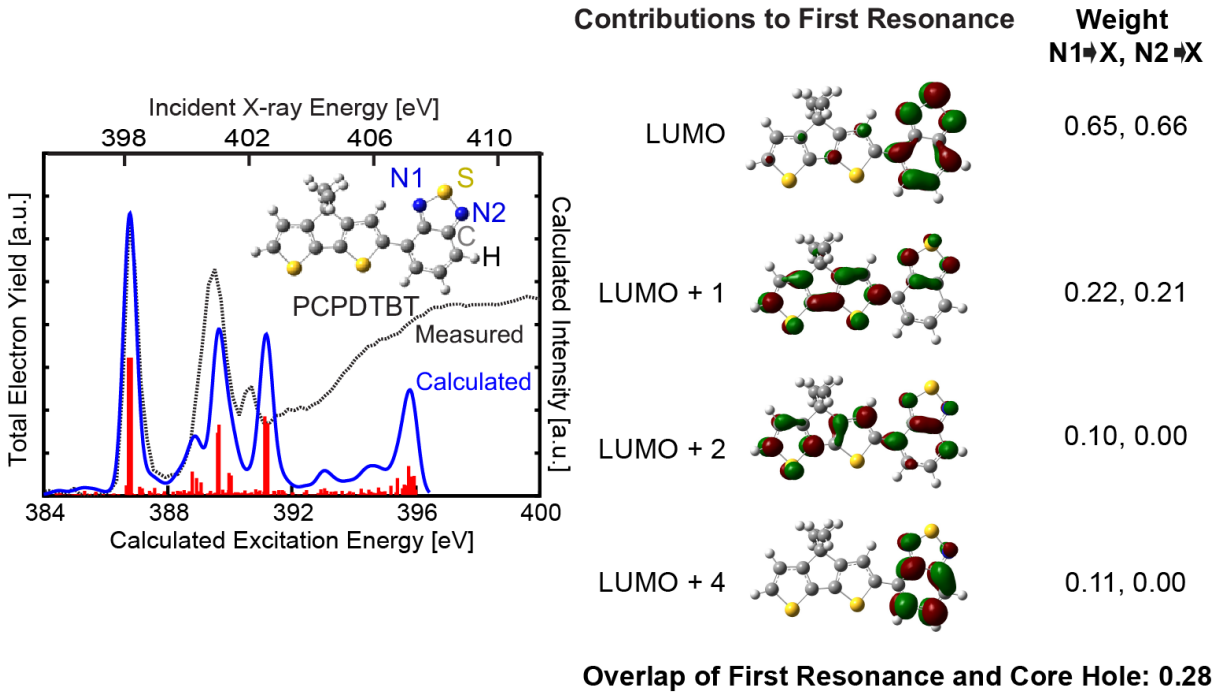

Figure 4.2. Left: TD-DFT calculated N 1S x-ray absorption spectrum of the PCPDTBT monomer. The red lines correspond to transitions to unoccupied MOs. The blue curve is the Gaussian broadening of these transitions using a FWHM of 0.2 eV. The black dashed line shows the measured NEXAFS spectrum for comparison. The DFT-optimized geometry is inset. Right: The first x-ray absorption peak is broken down into contributing virtual orbitals. The molecular orbital diagrams and the relative weights of transitions from each N atom 1s orbital to each virtual orbital are given. The overlap between the weighted sum of the virtual orbitals and their core hole is found to be 0.28 electrons.

For both polymers, we observe that the first resonance in the x-ray spectrum corresponds to a linear combination of virtual MOs. The relative weights are given in Figures 4.2 and 4.3 for transitions from the 1s orbitals of each N atom on the benzothiadiazole group. Transitions to the virtual LUMO orbital are dominant in both polymers. In the case of PCDTBT, the oscillator

strength for transitions from the carbazole N atom 1s orbital was smaller than those for the benzothiadiazole group N atoms by a factor of 1000 or more. Based on this, we assume that the carbazole N atom is most likely not involved in the first peak of the N k-edge NEXAFS spectrum. A population analysis reveals the probability of finding an excited electron on the nitrogen atom involved in the excitation, which effectively describes the overlap of the first resonance with the core hole. This value is similar for PCPDTBT (0.28) and PCDTBT (0.24) and provides a qualitative prediction for the spectator shifts measured in resonant Auger spectroscopy.

We have focused on monomer results above, as the resonant Auger data, shown below, proves to be independent of conjugation length and other morphological changes. TD-DFT calculations were also performed for the dimer of each molecule and are discussed below. The overlap of the first resonance with the core hole for the dimer is found to be 0.27 for PCPDTBT and 0.17 for PCDTBT. Both of these values are within 0.05 of the monomer values and these differences are not considered significant.

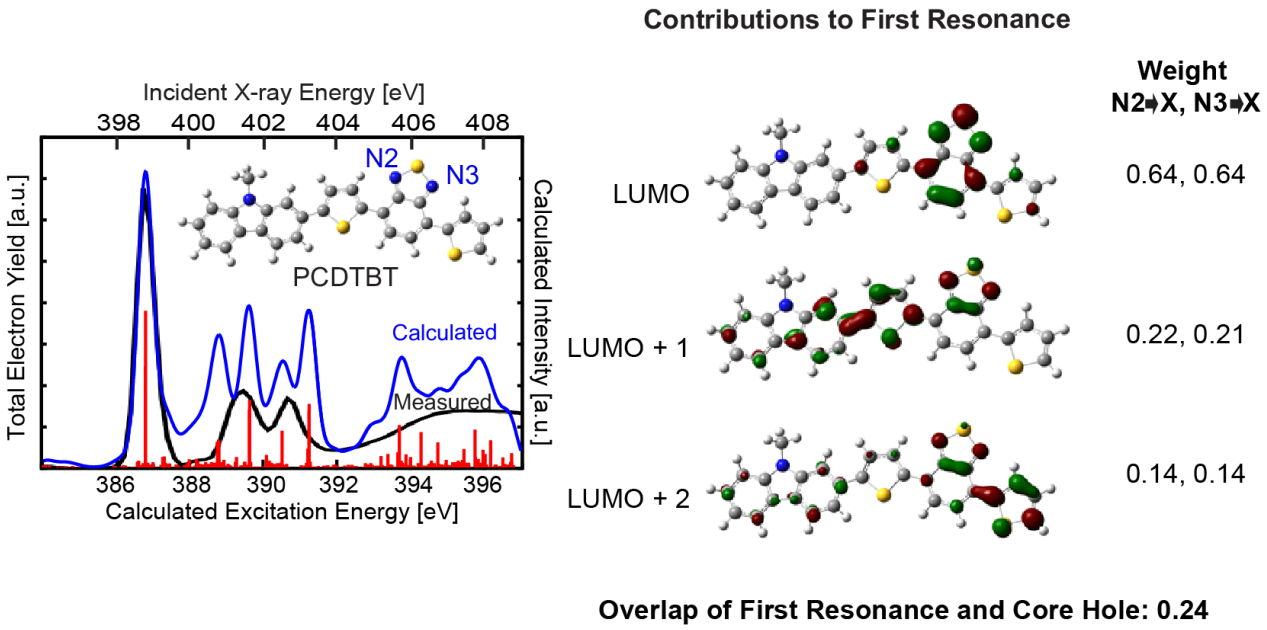

Figure 4.3. Left: TD-DFT calculated N 1S x-ray absorption spectrum of the PCDTBT monomer. The red lines correspond to transitions to unoccupied MOs. The blue curve is the Gaussian broadening of these transitions using a FWHM of 0.2 eV. The black dashed line shows the measured NEXAFS spectrum for comparison. The DFT-optimized geometry is inset. Right: The first x-ray absorption peak is broken down into contributing virtual orbitals. The molecular orbital diagrams and the relative weights of transitions from each N atom 1s orbital to each virtual orbital are given. The overlap between the weighted sum of the virtual orbitals and their core hole is found to be 0.24 electrons.

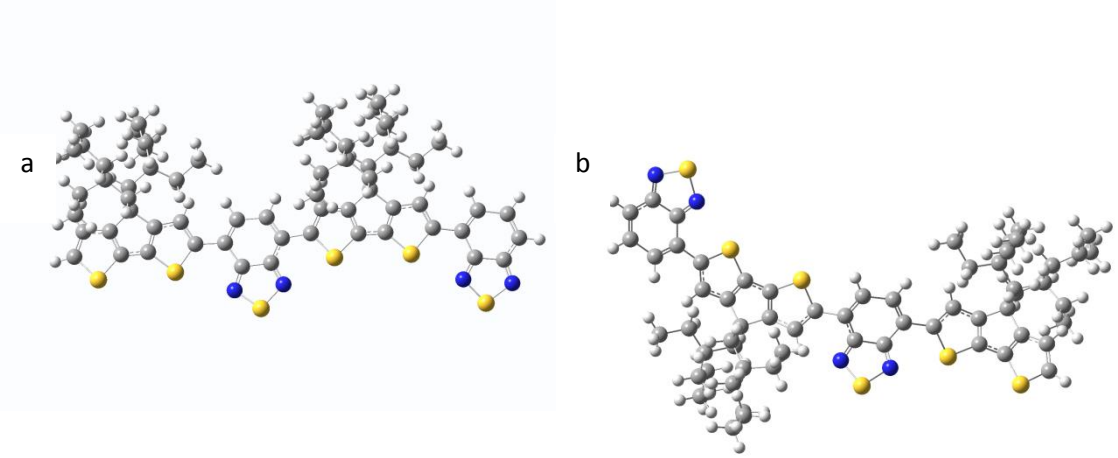

Figure 4.4. a) Optimized geometry of the gas phase PCPDTBT dimer with syn thiadiazole and thiophene units (3147580.66 kcal/mol) b) Optimized geometry of the gas phase PCPDTBT dimer with anti thiadiazole and thiophene units (3147511.64 kcal/mol) shows a 69 kcal/mol stabilization.

4.3 Dimer geometry

For PCPDTBT, PCDTBT, and similar polymers, it has previously been reported that the monomer conformation with the thiadiazole ring anti to the thiophene units is preferred by ~1 kcal/mol.[30, 31] However, it is also commonly observed that the steric strain induced by large alkyl groups causes monomer units to be anti to each other along the polymer chain.[32] In fact, we observe a 69 kcal/mol stabilization for the PCPDTBT dimer when the alkyl chains extend to opposite sides of the molecule, despite syn thiadiazole and thiophene units (Figure 4.4). While holding this geometry for longer polymer chains, our calculations approximate the alkyl chains with methyl groups to reduce computational cost.

4.4 Auger final state screening effects

From the N1s overlap values we can estimate the change in Auger parameter due to the spectating electron based on the final state effects model proposed by Cole et al.[33, 34] The Auger parameter, ξ, is defined as the kinetic energy of the Auger feature as compared to a photoemission feature. A shift in the Auger parameter indicates a shift in the Auger kinetic energy that is independent of work-function changes or sample charging effects. A spectator shift is a change in the kinetic energy of the Auger feature due to a change in valence occupancy, and is a special case of Δξ:

$$\Delta\xi = \Delta\{qb + \delta q_N[a - 2b + d(q - \delta q_N)]\} \quad (4.1)$$

δq_N is the change in valence occupancy due to the core hole. Physically, it must be between 0 and 1, with higher values assigned to better conductors or highly polarizable chemical environments. For purposes of this estimate, we assume this parameter is much smaller than *q*, the change in valence charge due to excited state overlap. By convention *a*, *b* and *d* are atomic structure parameters which are discussed elsewhere[34, 35] and have been calculated for nitrogen in the literature as 39.93 eV, -6.76 eV, and 5.05eV respectively.[36] Loosely, the parameter *a* is related to the size of the valence shell in the ground state, *b* represents the contraction of the valence shell on core ionization and the parameter *d* corresponds to the expansion or contraction of the valence shell with gain or loss of valence charge. Based on our orbital overlap for the monomer and dimer cases and Equation 4.1, we can estimate a spectator shift of 1.8-1.9 eV for PCPDTBT and a shift of 1.2-1.6 eV for PCDTBT. The excited state of PCDTBT is perhaps marginally more delocalized than that of PCPDTBT, but this difference is likely too small to be significant.

4.5 Resonant Auger spectroscopy of PCPDTBT

Figure 4.5b shows the N k-edge NEXAFS of PCPDTBT blended with $PC_{71}BM$. The first resonance at 398.5 eV corresponds to a transition of N 1s electrons to the LUMO, which strongly overlaps the benzothiadiazole unit and is composed of the virtual orbitals shown in Figure 4.2.[37] Additional resonances occur below the onset of the N 1s absorption edge at 400.5 and 401.8 eV, likely corresponding to transitions to other unoccupied π^* orbitals.[38] Figure 4.5c shows the valence photoemission spectrum, taken at incident x-ray energy below the onset of N 1s NEXAFS features (395 eV) with binding energy calibrated using the second-order excitation of the N 1s electrons (binding energy = 409.9 eV).[39] We observe two distinct valence bands, labeled G and H, centered at binding energies of 18 eV and 7.5 eV respectively. These spectra are similar to those reported for a model molecule, MTBT, which contains a benzothiadiazole group and a thiophene group.[38]

Figure 4.5d shows the spectra of electrons emitted at incident x-ray energies marked 1-7 on Figure 4.5b. Spectrum 1 is composed of the valence photoemission features (G,H) and the second order excitation of N 1s electrons, labeled SN. Spectrum 8 is the non-resonant KLL Auger spectrum for the nitrogen atoms, taken at ionizing incident x-ray energy (440 eV). The spectrum shown has been smoothed using a Loess method with a 10eV window. The Auger spectrum is very broad and exhibits a primary peak at about 379.5 eV with a dip at 370.2 eV and a secondary peak centered near 360 eV.

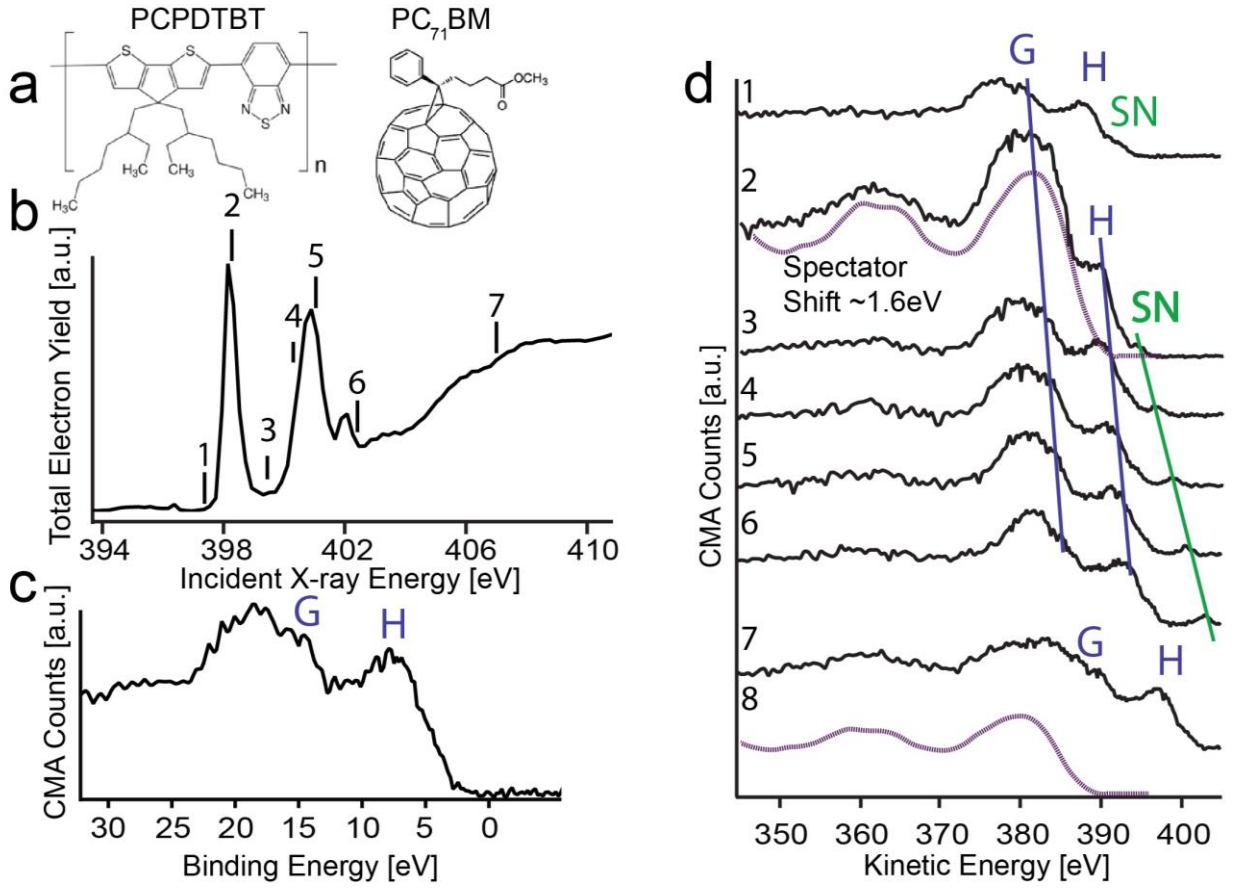

Figure 4.5. a) Molecular structure of PCPDTBT and $PC_{71}BM$ b) NEXAFS N K-edge total electron yield spectrum of a PCPDTBT and $PC_{71}BM$ blend film taken at 20° incident angle. c) Photoemission spectrum of the same film taken at incident x-ray energy of 395 eV. d) Resonant photoemission spectra of the blend film. Spectra labeled 1-7 correspond to incident x-ray energies as labeled on (a). The spectrum labeled 8 corresponds to a pure Auger spectrum taken at incident x-ray energy of 440 eV. The light purple line on spectrum 2 represents the spectator contribution of the fit used to determine the spectator shift. Peaks labeled G and H are valence photoemission peaks. Peak SN is second order light from the monochromator exciting N 1s electrons.

Spectra 2-7 are dominated by a broad Auger feature similar in shape to spectrum 8, but at slightly higher kinetic energy. The kinetic energy of this feature is constant as the monochromator is detuned across the LUMO resonance, indicating that our combined monochromator and electron-analyzer bandwidth is too large to achieve the Auger-resonant Raman condition or access vibrational state information.[21, 40] As the peaks and dip in this feature are shifted to a slightly higher kinetic energy than the non-resonant Auger spectrum, we attribute this intensity to spectator resonant decay channels. We also observe valence band photoemission features (G and H) with Raman-like dispersion in spectra 2-7. These features, especially the H feature in spectrum 2 at 391 eV, are somewhat enhanced due to participator channels as discussed below.

In order to establish the spectator shift for the LUMO excitation, we fit spectrum 2 using a combination of a scaled and shifted non-resonant Auger spectrum (spectrum 8) and the valence photoemission features. The former contribution is shown overlaying spectrum 2 in Figure 4.5d. The spectator shift is given by the energy shift of the Auger spectrum in the fit is 1.6 eV. The Auger dip alignment method[41] gives a similar result of 1.4 eV. Spectrum 5 is difficult to fit due to the overlap of Auger and photoemission structure. Spectrum 7 was found to have a spectator shift of less than 1 eV, indicating dominance of the non-resonant Auger pathway. The Auger intensity was not high enough in the other spectra to perform the fit reliably. The result for the spectator shift of the LUMO excitation (1.6 eV) matches the values from the DFT calculations and final state model (1.8-1.9 eV) quite well.

During this fitting process, we cannot explain the intensity in the neighborhood of 390 eV for excitation to the LUMO without considering significant participator enhancement of

photoemission feature H. In the participator decay path, the photoexcited electron participates in the Auger process. The participator decay is energetically degenerate with photoemission features and has a Raman-like dispersion.[22] The presence of the participator feature indicates spatial overlap between the wavefunctions of the excited state, the degenerate valence state and the core hole. In this case, the participator feature provides a qualitative indication of a significant overlap between the HOMO and LUMO.

We note that there is no evidence for non-resonant-like Auger emission at the LUMO excitation, meaning that we cannot specify a branching ratio or utilize the core-hole clock method. Applications of the core-hole clock method to organic systems are well-studied, especially for charge transfer across organic-organic and organic-metal interfaces.[22, 42-47] Applications of resonant Auger to thick (100 nm) polymer films are less common.[19, 38] Charge transfer processes can occur both from one conformational subunit to another along the same polymer chain, called a through-bond mechanism. Through space delocalization and charge transfer across the pi-stacking distance also play a role in closely-packed, well ordered polymer films.[48-50] The core-hole clock method assumes discrete charge transfer on the femtosecond timescale to a final state which has little to no overlap with the initial state. In a most core-hole clock experiments the use of a large metallic substrate satisfies this condition. In a polymer film, by contrast, the delocalized state might have significant overlap with the initial state, rendering the core-hole clock methodology inapplicable.

4.6 Effects of film morphology

Conjugation length, H-aggregation, pi-stacking and other morphological properties play a role in excited state localization and the timescales of any charge transfer processes.[18, 19, 46, 51] To

examine the effect of morphology on our results, we compared the photoemission of PCPDTBT in a blend with $PC_{71}BM$ with and without the diiodooctane (DIO) solvent additive. The use of DIO increases polymer crystallinity by selectively solvating the fullerene phase, resulting in a relative enhancement of the 0-0 Franck-Condon peak in the absorption spectrum (Figure 4.6).[52, 53] We observe no difference in the resonant Auger spectrum with the change in absorption spectrum (Figure 4.7), indicating that the delocalization being probed is mostly insensitive to exciton bandwidth or conjugation length. This is an indication that the nature of the excited state is dominated by the electronic structure of the monomer and its interactions with neighboring monomers.

Apart from minor changes to the non-resonant valence photoemission, identical spectra were found for neat-films of PCPDTBT in the absence of a fullerene (Figure 4.7), indicating that we are not probing processes of charge transfer to the fullerene. We also note that our experiment does not measure exciton or polaron formation, since the electron is excited from a core shell and geometric reorganization of the polymer does not occur on a time scale similar to the core hole decay.[48]

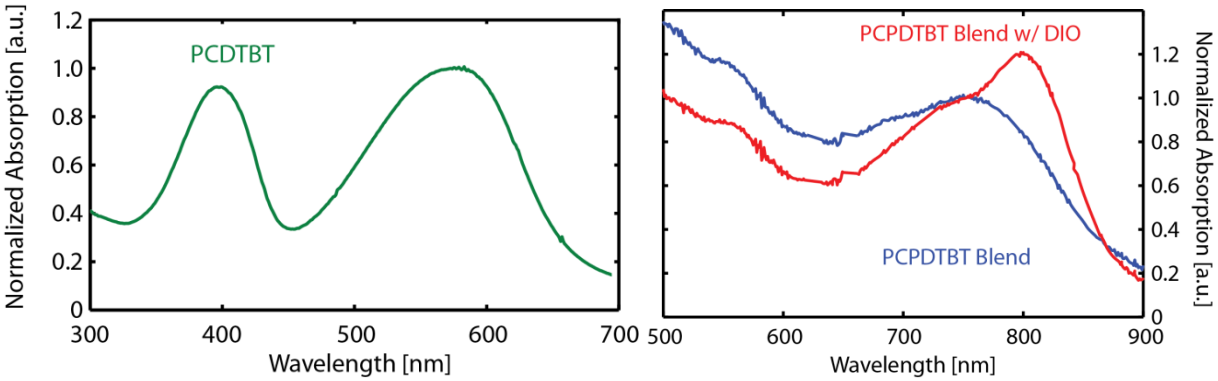

Figure 4.6. UV-Vis absorption spectra of neat films of PCDTBT (left) and blends of PCPDTBT with $PC_{71}BM$, with and without DIO additive (right).

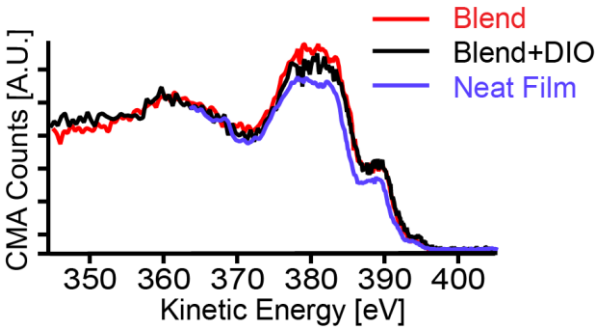

Figure 4.7. Resonant Auger spectra for a neat film PCPDTBT, a blend of PCPDTBT with $PC_{71}BM$ and a blend with DIO additive. Spectra are taken at the LUMO resonance with an incident x-ray energy of 398.5 eV.

4.7 Resonant Auger spectroscopy of PCDTBT

As discussed above, the LUMO of PCDTBT has similar overlap with the N atoms in the BT unit when compared with PCPDTBT. Based on the DFT calculations, we should expect a nearly identical spectator shift for PCDTBT as with PCPDTBT for excitation of N 1s electrons to the LUMO.

Figure 4.8a shows the N k-edge NEXAFS of PCDTBT. This part of the spectrum is composed of three resonances occurring before the onset of the N 1s absorption edge at 399 eV, 401.2 eV and 402.6 eV. These are similar to the excitations of N 1s electrons to unoccupied π* orbitals observed in PCPDTBT, though each is shifted to higher energy by 0.5 – 0.8 eV. Figure 4.8b shows the valence photoemission spectrum, taken at incident x-ray energy of 340 eV with binding energy calibrated using the second-order excitation of the N 1s electrons as performed for PCPDTBT. We observe four distinct valence bands, labeled J-M, and some emission at very low binding energy perhaps indicating gap states.

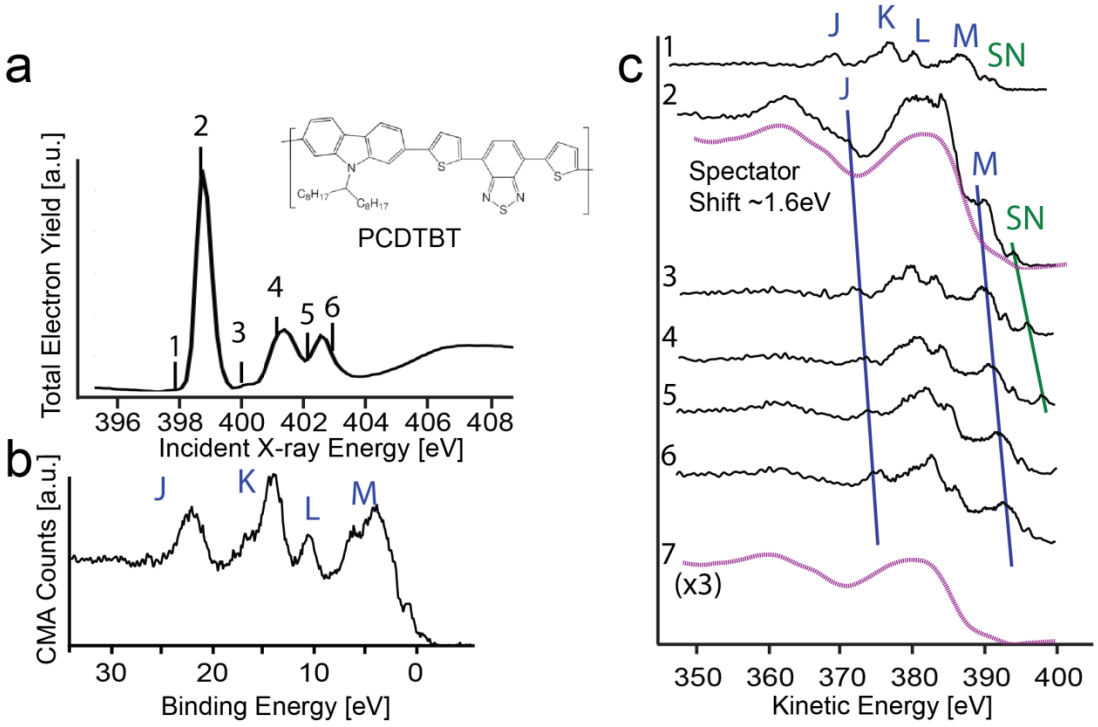

Figure 4.8. a) NEXAFS N K-edge total electron yield spectrum of a PCDTBT film taken at 20° incident angle. c) Photoemission spectrum of the same film taken at incident x-ray energy of 340 eV. d) Resonant photoemission spectra of the blend film. Spectra labeled 1-6 correspond to incident x-ray energies as labeled on (a). The light purple line on spectrum 2 represents the

spectator contribution of the fit used to determine the spectator shift. The spectrum labeled 7 corresponds to a pure Auger spectrum taken at incident x-ray energy of 440 eV. Peaks labeled J-M are valence photoemission peaks. Peak SN is second order light from the monochromator exciting N 1s electrons.

Figure 4.8c shows the photoemission spectra on a kinetic energy scale for PCDTBT, taken at incident x-ray energies marked 1-6 on Figure 4.8b. Spectrum 1 is composed of the valence photoemission features (J-M) and the second order excitation of N 1s electrons, labeled SN. Spectrum 7 is the non-resonant KLL Auger spectrum for the nitrogen atoms, taken at incident x-ray energy of 440 eV. The overall shape of the non-resonant Auger is nearly identical to that observed for PCPDTBT, apart from minor differences in the secondary peak shape. A \photoemission feature overlapped spectrum 7 at about 363 eV and was subtracted for fitting purposes. Determination of the spectator shift is complicated by the presence of feature J overlapping with the Auger dip for most of the resonant spectra. As with PCPDTBT, we fit spectra 2, corresponding to the LUMO excitation, using a combination of a scaled and shifted non-resonant Auger spectrum (spectrum 7) and the valence photoemission features. We observe that a spectator shift of 1.6 eV produces a good fit, reinforcing the similarities with the PCPDTBT LUMO observed in the DFT calculation. During the fitting process, we observe some evidence for participator enhancement of features K, L and M. This suggests that the LUMO wavefunction is spread across much of monomer, which is consistent with the DFT orbitals pictured in Figure 4.3. The Auger intensity was not high enough in the other resonant spectra to perform the fit reliably.

The measured spectator shift for the first resonance of PCDTBT is within 0.5 eV of the value predicted by our TD-DFT calculations and the final-state effect screening model. The spectator shift is very similar to that exhibited by PCPDTBT, which matched the predicted value to within less than 0.3 eV. Using this experimental technique, we have confirmed the similarities in the excited states of PCPDTBT and PCDTBT, especially their degree of delocalization, predicted by theoretical calculations.

4.8 Conclusions

N 1s x-ray absorption spectra were calculated for PCDTBT and PCPDTBT using TD-DFT and showed good agreement with the experimental NEXAFS spectra. The DFT virtual orbitals involved in the first x-ray resonance showed similar electronic structure in the two polymers, and population analysis revealed that a similar amount of the electron density is confined to the benzothiadiazole acceptor group. A final-state Auger parameter model using these electron densities successfully predicted the spectator shifts measured using resonant Auger spectroscopy, giving nearly identical overlap between the first excited state and the core hole (N 1s orbitals) for both polymers.

As the first x-ray resonance is dominated by the virtual LUMO and has π^* character, we assume that its electronic structure is similar to the optically excited electron. While PCPDTBT and PCDTBT have internal quantum efficiencies that differ by 30 percentage points, their chemical structures are similar and we observed no differences in the electronic structure of the LUMO. Although changes in morphology are known to affect device performance, we were unable to observe any changes in the x-ray resonant spectra. We conclude that the resonant

Auger technique is sensitive primarily to electronic structure of the monomer and that cannot explain differences in device performance between these two polymers.

4.9 References

1. Bredas, J. L.; Beljonne, D.; Coropceanu, V.; Cornil, J., Charge-transfer and Energy-Transfer Processes in Pi-conjugated Oligomers and Polymers: A Molecular Picture. *Chem. Rev.* **2004,** *104*, 4971-5003.

2. Dimitrakopoulos, C. D.; Malenfant, P. R. L., Organic Thin Film Transistors for Large Area Electronics. *Adv. Mater.* **2002,** *14*, 99-117.

3. Burroughes, J. H.; Bradley, D. D. C.; Brown, A. R.; Marks, R. N.; Mackay, K.; Friend, R. H.; Burns, P. L.; Holmes, A. B., Light-Emitting-Diodes Based on Conjugated Polymers. *Nature* **1990,** *347*, 539-541.

4. Guenes, S.; Neugebauer, H.; Sariciftci, N. S., Conjugated Polymer-Based Organic Solar Cells. *Chem. Rev.* **2007,** *107*, 1324-1338.

5. Dennler, G.; Scharber, M. C.; Brabec, C. J., Polymer-Fullerene Bulk-Heterojunction Solar Cells. *Adv. Mater.* **2009,** *21*, 1323–1338.

6. Clarke, T. M.; Durrant, J. R., Charge Photogeneration in Organic Solar Cells. *Chemical Reviews* **2010,** *110*, 6736–6767.

7. Bredas, J. L.; Norton, J. E.; Cornil, J.; Coropceanu, V., Molecular Understanding of Organic Solar Cells: The Challenges. *Accounts Chem. Res.* **2009,** *42*, 1691-1699.

8. Scholes, G. D.; Rumbles, G., Excitons in Nanoscale Systems. *Nature Materials* **2006,** *5*, 683-696.

9. Ohkita, H.; Cook, S.; Astuti, Y.; Duffy, W.; Tierney, S.; Zhang, W.; Heeney, M.; McCulloch, I.; Nelson, J.; Bradley, D. D. C.; et al, Charge Carrier Formation in Polythiophene/Fullerene Blend Films Studied by Transient Absorption Spectroscopy. *J. Amer. Chem. Soc.* **2008,** *130*, 3030-3042.

10. Yamamoto, S.; Ohkita, H.; Benten, H.; Ito, S., Role of Interfacial Charge Transfer State in Charge Generation and Recombination in Low-Bandgap Polymer Solar Cell. *J. Phys. Chem. C* **2012,** *116*, 14804–14810.

11. Hendry, E.; Schins, J. M.; Candeias, L. P.; Siebbeles, L. D. A.; Bonn, M., Efficiency of Exciton and Charge Carrier Photogeneration in a Semiconducting Polymer. *Phys. Rev. Lett.* **2004,** *92*, 4.

12. Kularatne, R. S.; Magurudeniya, H. D.; Sista, P.; Biewer, M. C.; Stefan, M. C., Donor-Acceptor Semiconducting Polymers for Organic Solar Cells. *J. Polym. Sci. Part A.* **2013,** *51*, 743-768.

13. Koller, G.; Berkebile, S.; Oehzelt, M.; Puschnig, P.; Ambrosch-Draxl, C.; Netzer, F. P.; Ramsey, M. G., Intra-and Intermolecular Band Dispersion in an Organic Crystal. *Science* **2007,** *317*, 351-355.

14. Huang, J. S.; Kertesz, M., Electronic Structures and Charge Transport Properties of the Organic Semiconductor bis 1,2,5 thiadiazolo-p-quinobis(1,3-dithiole), BTQBT, and its Derivatives. *J. Phys. Chem. B* **2005,** *109*, 12891-12898.

15. Gustafsson, J. B.; Moons, E.; Widstrand, S. M.; Gurnett, M.; Johansson, L. S. O., Thin PTCDA films on Si(001): 2. Electronic structure. *Surf. Sci.* **2004,** *572*, 32-42.

16. Bezel, I.; Gaffney, K. J.; Garrett-Roe, S.; Liu, S. H.; Miller, A. D.; Szymanski, P.; Harris, C. B., Measurement and Dynamics of the Spatial Distribution of an Electron Localized at a Metal-Dielectric Interface. *J. Chem. Phys.* **2004,** *120*, 845-856.

17. Szymanski, P.; Garrett-Roe, S.; Harris, C. B., Time- and Angle-Resolved Two-Photon Photoemission Studies of Electron Localization and Solvation at Interfaces. *Prog. Surf. Sci.* **2005,** *78*, 1-39.

18. Schmeisser, D., Valence states of Poly(3-hexyl-thiophene) as Probed by Photoelectron Spectra at Resonant Excitation. *Synthetic Met.* **2003,** 138, 135-140.

19. Gallet, J. J.; Jolly, F.; Rochet, F.; Bournel, F.; Dufour, G.; Avila, P. A.; Sirotti, F.; Torelli, P., Resonant Auger Spectroscopy of Poly(4-hydroxystyrene). *J. Electron Spectrosc.* **2002,** *122*, 11-25.

20. Stöhr, J., *NEXAFS spectroscopy*. Springer-Verlag: Berlin, 1992; p xv, 403 p.

21. Bruhwiler, P. A.; Karis, O.; Martensson, N., Charge-Transfer Dynamics Studied Using Resonant Core Spectroscopies. *Rev. Mod. Phys.* **2002,** 74, 703–740.

22. Vilmercati, P.; Cvetko, D.; Cossaro, A.; Morgante, A., Heterostructured Organic Interfaces Probed by Resonant Photoemission. *Surf. Sci.* **2009,** *603*, 1542-1556.

23. Nordlund, D.; Ogasawara, H.; Bluhm, H.; Takahashi, O.; Odelius, M.; Nagasono, M.; Pettersson, L. G. M.; Nilsson, A., Probing the Electron Delocalization in Liquid Water and Ice at Attosecond Time Scales. *Phys. Rev. Lett.* **2007,** 99, 217406.

24. Foehlisch, A.; Vijayalakshmi, S.; Pietzsch, A.; Nagasono, M.; Wurth, W.; Kirchmann, P. S.; Loukakos, P. A.; Bovensiepen, U.; Wolf, M.; Tchaplyguine, M.; et al., Charge transfer Dynamics in Molecular Solids and Adsorbates Driven by Llocal and Non-local Excitations. *Surf. Sci.* **2012,** *606*, 881-885.

25. Wurth, W.; Menzel, D., Ultrafast Electron Dynamics at Surfaces Probed by Resonant Auger Spectroscopy. *Chem. Phys.* **2000,** *251*, 141-149.

26. Peet, J.; Kim, J. Y.; Coates, N. E.; Ma, W. L.; Moses, D.; Heeger, A. J.; Bazan, G. C., Efficiency Enhancement in Low-Bandgap Polymer Solar Cells by Processing with Alkane Dithiols. *Nature Materials* **2007,** *6*, 497-500.

27. Park, S. H.; Roy, A.; Beaupre, S.; Cho, S.; Coates, N.; Moon, J. S.; Moses, D.; Leclerc, M.; Lee, K.; Heeger, A. J., Bulk Heterojunction Solar Cells with Internal Quantum Efficiency approaching 100%. *Nat. Photonics* **2009,** *3*, 297-U5.

28. Albrecht, S.; Schaefer, S.; Lange, I.; Yilmaz, S.; Dumsch, I.; Allard, S.; Scherf, U.; Hertwig, A.; Neher, D., Light Management in PCPDTBT:PC70BM Solar Cells: A Comparison of Standard and Inverted Device Structures. *Org. Electron.* **2012,** *13*, 615-622.

29. Besley, N. A.; Asmuruf, F. A., Time-Dependent Density Functional Theory Calculations of the Spectroscopy of Core Electrons. *Phys. Chem. Chem. Phys.* **2010,** *12*, 12024-12039.

30. Risko, C.; McGehee, M. D.; Bredas, J.-L., A Quantum-Chemical Perspective into Low Optical-Gap Polymers for Highly-Efficient Organic Solar Cells. *Chemical Science* **2011,** *2*, 1200-1218.

31. Chen, H.-Y.; Hou, J.; Hayden, A. E.; Yang, H.; Houk, K. N.; Yang, Y., Silicon Atom Substitution Enhances Interchain Packing in a Thiophene-Based Polymer System. *Adv. Mater.* **2010,** *22*, 371-375.

32. Perepichka, I. F.; Perepichka, D. F., *Handbook of Thiophene-Based Materials: Applications in Organic electronics.* John Wiley & Sons,: Chicester, 2009.

33. Cole, R. J.; Matthew, J. A. D.; Weightman, P., Extra-Atomic Relaxation Energy Calculations using an Extended Potential Model. *J. Electron Spectrosc.* **1995,** *72*, 255-259.

34. Cole, R. J.; Weightman, P., Separating Ground-State and Screening Contributions to Chemical-Shifts. *J. Phys.-Condens. Mat.* **1994,** *6*, 5783-5790.

35. Moretti, G., Auger Parameter and Wagner Plot in the Characterization of Chemical States by X-ray Photoelectron Spectroscopy: a Review. *J. Electron Spectrosc.* **1998,** *95*, 95-144.

36. Jackson, M. D.; Cole, R. J.; Brooks, N. J.; Weightman, P., Potential Parameters for Analysis of Chemical-Shift for the Elements Lithium to Argon. *J. Electron Spectrosc.* **1995,** *72*, 261-266.

37. Clarke, T.; Ballantyne, A.; Jamieson, F.; Brabec, C.; Nelson, J.; Durrant, J., Transient Absorption Spectroscopy of Charge Photogeneration Yields and Lifetimes in a Low Bandgap Polymer/fullerene Film. *Chem. Commun.* **2009**, 89-91.

38. Hintz, H.; Peisert, H.; Aygul, U.; Latteyer, F.; Biswas, I.; Nagel, P.; Merz, M.; Schuppler, S.; Breusov, D.; Allard, S.; et al. Electronic Structure and Interface Properties of a Model Molecule for Organic Solar Cells. *Chemphyschem* **2010,** *11*, 269-275.

39. Thompson, A. C.; Attwood, D. T.; Gullikson, E. M.; Howells, M. R.; Kortright, J. B.; Robinson, A. L.; Underwood, J. H.; Kim, K.-J.; Kirz, J.; Lindau, I.; et al. *X-Ray Data Booklet*, Center for X-ray Optics, Lawrence Berkeley Laboratory, Berkeley, CA **2001**.

40. Piancastelli, M. N., Auger Resonant Raman Studies of Atoms and Molecules. *J. Electron. Spectrosc.* **2000,** *107*, 1-26.

41. Kikuma, J.; Tonner, B. P., Photon Energy Dependence of Valence Band Photoemission and Resonant Photoemission of Polystyrene. *J. Electron Spectrosc.* **1996,** *82*, 41-52.

42. Ben Taylor, J.; Mayor, L. C.; Swarbrick, J. C.; O'Shea, J. N.; Schnadt, J., Charge-Transfer Dynamics at Model Metal-Organic Solar Cell Surfaces. *J. Phys. Chem. C* **2007,** *111*, 16646-16655.

43. Schnadt, J.; Bruhwiler, P. A.; Patthey, L.; O'Shea, J. N.; Sodergren, S.; Odelius, M.; Ahuja, R.; Karis, O.; Bassler, M.; Persson, P.; et al. Experimental Evidence for Sub-3-fs Charge Transfer from an Aromatic Adsorbate to a Semiconductor. *Nature* **2002,** *418*, 620-623.

44. Petraki, F.; Peisert, H.; Biswas, I.; Aygul, U.; Latteyer, F.; Vollmer, A.; Chasse, T., Interaction between Cobalt Phthalocyanine and Gold Studied by X-ray Absorption and Resonant Photoemission Spectroscopy. *J. Phys. Chem. Lett.* **2010,** *1*, 3380-3384.

45. Peisert, H.; Biswas, I.; Zhang, L.; Schuster, B. E.; Casu, M. B.; Haug, A.; Batchelor, D.; Knupfer, M.; Chasse, T., Unusual Energy Shifts in Resonant Photoemission Spectra of Organic Model Molecules. *Journal of Chemical Physics* **2009,** *130*, 194705- 194712.

46. Friedlein, R.; Braun, S.; de Jong, M. P.; Osikowicz, W.; Fahlman, M.; Salaneck, W. R., Ultra-Fast Charge Transfer in Organic Electronic Materials and at Hybrid Interfaces Studied using the Core-Hole Clock Technique. *J. Electron Spectrosc.* **2011,** *183*, 101-106.

47. Hamoudi, H.; Neppl, S.; Kao, P.; Schupbach, B.; Feulner, P.; Terfort, A.; Allara, D.; Zharnikov, M., Orbital-Dependent Charge Transfer Dynamics in Conjugated Self-Assembled Monolayers. *Phys. Rev. Lett.* **2011,** *107*, 027801-027805.

48. Collini, E.; Scholes, G. D., Coherent Intrachain Energy Migration in a Conjugated Polymer at Room Temperature. *Science* **2009,** *323*, 369-373.

49. Sirringhaus, H.; Brown, P. J.; Friend, R. H.; Nielsen, M. M.; Bechgaard, K.; Langeveld-Voss, B. M. W.; Spiering, A. J. H.; Janssen, R. A. J.; Meijer, E. W.; Herwig, P.; et al. Two-Dimensional Charge Transport in Self-Organized, High-Mobility Conjugated Polymers. *Nature* **1999,** *401*, 685-688.

50. Clark, J.; Silva, C.; Friend, R. H.; Spano, F. C., Role of Intermolecular Coupling in the Photophysics of Disordered Organic Semiconductors: Aggregate Emission in Regioregular Polythiophene. *Phys. Rev. Lett.* **2007,** *98*, 206406- 206409.

51. Friedlein, R.; Sorensen, S. L.; Osikowicz, W.; Rosenqvist, L.; Crispin, A.; Crispin, X.; de Jong, M.; Murphy, C.; Fahlman, M.; Salaneck, W. R., Electronic Structure of Conjugated Polymers and Interfaces in Polymer-Based Electronics. *Synthetic Met.* **2003,** *135*, 275-277.

52. Agostinelli, T.; Ferenczi, T. A. M.; Pires, E.; Foster, S.; Maurano, A.; Mueller, C.; Ballantyne, A.; Hampton, M.; Lilliu, S.; Campoy-Quiles, M.; et al. The Role of Alkane Dithiols in Controlling Polymer Crystallization in Small Band Gap Polymer:Fullerene Solar Cells. *J. Polym. Sci. Pol. Phys.* **2011,** *49*, 717-724.

53. Yamagata, H.; Spano, F. C., Interplay Between Intrachain and Interchain Interactions in Semiconducting Polymer Assemblies: The HJ-aggregate Model. *J. Chem. Phys.* **2012,** *136*, 184901-184914.

Chapter 5: Future Directions

In this dissertation, I have demonstrated that phenylphosphonic acid (PPA) forms a well-ordered self-assembled monolayer (SAM) on indium tin oxide (ITO), with a well-defined orientation with the phenyl ring plane tilted at an angle of 15 ± 4° from the surface normal. I also found well-defined orientations in fluorinated and non-fluorinated alkyl and aliphatic PA SAMs on ITO. The effect of fluorination on the orientation is non-trivial, due to the combined effects of the fluorination on binding mode and steric packing. The latter effects are found to be more dominant in aliphatic SAMs, leading to a more upright orientation in the fluorinated SAM. In the aromatic case, the fluorinated SAM adopted a less upright orientation which I attribute to changes in binding mode.

The agreement of our near-edge x-ray absorption fine structure (NEXAFS) results with the fundamentally different surface IR technique, polarization modulated-IR reflection-absorption spectroscopy (PM-IRRAS), is a strong indicator of the reliability of the technique and my data processing methods. As a result of this agreement and with support from x-ray photoelectron spectroscopy (XPS) data, my collaborators were able to correct earlier vibrational peak assignments in the IR spectra of phosphonic acids that are critical to determining molecular orientation. Furthermore, I have compared the NEXAFS data with DFT calculations of the molecular geometry of the aromatic SAMs with excellent agreement. This agreement strongly indicates that intermolecular forces are not dominant in the orientation of aromatic PA SAMs on ITO.

This research leaves some unanswered questions for the system of PA SAMs on ITO, however. NEXAFS alone has proved insufficient to distinguish between the various fluorination positions

on the aromatic benzylphosphonic acid (BnPA), due either to high disorder in the monolayer or an orientation of the benzyl group normal very near the NEXAFS "magic angle". In order to gain a complete picture of the effect of fluorination position on an aromatic SAM, one needs a more comprehensive study. The combination of NEXAFS, ultraviolet photoelectron spectroscopy (UPS), and DFT calculations of work-function shift and geometry should lead to a more complete picture. The goal of such a study would be to compare the measured work-function shift and orientation with DFT calculated values. If the gap between theory and measurement is large in a particular SAM, it is likely disordered or exhibits strong inter-molecular forces not accounted for in the DFT calculated geometries. The ratio of bidentate to tridentate bonding and how it varies with fluorination position could be explored in the comparison of measured and calculated orientations and by measuring pK_a values.

The binding mode of PA SAMs in this research has been inferred from the comparison of theoretical orientations and measurement. In principle, PM-IRRAS could determine the binding mode through a measurement of stretching modes for P-O, P=O and O-H bonds. In practice, this has proven difficult due to low signal but should be possible with further refinement. Thermo-gravimetric analysis and calorimetric measurements might also provide a way to determine the binding mode definitively. Both techniques can provide a quantitative measure of the strength of the SAM-substrate binding. A comparison of the fluorinated and non-fluorinated PPA derivatives might prove useful for these two techniques.

NEXAFS is a very general technique, and can be used to measure the orientation of many monolayer systems. It also has chemical specificity, and can be used in polymer fingerprinting. The surface composition (vertical morphology) of any polymer-fullerene blend can be explored

using NEXAFS: all that is needed is to compare the NEXAFS spectrum of the blend to a neat film of each component in the blend. Some new beamlines (2-3, 6-2, 14-3) at SSRL are able to perform x-ray spectroscopic images with spatial resolution of 2 μm or larger. Imaging studies could be helpful in examining spatially patterned SAMs or investigating in-plane morphology and phase-separation in active-layer materials for organic solar cells.

N 1s x-ray absorption spectra were calculated for PCDTBT and PCPDTBT using TD-DFT and showed good agreement with the experimental NEXAFS spectra. The spectator shift determined by the N k-edge resonant Auger technique allowed for a measurement of overlap between the LUMO and the N atoms in the benzothiadiazole acceptor group. These spectator shifts are similar to those predicted from the TD-DFT population analysis using a final-state Auger parameter model. Both polymers exhibited similar spectator shifts in the resonant Auger spectra. Since my resonant Auger results showed no significant correlation with morphology or device performance, I conclude that the resonant Auger technique is sensitive primarily to electronic structure of the monomer, which cannot explain the differences in device performance between these two polymers. Based on this, and the inapplicability of the core-hole clock method, I believe polymer films are not the ideal system to explore with this technique.

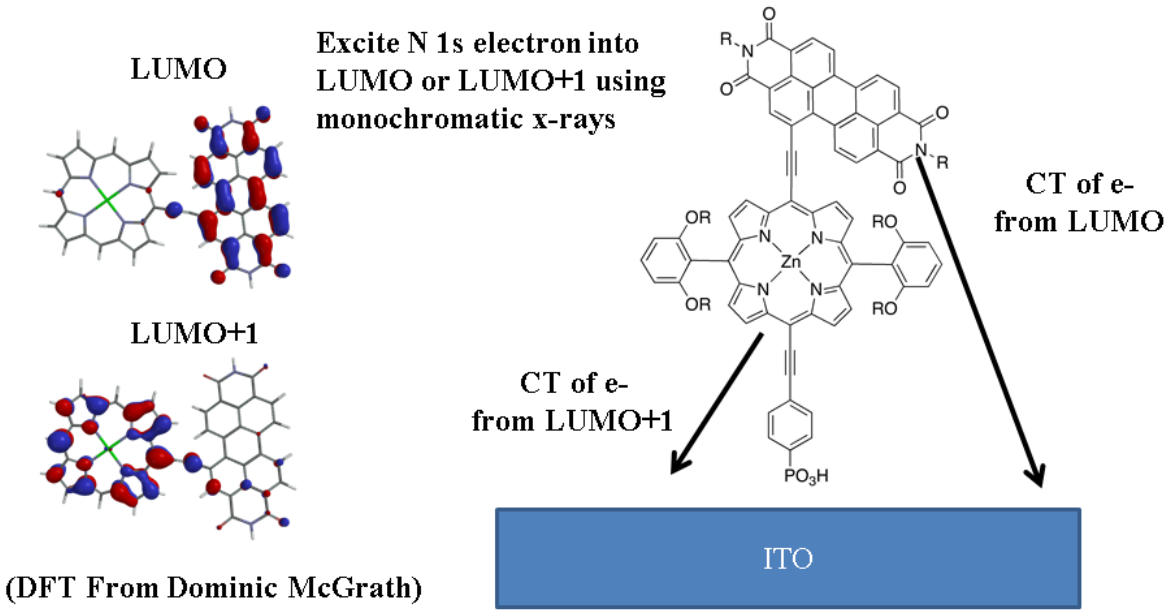

Figure 5.1. DFT molecular orbitals for a Zn-porphyrin/perylene diimide dyad.(Left) Schematic of core-hole clock experiment.(Right)

A main strength of the resonant Auger technique lies in the core-hole clock method for determining the time-scales of femtosecond charge transfer processes. The core-hole clock method is most easily applied to systems of a small molecule on a large conducting substrate. Dyads on metal oxides form an interesting and tractable system for use with this technique. Figure 5.1 shows an example of a dyad composed of a donor (Zn-porphyrin) and an acceptor (perylene diimide) component. The dyad molecule provides a simple single-molecule alternative to the complex polymer-fullerene bulk-heterojunction solar cell. Time-resolved optical pump-probe spectroscopies can probe the lifetime of the optically excited state, which contains information about multiple decay pathways. Resonant Auger spectroscopy can excite core electrons to unoccupied orbitals on the donor and acceptor regions separately. Since resonant spectroscopy does not create excitons or a valence hole, charge transfer processes from each

dyad component to the substrate can be isolated. The core-hole clock method could potentially measure the timescales of charge transfer for either pathway. This information, combined with time-resolved optical pump-probe measurement could provide a comprehensive picture of the charge dynamics in this model system.

Chapter 6: Methodology

6.1 Materials

Super-smooth 100 nm ITO on glass substrates were purchased from Thin Film Devices (Anaheim, CA). Atomic force microscopy scans (Figure 3.6) reveal a surface roughness of 0.7-0.8 nm (RMS) over a 100 nm length scale. Evaporated Au on glass slides for PM-IRRAS experiments with 1.5-2.0 nm root-mean-squared (RMS) roughness were purchased from Evaporated Metal Films (Ithaca, NY). In the PM-IRRAS experiment, Au films on glass were selected as the underlying platform for thin IZO films because of their infrared reflectivity. Thin IZO overlayers of 5-10 nm thickness were sputtered onto evaporated Au on glass slides from a 3 in., 70:30 (wt %) In2O3:ZnO target in a chamber with a base pressure of 10^{-6} Torr at a deposition pressure of 4.5 mTorr. During an 8.5 s deposition, the oxygen flow was maintained at 0.5 sccm, and the argon flow at 13.4 sccm, with a DC sputtering power of 100 W. Phenylphosphoinc acid (PPA), 1,8-diiodooctane (DIO), ethanol, acetone, triethylamine, chloroform, mesitylene, chlorobenzene and dichlorobenzene were purchased from Sigma-Aldrich and used without further purification. The synthesis of *n*-octylphosphonic acid (OPA)[1], 3,3,4,4,5,5,6,6,7,7,8,8,8-tridecafluorooctylphosphonic acid (F_{13}OPA)[2], and 3,4,5-trifluorophenylphosphonic acid (F_3PPA)[3] were reported elsewhere in the literature. Synthesis of all benzyl-phosphonic acids (BnPA) were conducted at Georgia Institute of Technology by Anthony Giordano.

[6,6]-phenyl-C_{71}-butyric acid methyl ester ($PC_{71}BM$) was purchased from Nano-C. Regioregular poly(3-hexylthiophene) (P3HT) (M_w = 35.40 kDa, PDI = 2.45) was purchased from Rieke Metals, Poly[[9-(1-octylnonyl)-9H-carbazole-2,7-diyl]-2,5-thiophenediyl-2,1,3-benzothiadiazole-4,7-diyl-2,5-thiophenediyl] (PCDTBT) and Poly[2,6-(4,4-bis-(2-ethylhexyl)-

4H-cyclopenta[2,1-b;3,4-b0]-dithiophene)-alt-4,7-(2,1,3-benzothiadiazole)] (PCPDTBT) were purchased from 1-Material.

6.2 Substrate cleaning and PA modification

The thin IZO films were detergent cleaned and sonicated for 10 min in acetonitrile, followed by 5 min in isopropyl alcohol, and dried under a N_2 stream after each step. Next, the substrates were placed into a Harrick Plasma Cleaner PDC-32G (Harrick Plasma, Ithaca, NY) and plasma cleaned for 10 min at an RF power of 10.5 W in a chamber fed by an oxygen pressure of ~400 mTorr.

Thick film (~100 nm) IZO on glass substrates were used for NEXAFS data collection and prepared using the same sputtering methods described above for the thin IZO films on Au. These films and the Super-smooth ITO films were sonicated in acetone for 10 min then scrubbed with Micro-90 electronics-grade detergent in deionized water (DI). Substrates were then successively sonicated in a solution of Micro-90 and DI, then Milli-Q DI, then ethanol, for 10 min each. Substrates were then oxygen plasma cleaned under a 100 mL/min flow of O_2 for 5 min at 18 W power at 100 MHz using a Harrick Plasma PDC-32G plasma cleaner.

Cleaned substrates were immersed in 10 mM PA solutions in ethanol for either 48 hours at room temperature, 48 hours at 70°C (samples herein referred to as 70°C), or one week (168 hours) at room temperature. Upon removal from solution, substrates were rinsed with ethanol, blown dry in a stream of N_2, and annealed under rough vacuum for 2 hours at 140°C. Samples were then rinsed with ethanol and blown dry.

To prepare the microcontact printed samples, a procedure was used that has been shown to produce SAMs with local workfunction shifts comparable to those reported in early solution-deposited methods.[4] However, to improve signal in NEXAFS experiments, a flat featureless PDMS stamp was used instead of a patterned stamp. The stamp was first rinsed with ethanol and blown dry in a stream of N_2. The stamp was then "inked" with a 10 mM PA solution in ethanol, and blown dry in a stream of N_2. The inked stamp was immediately pressed into contact with the freshly plasma cleaned substrate and held in place by a ~35 g weight for 10 minutes. Upon removal of the stamp and weight, the substrate was annealed on a pre-heated 140°C hot plate for 5 minutes, and then rinsed with ethanol and blown dry. The substrates were then sonicated in a 5% triethylamine: 95% ethanol solution (v/v) for 30 minutes, rinsed well with ethanol, and blown dry.

Each of the samples made for chapter 2 utilize the 168 hour soak method. All of the samples in chapter 3 utilize the 48 hour, room temperature soak unless otherwise noted.

6.3 Polymer thin film preparation (Dana Sulas, University of Washington)

To produce thin-film polymer and bulk-heterojunction samples for resonant Auger spectroscopy studies, solutions of the polymers with or without fullerene were spin-coated onto ITO substrates cleaned as discussed in section 6.2. For P3HT samples, 60 µl of solution of 10 mg/mL P3HT in Chloroform or Mesitylene was coated at 500 rpm for 5 s and 1750 rpm for 120 s then annealed for 1 hour at 100°C. PCDTBT samples were coated at 60°C from a 10 mg/mL solution in dichlorobenzene at 500 rpm for for 5 s and 2000 rpm for 300 s. PCPDTBT samples were spin-coated with or without fullerene and with or without the diiodooctane (DIO) solvent additive. In the neat films, a 10 mg/mL solution of PCPDTBT was coated from either

chlorobenzene or from a mixture of 2.5 vol% DIO in chlorobenzene. Blend films were coated from a 3:1 solution of $PC_{70}BM$ and PCPDTBT (10 mg/mL) in either chlorobenzene or the chlorbenzene-DIO mixture. Samples were spun at 500 rpm for 5 s and 1750 rpm for 120 s.

6.4 NEXAFS experimental Setup

The NEXAFS data were acquired at Stanford Synchrotron Radiation Lightsource (SSRL), at the bending magnet beamline 8-2.[5] The slit-to-slit SGM monochromator has an optimal resolution of better than 100 meV in the carbon region, but was operated at a lower resolution of about 200 meV for most measurements in order to maximize throughput while still resolving the features needed for the angular dependence analysis. The toroidal refocusing optics provided a near circular beam cross-section of about 1 mm in diameter. The incoming photon flux was recorded from a gold covered wire mesh (gold grid) intercepting a few percent of the beam, via the drain current by a Keithley 428 picoammeter. In order to ensure a proper normalization without artificial structures from contaminants, a fresh layer of gold was evaporated onto the grid before the start of each run. Second-order contributions from the beamline monochromator were supressed by a Ti filter, inserted upstream of the gold grid, which strongly absorbs photons above the Ti L-edge at ~460 eV. The absolute beam energy was calibrated by measuring highly oriented pyrolytic graphite (HOPG), assigning the energy of the π^* feature to 285.38 eV.[6] To compensate for small monochromator drifts over the course of the day, the lower energy dip in the gold-grid absorption spectrum (corresponding the residual carbon on the optics in the beamline and assumed to be constant) was used to align all spectra to the same absolute calibration during individual runs.[5] The degree of linear polarization is assumed to be 0.85+/-0.05, based on recent measurements on this beamline,[5] although one paper has reported polarization as high as 0.99.[7]

The uncertainty in polarization is accounted for in the analysis below, and results in only a 2-degree systematic uncertainty in the final result, with any overestimation of the polarization leading to a measured orientation systematically shifted towards the magic angle, 54.7° (and vice versa).[8] All NEXAFS measurements were conducted at base pressures below 10^{-8} Torr. NEXAFS spectra are recorded in two modes simultaneously; total electron yield (TEY), measured as the sample drain current by a Keithley picoammeter, and the Auger electron yield (AEY), measured by a PHI 15-255G double pass cylindrical mirror analyzer (CMA) operated in pulse counting mode. The CMA analyzer was set to a pass energy of 200 eV for highest throughput and operated at a fixed kinetic energy of 257 eV, which is part of the broad carbon Auger distribution and chosen specifically to shift contribution from non-NEXAFS features resulting from first and second order photoemission peaks to energies below the onset of the C k-edge NEXAFS spectrum (285 eV). The experimental setup is shown in Figure 1.6.

6.5 AEY background removal

Figure 6.1 shows a typical AEY spectrum for PPA deposited on IZO using the 168 hour soak method, obtained under the parameters defined in section 6.4. The raw NEXAFS AEY spectra contain Auger peaks and photoemission peaks from the carbon valence electrons, as well as photoemission peaks from the substrates.[8] The non-Auger features can be understood by also plotting the data on a binding energy scale (top axis) in which:

[Binding Energy] = [Incident Photon Energy] - [CMA Energy = 257eV] - [Work Function].

The C valence band contribution was present at 263 eV along with photoemission from the shallow substrate orbitals. In the energy range of interest (NEXAFS region from ~ 284 eV to 310 eV), the photoemission contribution was rather smooth with little fine-structure to affect the

Auger intensities. The presence of the photoemission peaks from the substrate demonstrates that the thickness of our monolayer samples is on the same order as the escape depth of electrons from substrate excitations or that there are bare patches. Anisotropy of the photoemission peaks is indicative of the former.

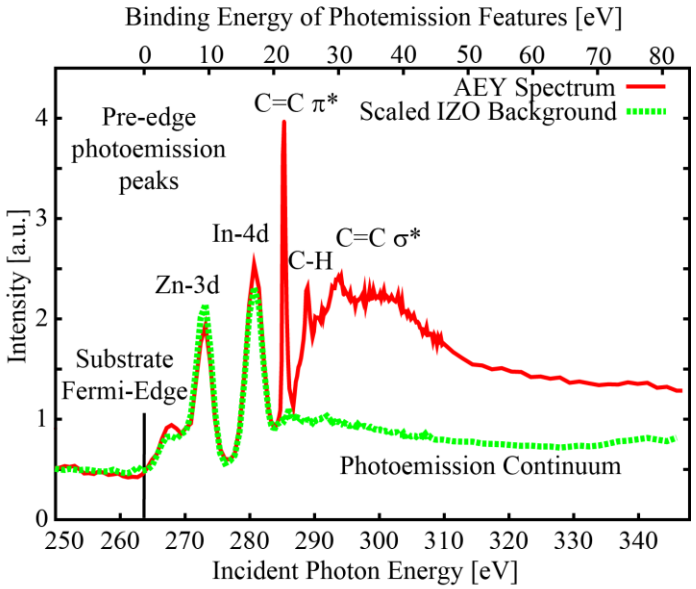

Figure 6.1. Raw AEY NEXAFS spectra for a sputter-cleaned IZO substrate (green curve) and a phenyl phosphonic acid SAM (red curve) on IZO collected at 55° incidence. The green curve has been scaled to fit to the pre-edge photoemission features as is done during the background subtraction step of data processing.

To remove the substrate background contribution, a bare IZO sample was sputtered with a large unfocused ion beam using Ar at a pressure of $4*10^{-5}$ torr, with a current of 20 mA and a driving voltage of 1 kV for 70 min to remove any carbon contamination. The spectra from this sputter-cleaned substrate were scaled to fit the pre-edge features of each of our sample spectra and subtracted. This subtraction was performed independently for each sample at each incident beam angle. Figure 6.1 shows such a scaled sputter-cleaned substrate spectrum. Since the CMA was fixed in orientation perpendicular to the incident radiation, the electrons from the substrate are more strongly suppressed at normal incidence due to the finite electron penetration depth, which makes the background subtraction

process anisotropic.[9] Our largest source of uncertainty is thus systematic and results from this correction step. When fitting the background there was a choice of two major features: by performing the analysis using a background fit to either feature or both simultaneously I computed this systematic uncertainty, which is approximately 3 degrees in the final result.

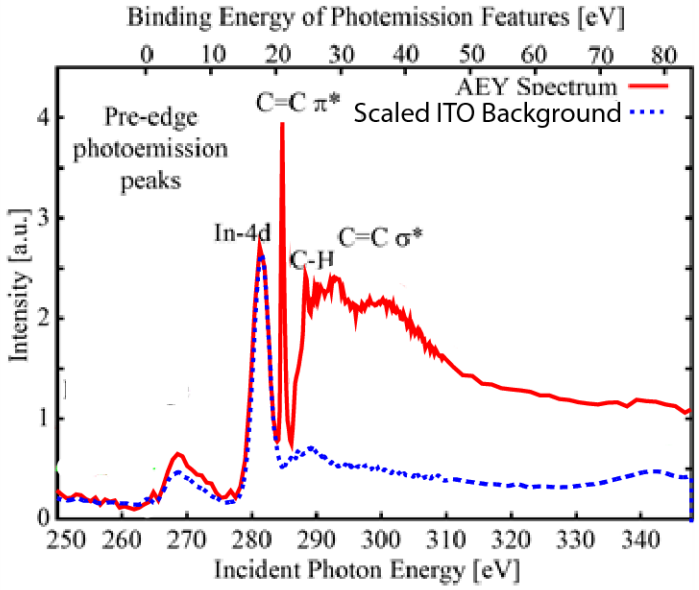

Figure 6.2. Raw AEY NEXAFS spectra for a sputter-cleaned ITO substrate (blue curve) and a phenyl phosphonic acid SAM (red curve) on IZO collected at 55° incidence. The blue curve has been scaled to fit to the pre-edge photoemission features as is done during the background subtraction step of data processing.

The background subtraction process for PA samples on ITO is very similar. Figure 6.2 shows the removal of a sputter cleaned ITO background. Since the Zn-3d feature is not present, the background fit is similar and the systematic uncertainty involved in this step is significantly reduced. Systematic uncertainty for the ITO samples is calculated using the difference in orientation reported by the AEY and the TEY data.

6.6 TEY background removal

A second-order polynomial background contribution to the sample current was subtracted prior to normalizing the signal by the gold grid. In the absence of this background, pre-edge artifacts arose at about 285 eV and 291 eV. These artifacts are related to the dips in the beam

intensity due to intrinsic carbon in the beamline optics. When the appropriate background is subtracted, the gold-grid normalization removes this structure. I believe the background is primarily from ion current due to the nearby ion pump. The background depended on the location of the samples on the mounting stick and varied with time. The background was found to gradually vanish after about 48 hours after pump-down was completed.

6.7 NEXAFS spectral processing

The final data processing steps included normalization and averaging between samples for noise reduction. The sample was normalized to an arbitrary average height of 1.8 in the background past the edge step (343-346 eV). Oscillatory behavior in this range, commonly known as extended x-ray absorption fine structure (EXAFS), was not large enough to require a wider normalization range. After normalization, three spectra for each sample type and angle were averaged together in a three-step process as follows: first, an average spectrum was computed. Second, the individual spectra were scaled and shifted on the incident photon energy axis to best match the average. Finally, the modified spectra were averaged together to create the corrected spectrum used for peak fitting and angular dependence studies. I use this process to mitigate any monochromator drift that may be present, which would have resulted in a shift of the spectrum along the energy axis. For all samples on ITO, the sample-sample variation was found to be very small. The systematic uncertainty from the data processing steps are discussed in section 6.5.

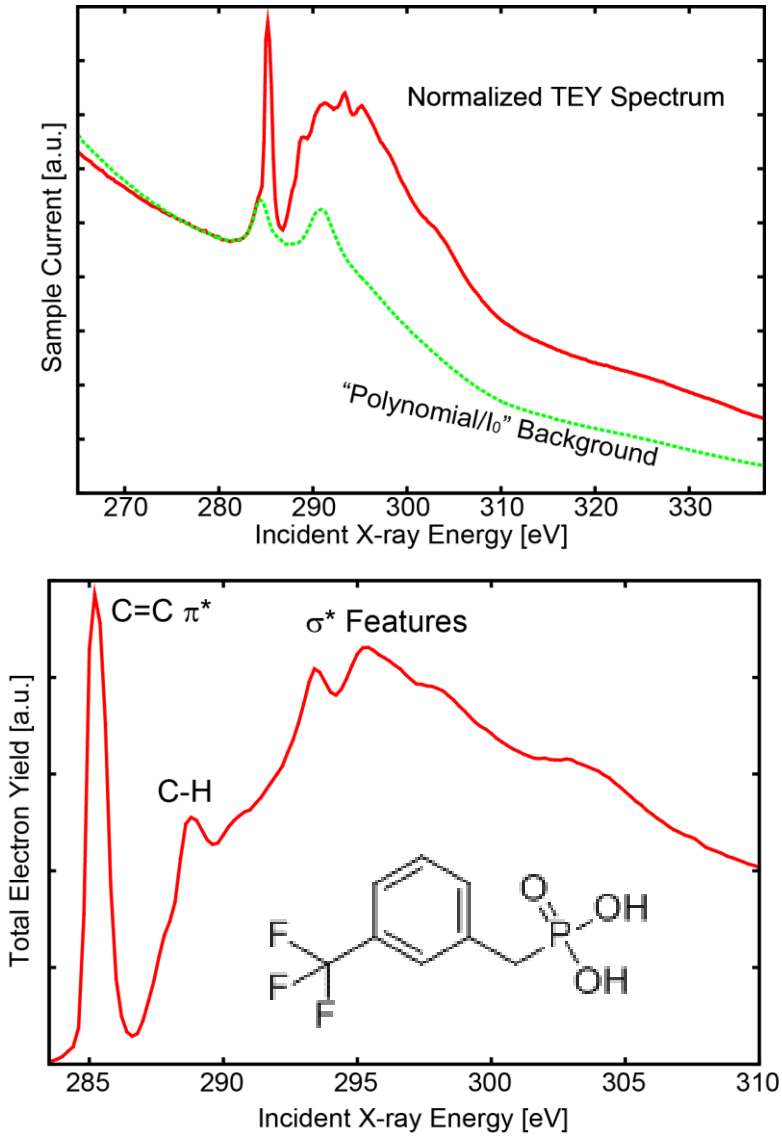

Figure 6.3. Top: Raw TEY spectrum given by sample current (red line), Green line is smooth background signal subtracted. Bottom: The same TEY spectrum after background removal. Spectra correspond to 2-(CF_3)BnPA on ITO, deposited in the 48 hour, room temperature method at 55° incident x-ray radiation.

6.8 Using the NEXAFS data processing code

This section describes how to use my custom code for the software to analyze x-ray spectroscopy data gathered in a large batch from beamlines which use SPEC, SUPER or XAS as

interfaces (such as SSRL beamlines 8-2 or 10-1). Portions of this software were originally written by Andreas Tillack in 2010, but have been extensively modified. The code performs various processing tasks, including background subtraction and averaging, on a data set with minimal programming knowledge required. The use of more advanced or data-specific processing techniques require the ability to reprogram this code or importing the data into Matlab. Most of these processing tasks can be performed (albeit not in a batch process) using Bruce Ravel's Athena software, available free online at http://cars9.uchicago.edu/ifeffit/BruceRavel/Horae.

Installation

All of the code is self-contained in the shared/ SSRL/SSRL analysis folder and installation is required. The main folder contains several folders, and the code relies on this exact directory structure. The "programs" folder contains versions of gawk, gnuplot and notepad++. The only installation required is the association of .plt files with notepad++. This is achieved by right-clicking on any file with the ".plt" extension (such as "Main_Initialize.plt" in the main folder) then select "Open with..." and choose "Browse..." to point to "Programs\Notepad++\notepad++.exe". If need be, you can install Gawk, gnuplot and notepad++ on your own into their respective folders in the "programs" folder. Ghostscript and Ghostview should be installed on your computer as well, since the plots are produced in .eps format.

Definitions and program structure.

The code's directory is built from several important folders. The following are inside the main directory: Programs: contains gawk, gnuplot, notepad++; Reference Data: contains data

about the gold cross section which is used in conjunction with gold-grid data in the raw data file in the normalization. Functions; contains scripts executed by notepad++ in a windows shell using gnuplot; and Scripts: contains the awk programs which modify the data files line by line. The code files in the Functions folder each have the ".plt" extension. This folder contains analyze_file.plt, which accesses the raw data files, picks out the types of data from different channel, ratios it with the gold-grid reference, and calls the various background subtraction routines. Here also is the code that takes averages, (average_files.plt, corrected_file.plt), performs data-to-data fit(fit1to1.plt), normalizes files, etc, and produces all the associated plots. The files in the Scripts folder all have the ".awk" extension. The code in this folder performs plotting routines and call awk routines. Create_analysis.awk writes the analysis scripts for each data sample. If you would like to add processing steps, such as angular dependence and peak fitting, these steps should be called from this file.

The template folder provides a model of how the folder which contains your data and output will be structured, you must copy this directory and renameit for each set of data you process. Inside your data folder, there will be an excel spreadsheet which should contain the names of all of your data files as discussed in the following subsection. There will also be a program, "Run Data Analysis", which allows you to set your basic processing options and execute the data processing itself. "Raw Data Files" should contain your SUPER, SPEC or XAS output files, unmodified. "Data Analysis" contains the output of your analysis. "Data Analysis/Plots" and "Data Analysis/Processed Data Files" store the plots and .dat files put out by the program during the analysis respectively. After running the code, three scripts will be produced in the "Data Analysis" folder: "Reference(autogenerated).plt",

"Analyze(autogenerated).plt", and "Peak Analysis (autogenerated).plt" These are written by the "create_analysis.awk" script. In order they perform the analysis on reference data (such as substrate spectra that might be used in background subtraction), main data, and advanced processing like angular dependent fits which are not supported for basic users. Lastly, in the parent directory there is a configuration file called "Main_Initialize.plt". This function sets the file directories and initializes variables. Changing this code can toggle PDF output on/off, and change other options that might affect stability.

Running the analysis

First, copy the template directory and rename it to identify the data set you are working on. Second, copy the raw data files into the labeled directory. You must save a tab-delimited text file named "Sample Info.txt" containing information on all of the raw data files to be processed. This is easily done using an excel spreadsheet saved as tab-delimited text once filled out. The excel spreadsheet must have the following columns in order:

1. Running number: order tests are run in, helps to distinguish tests on the same sample from one another.
2. Data Type: AD is the type for most data that will be analyzed. Lines with the Reference data type will be processed first, and can be subtracted from the other spectra as a form of background removal. Other data types can be used, like AD analysis to add steps to the processing script like angular dependence fits.
3. Use? : y or n, determined whether or not the spectrum will be used in the analysis.
4. Sample Type: used to group samples that will be analyzed together.

5. Sample number: distinguish between different samples of the same type.
6. Angle: incident radiation angle
7. Nexafs filename: the exact filename as output by super or xas and stored in your "raw data files" folder.
8. Other fields: slits/pass energy; range; comments Useful for book keeping. The comments will show up as comments in the analysis script for the different files. This field is also used in some advanced features.

Once the excel file is saved, the "Run_DataAnalysis.plt" file in your data directory should be opened in notepad++ and excecuted by pressing F9. Several data analysis options are available in the Run Data Analysis file, and shoud be set carefully before proceeding. "Sample_Log" should be set to the name of your tab-delimited text file. The program will skip processing steps if it thinks it has already done them, in order to save time; "Force_Reprocess=1" disallows this.

The channels for AEY data (from the CMA), TEY data and Gold-grid data can be set here. Gridref is the variable that controls the column number for the gold-grid. Column 1 is the energy value, column 2 is channel 1, etc. The number you enter is the column value. Entering a value of 0 for AEY or TEY will disable all processing of that data type. The processed AEY and TEY data will have been normalized by the incident energy using the gold-grid data and the gold-cross section information stored in the reference-data folder.

"Data_start" and "Data_end" tell the program where to expect the data to fall on the energy scale. The program can adapt to discrepancies of a couple eV between samples. "Fit_start" and "Fit_end" are used to specify where in the spectra are the peaks of interest. No normalization or background removal will use this area. "Int_start" and "Int_end" specify the post-edge region

used to normalize the total number of counts. The background removal areas for AEY and TEY can be specified separately. The TEY background removal will end at "Fit_start". Subtraction of substrate reference data from AEY can be enabled or disabled, as can the ad-hoc AEY and TEY backgrounds. The exact functional form of these backgrounds can be changed in the "Functions/Analyze_File.plt" file.

Output files

Each sample will have several processed data files, saved after various processing steps. AEY and TEY data are processed differently. All of these files are in the "**Your data folder**/Data Analysis/Processed Data files" directory. In the following filename descriptions, *N* refers to sample number, *T* refers to sample type, *F* refers to the filename of the raw data file *A* refers to incident x-ray angle and*R*, refers to running number.

The x-ray energy values, AEY and TEY data are extracted from each raw data file and saved as "*T* *N*.*R* *A* deg data.dat". The AEY data undergoes substrate background removal and normalization. The raw AEY data and scaled substrate background are saved as "*T* *N*.*R* *A* deg corrected (AEY) data.dat". The AEY data after subtracting the background and normalizing by the edge step is saved as "*T* *N*.*R* *A* deg corrected and normalized (AEY) data.dat".

Each data of the same type is then averaged. The averaged TEY data is saved as "*T* *A* deg.dat". The averaged AEY data is saved as "*T* *A* deg corrected and normalized.dat" Data from each sample is fit to the average to create the "*T* *N*.*R* *A* deg to average (T[A]EY) data.dat" These fits are averaged to make the "Average *T* *A* deg corrected (TEY)

.dat" and "Average *T* *A* deg doublecorrected and normalized (AEY).dat" files. These files are similar to the simple average, but reduce the impact of monochromator drift.

Output plots

Plots are divided into 5 subfolders. First, "Averages" contains plots of averages of a particular sample type at a particular angle and includes the spread of data as a visual representation. "Peak-Fitting" contains visualizations of background subtractions (figures ending in "corrected.eps") and fits of data to average. If data is present from the same sample type atmultiple angles of incidence, the "Comparisons" folder contains plots of each sample type at all available angles. The "General" folder contains plots of various intermediate steps, these are not very interesting and only useful for debugging. Lastly, the "Angular Dependence" folder will contain peak fits and fits of the angular dependence equations if these steps are performed.

Advanced options

There is no user-friendly way to access the functionality described here. Unless you are good at programming and/or have experience with awk, this would be best undertaken in MATLAB for each of your output spectra on a case by case basis.

TEYmethod_I.plt performs the subtraction of a substrate background and can be enabled by uncommenting in create_analysis.awk. It works fine, though the region where the fit is performed must be tweaked in the program manually. I never found reference data subtraction in the TEY to be useful, but maybe you will. TEYmethod_II.plt creates the difference spectra by subtracting the data gathered at 55 degrees from the each spectrum. This one is a bit glitchy because my awk-ing skills are not up to par. The framework works though, and this can, with

effort, be re-enabled by tweaking certain lines in create_analysis.awk The spectra at 55 degrees are not necessarily processed first, so doing this on a first data run will not work.

Peak fitting of spectra for angular dependence can be undertaken in two ways. For a rough, qualitative estimate, the first method uses the height of the peak maximums near the specified point. To achieve publication-quality results however, you must use the second method which fits peaks and calculates the area beneath.

In order to use the peak heights method, there is a section commented out in "Create_Analysis.awk" which writes lines for the "getpeakmax.awk" script, which can be enabled.

In order to use the more correct peak fitting method, there is a section in "Create_Analysis.awk" near the one above which calls a fitting routine specific to each molecule. The batch fitting program needs to be writted for each sample type using one of my existing peak fitting programs for a template. The fitting routines are in the "functions" directory and titled "getpeakarea*T*.plt". These perform fits of the peak of interest and nearby ones along with an edge function. The "reportpeakmax.awk" script is used to locate the peak exactly based on a guess and return its height and location via a file in the processed data directory. The fits have many parameters and may need to be rerun multiple times with clever guesses. Make note of the fit command and its syntax. Online references for gnuplot will be helpful. The areas and errors are calculated from the fits and the spread in heights of the initial spectra. The values for each angle are kept in a running list in "processed data files/*T*xxxeVAD.dat" for each sample type. This file will need to be cleared of bad fits or deleted if you start over. The lines fed to this file are used by the "AD Analysis" script.

To run angular dependence (AD) analysis, enter the commands into the Excel table (and corresponding "Sample Info.txt"). Listed below are examples of commands and the information that should be contained in each column for the program to properly execute. This will not work unless some sort of peak-fitting routine is enabled.

I. Running #: "0"

II. Data type: "AD Analysis"

III. Use?: "TEY" (or "AEY")

IV. Sample Type: "Sample Name"

V. Angle: 20 35 45 55 65 75 90 or whichever angles you took data at.

VI. Comments: (e.g. "v:285.38" ➔ vector fit at 285.38 eV), The direction of the orbitals are indicated by the following abbreviations. Fit equations are defined in "functions/AD_functions.plt" and come from Stohr.[8] They are also given in chapters 2 and 3, Equations 2.3 and 3.3 are examples. v: vector (e.g. C=C π^*), p: plane (e.g. C–F σ^*) to describe transition dipole moments spanning a plane. Tc = tilted chain model, described in Equation 3.3

6.9 Peak fitting and angular dependence of NEXAFS spectra

In order to determine the variation of peak intensity with incident x-ray angle (I(θ), Equations 2.3, 3.3) I perform peak fitting on the final averaged spectra for each sample at each incident angle. The peak of interest corresponds to the transition dipole used to determine the molecular orientation; the area of this peak is used as I(θ). This peak and others near the edge step are fit to Gaussian peaks while the edge step is fit to Equation 6.1. The height, a and decay, γ of the edge are fit to the featureless area of the spectrum. The step location, dx, and width, σ of the edge step

are fit to area near the edge.. The height of this edge step is used to normalize the peak area to eliminate normalization artifacts from the background subtraction. Figure 6.4 shows an example peak fit.

$$\text{Edge step (x)} = \boldsymbol{a} * \left(\mathbf{0.5} + \frac{\boldsymbol{2arctan(x-dx)}}{\boldsymbol{\pi * \sigma}}\right) * \begin{Bmatrix} \mathbf{1} \mid \boldsymbol{x \leq dx + \sigma} \\ \boldsymbol{e^{-\gamma(x-dx-\sigma)}} \mid \boldsymbol{x > dx + \sigma} \end{Bmatrix} \quad [6.1]$$

6.10 XPS (Erin Ratcliffe, University of Arizona)

The near-surface composition of the IZO was evaluated using X-ray photoelectron spectroscopy (XPS). XPS studies were performed using a Kratos Axis Ultra photoelectron spectrometer operating at a base pressure of 10^{-9} Torr with a monochromatic Al Kα source at 1486.6 eV. The analyzer was operated at 20 eV pass energy and at a step width of 0.1 eV. The kinetic energy scale of the spectrometer was corrected for non-linearity of the spectrometer according to a previously reported method by Powell.[10] Results on IZO were obtained at high take-off angles (~60°) using substrates identical to those used for PM-IRRAS studies (i.e. ~5-10 nm IZO thin films sputtered onto Au substrates); this approach increases the surface sensitivity of the XPS measurement over a normal 0° take-off angle. XPS results on these substrates are comparable to those obtained using a similar high take-off angle on bulk IZO on glass substrates.

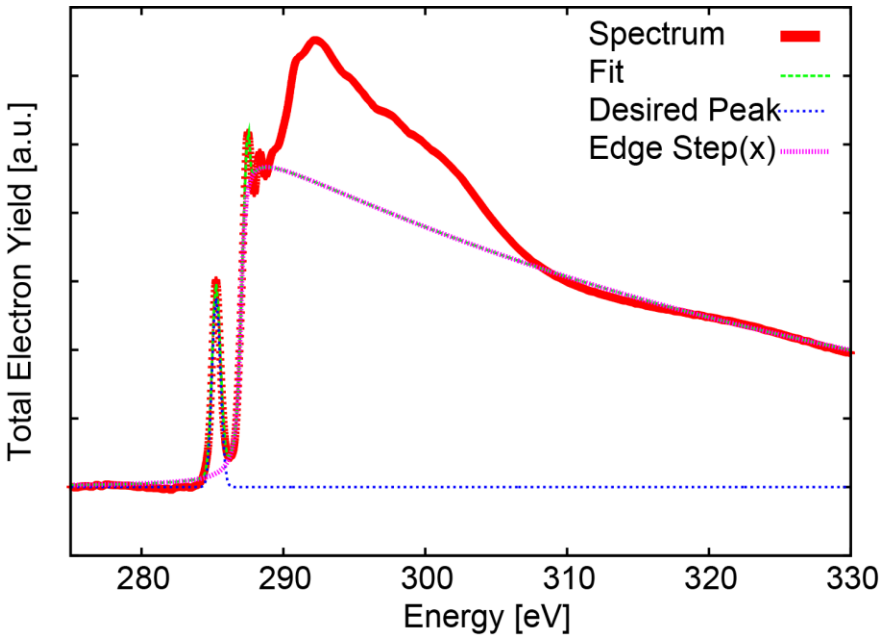

Figure 6.4. Example peak fit of F_3PPA, deposited using the 48 hour, room temperature soak at incident x-ray engle of 45°.

6.11 PM-IRRAS (Lingzi Sang and Matthew Schalnat, University of Arizona)

A Nicolet Nexus 670 Fourier transform infrared (FTIR) spectrometer coupled to a tabletop optical module was used to record PM-IRRAS. Polarization modulation (PM) in this instrument was provided by a Hinds Instruments (Hillsboro, OR) PM-90 with a 50 kHz ZnSe optical head and a synchronous sampling demodulator (GWC Instruments, Madison, WI). Detection was accomplished with a MCT-A detector (Thermo Electron Scientific Instrument Corp., Beverly, MA). Samples were positioned to accommodate an 80^{o} angle for incident and reflected radiation; spectra were acquired by averaging 4096 scans at 4 cm^{-1} resolution with spectra acquired in two discrete data sets with maximum dephasing at either 2900 or 1300 cm^{-1} in an effort to minimize PM error across the spectrum. Reference spectra were acquired (at identical sample placement) on samples that were identically cleaned and placed into neat ethanol for the same soaking

period. Baseline-corrected PM-IRRAS spectra were obtained according to practice previously established in the literature by normalization to the reference spectrum.[11-15] Once corrected for baseline, PM-IRRAS spectra are given by,[13,14]

$$\left[\frac{\Delta R}{R}\right]_{norm} = 1 + \frac{2\gamma\rho}{1-\gamma^2\rho^2} A \qquad [6.2]$$

where $[\Delta R/R]_{norm}$ is the baseline-correct PM-IRRAS signal, A is the absorbance, γ is the ratio of overall optoelectronic response for p- and s-polarizations, and ρ is ratio of the reflectivity values of p- and s-polarizations for a reference system of known thickness. For a typical monolayer sample on a metal substrate at grazing angle,[14] γ was determined to be 1 and ρ was determined to be 0.95 at both 2900 and 1000 cm^{-1} on our instrument. Thus, absorbance values were determined from Equation 6.3:[13,14]

$$A = 0.0223\left[\left(\frac{\Delta R}{R}\right)_{norm} - 1\right] \qquad [6.3]$$

Band fitting was performed with 100% Gaussian line shapes. Spectral fits were accepted for χ^2 values > 0.99. Transmission spectra of KBr pellets of the neat and dibasic sodium salts of the PAs were acquired on a Nicolet Magna 550 Series II FTIR spectrometer equipped with a MCT-A detector. Acquired spectra were averaged over 512 scans at 4 cm^{-1} resolution.

Key peak frequencies and assignments for neat PPA, PPA^-, PPA^{2-}, and PPA-modified IZO are given in Table 6.1. PPA binding mode and orientations derived from these spectra are discussed in the main text. Phenyl ring vibrational modes with transition dipole moment vectors are illustrated in Figure 6.5.

In order to determine average molecular orientation within the modifier layer, the experimental IR reflectance-absorbance spectrum calculated by conversion of the baseline-corrected PM-IRRAS data must be compared to a spectrum that is calculated for an isotropic film of comparable thickness. This calculation requires knowledge of the optical constants n and k at the relevant frequencies for the molecule of interest or a suitable model. Based on the noted similarities between the spectra of metal phosphonates, PPA^{2-} salts, and PPA on oxide surfaces, the spectrum of PPA^{2-} is chosen to be an appropriate model for the surface-bound PPA molecules. The transmission IR spectrum of PPA^{2-} provides a simple means of approximating the imaginary part of the refractive index, k(ν), at the relevant frequencies. The magnitude of the IR transmission is related to k(ν) through:

$$\frac{I}{I_o} = e^{-4\pi k(\nu)d\nu} \qquad [6.4]$$

where I/I_o is the fraction of power transmitted through the sample, d is the path length, ν is the frequency in cm^{-1}, and k*(ν)* is the extinction coefficient.[16-18] From estimates of k(ν) determined in this way, the corresponding n(ν) values are calculated by a Kramers-Kronig (KK) transformation using Maclaurin's formula:[19]

$$n(\nu_i) = n_\infty + \frac{2}{\pi}\int_{\nu 1}^{\nu 2} \frac{\nu\, k(\nu)}{(\nu^2 - \nu_i{}^2)} d\nu \qquad [6.5]$$

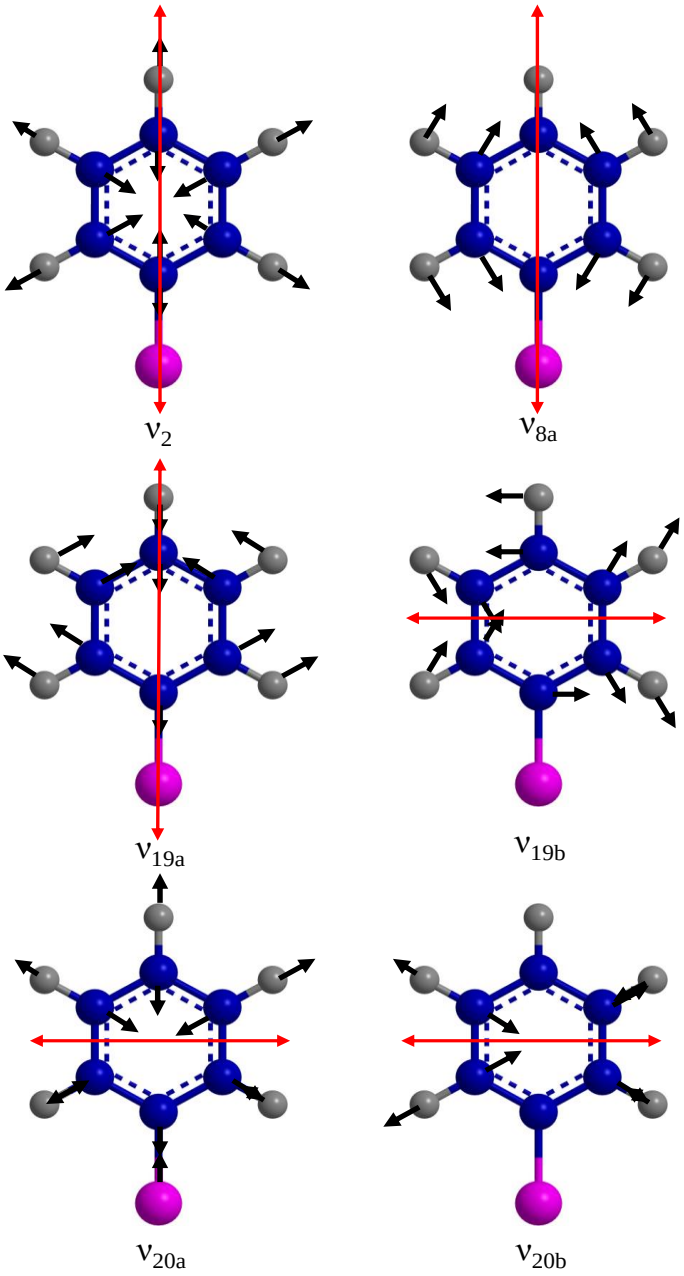

Figure 6.5 Illustration of phenyl ring vibrational modes and transition dipole moment vectors (red arrows) used to determine orientation of PPA on IZO.

Table 6.1. Peak frequencies and assignments for PPA, PPA^{-}, PPA^{2-}, and PPA-modified IZO.

Peak Frequency (cm^{-1})				Assignments
PPA	PPA^{1-}	PPA^{2-}	PPA-modified IZO	
925	926			ν_s (P-OH)[20]
940	942			ν_s (P-OH)[20]
999	998	997	997	ν_{12} β(C-C-C)$_{ip}$[21]
1017	1019	1021	1016	$\nu_s(PO_3^{2-})$[20]
			1040	$\nu_{as}(PO_3^{2-})$[22]
			1069	$\nu_{as}(PO_3^{2-})$[22]
1081				ν(P-O) in PO_3H_2 [20]
1146	1145	1140	1148	$\nu(C_{ring}\text{-}P)$ [23,24] $\delta(ring)_{ip}$ [23,24]
	1167	1164	1166	ν(P-O-metal)[25,26] $\nu(C_6H_5\text{-}P)$[25,26]
		1198	1197	ν(P=O)[27]
1222	1226	1230 1260		ν(P=O)[20]
1316 1337	1315 1334	1309 1331		ν_{14} ν(C-C)[21]
1439	1438	1437	1436	ν_{19b} ν(C-C)[21]
1487	1486	1486	1491	ν_{19a} ν(C-C)[21]
1592	1593	1594	1595	ν_{8a} ν(C-C)[21]
3016	3014	3013	3031	ν_{20b} ν(C-H)[21]
3055	3055	3055	3061	ν_2 ν(C-H)[28]
3083	3081	3075		ν_{20a} ν(C-H)[21]

Here, ν_I represents the i^{th} point in the frequency set over the range from ν_1 to ν_2, and n_∞ is the value of $n(\nu)$ far below the electronic absorption and far above the infrared absorption. The

initial set of n(ν) values determined in this way is then used in a more rigorous calculation of a theoretical transmission spectrum, which provides significantly improved k(ν) values. We then proceed iteratively, obtaining more accurate values of n(ν) and k(ν) values using similar calculations to convergence.

6.12 Determination of pK_a for PPA and F_3PPA (Anthony J. Giordano, Georgia Institute of Technology)

Titrations of the acids were conducted in a manner similar to that reported previously for PPA.[29] The pK_a of PPA has been measured several times in the literature,[29-32] and this particular method was chosen due to the use of a solvent mixture containing a high ethanol content, which is similar to the conditions used for the modification of our ITO substrates. All titrations were performed at an ambient temperature of 20 °C and made with a Thermo Orion 420A+ pH meter equipped with a VWR sympHony glass electrode (filled with saturated solutions of KCl in either deionized water or methanol) calibrated against pH 4, 7, and 10 buffer solutions (Hach Company). A standardized solution of 0.10 M NaOH in a mixture of 75:25 ethanol:water (v:v) served as the titrant. Solutions of the phosphonic acid for titration were dissolved in the same ethanol:water mixture at a concentration of 0.01 M. All solutions were degassed by sparging with nitrogen prior to use and all titrations were performed under a flow of nitrogen.

6.13 Resonant spectroscopy experimental setup

Total electron yield (TEY) NEXAFS spectra were recorded at grazing (20°) angle of x-ray incidence at beamline 10-1 at the Stanford Synchrotron Radiation Lightsource (SSRL) with a linear polarization of approximately 80%. All spectra were normalized by dividing by a freshly

coated gold mesh flux monitor. The sample drain current and the gold-grid current were measured simultaneously with Keithley 428 current amplifiers. A titanium oxide film (strongly absorbing photons with energies above the Ti L-edge at 454 eV and O K-edge at 530 eV) was employed to suppress second order light passed by the monochromator. The lower energy dip in the gold-grid absorption spectrum (corresponding to the residual carbon on the optics in the beamline and assumed to be constant) was used to align all spectra to the same absolute energy calibration during individual runs. All resonant Auger spectra and NEXAFS measurements were conducted at base pressures below 1x10-8 Torr. For resonant Auger spectra, the CMA was set to a pass energy of 25 eV yielding an energy resolution of 250 meV. The monochromator was optimized for maximum flux at this energy resolution. The beam spot size was approximately 1.5 mm x 1 mm. In order to avoid beam damage, several spots, chosen at least 4mm apart were used. TEY NEXAFS spectra were taken before and after resonant Auger spectra on each spot to confirm both the uniformity of the sample and that no beam damage had occurred.

6.14 Processing resonant Auger data

The resonant Auger data consists of energy spectra of emitted electrons taken at several x-ray energies. A NEXAFS spectrum of the sample is used as a road map. The photoemission spectrum is taken at an x-ray energy about 10-20 eV below the onset of the first NEXAFS peak. This photoemission spectra captures the valence features, which occur at constant binding energy. An Auger and photoemission spectrum is taken at x-ray energy of about 50 eV past the final NEXAFS feature. This spectrum contains the Auger feature which is compared with Auger emission in the resonance spectra. Resonant spectra can then be taken at any x-ray energy corresponding to the resonances near the atomic absorption edge in the NEXAFS spectrum. The

position of the photoemission feature should vary as binding energy + x-ray energy. Even if suppressed, some second-order light from the monochromator will reach the sample and excite 1s electrons. The position of the second-order feature varies as binding energy + 2*(x-ray energy). In each resonant spectrum, the position of the photoemission features and second-order features can be used in tandem to ensure that no monochromator drift, CMA drift or sample charging is present. If monochromator drift is present, both features will be shifted with the second-order feature shifted by twice as much as the photoemission. Sample charging or CMA drift will result in equal shifts of the two features.

After the photoemission and second-order features are examined, I can be confident in the absolute kinetic energy scale of the resonant spectra. I can then compare the location of the Auger feature in the resonant spectra with that in the off-resonance Auger spectrum. The difference in location is deemed as the spectator shift. There are two ways to determine the spectator shift: fitting and feature alignment. First, the non-resonant spectra can be fitted using a shift and a scaling factor to the resonant spectra to extract the spectator shift. In this method, if an Auger-spectator branching ratio is suspected the resonant spectra can be fitted to the sum of an unshifted and a shifted Auger spectrum, with the ratio between their scaling factors related to the timescale of a charge transfer process as discussed in chapter 1.6. If no branching ratio is suspected, than the simplest way to get the spectator shift is by comparing the location of the Auger dip. Since the peaks in the Auger are typically broad, they are hard to compare. In the C and N Auger KLL features, there tends to be a sharp dip in between two broad peaks, which is straightforward to locate and determine the spectator shift.

6.15 Density functional theory I: phosphonic acid orientation (Hong Li, Georgia Institute of Technology)

Density functional theory calculations were carried out to optimize the adsorption geometry of PPA molecules on a conducting oxide surface. We have evidence suggesting IZO is amorphous (See Appendix A), which presents a challenge with respect to our use of slab calculations (see below). Therefore, for the purposes of computation we consider PPA bound to a model ITO surface. We anticipate similar binding geometries on both oxides. This is based on the fact that Sn:In ratio in the commercial ITO is on the order of 0.1~0.2, whereas the Zn:In ratio in our IZO samples is ~0.24. Therefore, in both cases, the major interaction between the PPA molecules and the substrate is via the surface In atoms, which are common to both ITO and IZO. The theoretical model of the bare ITO surface consisted of a slab of three (In/Sn-O) layers, where the top layer was passivated by hydroxyl groups.[33] Geometry optimizations were performed for all ITO/PA interface systems composed of a slab of ITO and a monolayer of PPA or F_3PPA molecules at two coverage densities, 2.8×10^{13} molecules/cm^2 equivalent to one PA molecule per surface unit cell, and 1.1×10^{14} molecules/cm^2, equivalent to four PA molecules per unit cell.

To clarify the contribution of the fluorinated PPA molecules on the surface modification with respect to the nonfluorinated ones, the perpendicular component of the dipole moment of each PA monolayer was calculated. These calculations were performed on unbound PA molecules, with the geometry of each PA monolayer fixed at its surface-adsorbed geometry. Self-consistent total energy calculations with dipole-sheet corrections were then carried out for each PA monolayer. The calculations were performed with the Vienna Ab Initio Simulation Package (VASP)[34,35] code using plane wave basis sets and the projector-augmented wave (PAW)[36] method. The generalized gradient approximation (GGA) PBE exchange-correlation functional[37]

was employed. A plane-wave energy cutoff of 300 eV and a total energy convergence of 10^{-6} eV were used in the self-consistent total-energy calculations. For geometry optimizations, the coordinates of all the optimized atoms were relaxed until the forces were lower than 0.04 eV/Å using a damped molecular dynamics scheme.

6.16 Density functional theory II: polymer orbitals and energy levels (Dane W. de Quilettes and Phu Nguyen, University of Washington)

All DFT calculations were performed using the development version of Gaussian software suite.[38] Ground-state energies and electronic structures of alternating n = 1-4 monomer units were obtained by solving the Kohn-Sham equations self-consistently using the B3LYP exchange correlation functional and 6-31G(d) basis set.[39-41] Subsequent frequency calculations were performed to verify the minima of the potential energy surface. Vertical excitations from the core 1s orbitals of the N atoms in each PCPDTBT and PCDTBT molecule and characteristics of these excited states were calculated using the well-established energy-specific linear response formalisms of TD-DFT as implemented in Gaussian.[42]

6.17 References

1. Bravo-Altamirano, K.; Montchamp, J.-L., A Novel Approach to Phosphonic Acids from Hypophosphorous Acid. *Tetrahedron Lett.* **2007,** *48,* 5755-5759.

2. Schulmeyer, T.; Paniagua, S. A.; Veneman, P. A.; Jones, S. C.; Hotchkiss, P. J.; Mudalige, A.; Pemberton, J. E.; Marder, S. R.; Armstrong, N. R., Modification of BaTiO3 Thin Films: Adjustment of the Effective Surface Work Function. *J. Mater. Chem.* **2007,** *17,* 4563-4570.

3. Hotchkiss, P. J.; Li, H.; Paramonov, P. B.; Paniagua, S. A.; Jones, S. C.; Armstrong, N. R.; Bredas, J. L.; Marder, S. R., Modification of the Surface Properties of Indium Tin Oxide with Benzylphosphonic Acids: A Joint Experimental and Theoretical Study. *Adv.Mater.* **2009,** *21,* 4496-4501.

4. Knesting, K. M.; Hotchkiss, P. J.; MacLeod, B. A.; Marder, S. R.; Ginger, D. S. Spatially Modulating Interfacial Properties of Transparent Conductive Oxides: Patterning Work Function with Phosphonic Acid Self-Assembled Monolayers. *Adv. Mater.* **2012**, *24*, 642-646.

5. Tirsell, K. G.; Karpenko, V. P. A General-Purpose Sub-Kev X-Ray Facility at the Stanford-Synchrotron-Radiation-Laboratory. *Nucl. Instrum. Meth. A.* **1990**, *291*, 511-517.

6. Batson, P. E. Carbon-1s Near-Edge-Absorption Fine-Structure in Graphite. *Phys. Rev. B* **1993**, *48*, 2608-2610.

7. Willey, T. M.; Lee, J. R. I.; Fabbri, J. D.; Wang, D.; Nielsen, M. H.; Randel, J. C.; Schreiner, P. R.; Fokin, A. A.; Tkachenko, B. A.; Fokina, N. A.; et al. Determining Orientational Structure of Diamondoid Thiols Attached to Silver Using Near-Edge X-ray absorption Fine Structure Spectroscopy. *J. Electron Spectrosc.* **2009**, *172*, 69-77.

8. Stöhr, J. *NEXAFS spectroscopy*; Springer-Verlag: Berlin, 1992.

9. Genzer, J.; Kramer, E. J.; Fischer, D. A. Accounting for Auger Yield Energy Loss for Improved Determination of Molecular Orientation Using Soft X-ray Absorption Spectroscopy. *J. Appl. Phys.* **2002**, *92*, 7070-7079.

10. Powell, C. J. Energy Calibration of X-ray Photoelectron Spectrometers: Results of an Interlaboratory Comparison to Evaluate a Proposed Calibration Procedure. *Surf. Interface Anal.***1995,** *23*, 121-132.

11. Frey, B.L.; Corn, R.M.; Weibel, S.C. In *Handbook of Vibrational Spectroscopy,* Vol. 2; Chalmers, J.M.; Griffiths, P.R., Eds.; John Wiley: United Kingdom, 2001; pp. 1042-1056.

12. Barner, B. J.; Green, M. J.; Saez, E. I; Corn, R. M. Polarization Modulation Fourier Transform Infrared Reflectance Measurements of Thin Films and Monolayers at Metal Surfaces Utilizing Real-Time Sampling Electronic. *Anal. Chem.*, **1991**, *63*, 55-60.

13. Buffeteau, T.; Desbat, B.; Turlet, J. M., Polarization Modulation FT-IR Spectroscopy of Surfaces and Ultra-thin Films: Experimental Procedure and Quantitative Analysis. *Appl. Spectrosc.* **1991**, *45*, 380-389.

14. Bradley, M.S. A New Approach to Quantitative Spectral Conversion of PM-IRRAS: Theory, Experiments and Performance Comparisons with Conventional IRRAS. Application Note: 51368, ThermoFisher Scientific: Madison, WI, 2008.

15. Buffeteau, T.; Desbat, B.; Blaudez, D.; Turlet, J.M. Calibration Procedure to Derive IRRAS Spectra from PM-IRRAS Spectra. *Appl. Spectrosc.* **2000**, *54*, 1646-1650.

16. Hansen, W. N. Electric Fields Produced by the Propagation of Plane Coherent Electromagnetic Radiation in a Stratified Medium. *J. Opt. Soc. Am.* **1968**, *58*, 380-388.

17. McIntyre, J. D. E.; Aspnes, D. E. Differential reflection spectroscopy of very thin surface films. *Surf. Sci.* **1971**, *24*, 417-434.

18. Allara, D. L.; Baca, A. Distortions of Band Shapes in External Reflection Infrared Spectra of Thin Polymer Films on Metal Substrates. *Macromolecules* **1978**, *11*, 1215-1220.

19. Ohta, K.; Ishida, H. Comparison Among Several Numerical Integration Methods for Kramers-Kronig Transformation. *Appl. Spectrosc.* **1988**, *42*, 952-957.

20. Yagyu, S.; Yoshitake, M.; Tsud, N.; Chikyow, T. Adsorption Structure of Phenylphosphonic Acid on an Alumina Surface. *Appl. Surf. Sci.* **2009,** *256*, 1140-1143.

21. Joo, T. H.; Kim, M. S.; Kim, K. Surface-enhanced Raman scattering of Benzenethiol in Silver Sol. *J. Raman Spectrosc.* **1987,** *18*, 57-60.

22. Ohno, K.; Mandai, Y.; Matsuura, H. Vibrational Spectra and Molecular Conformation of Ciliatine. *J. Mol. Struct.* **1993,** *298*, 1-11.

23. Forner, W.; Badawi, H. M. Vibrational Spectra of Phenylphosphonic and Phenylthiophosphonic Acid and Their Complete Assignment. *Z. Naturforsch.* **2010,** *65b*, 357-366.

24. Forner, W.; Badawi, H. M. Study of Vibrational Spectra and Their Assignments for Phenylphosphonic Acid and Phenylthiophosphonic Acid and Comparison to Experiments. *J. Struct. Chem.* **2011,** *52*, 471-479.

25. Guerrero, G.; Mutin, P. H.; Vioux, A. Anchoring of Phosphonate and Phosphinate Coupling Molecules on Titania Particles. *Chem. Mater.* **2001,** *13*, 4367-4373.

26. Koh, S. E.; McDonald, K. D.; Holt, D. H.; Dulcey, C. S.; Chaney, J. A.; Pehrsson, P. E. Phenylphosphonic Acid Functionalization of Indium Tin Oxide: Surface Chemistry and Work Functions. *Langmuir* **2006,** *22*, 6249-6255.

27. Botelho do Rego, A. M.; Ferraria, A. M.; El Beghdadi, J.; Debontridder, F.; Brogueira, P.; Naaman, R.; Rei Vilar, M. Adsorption of Phenylphosphonic Acid on GaAs (100) Surfaces. *Langmuir* **2005,** *21*, 8765-8773.

28. Rajalingam, K.; Hallmann, L.; Strunskus, T.; Bashir, A.; Woll, C.; Tuczek, F. Self-Assembled Monolayers of Benzylmercaptan and Para-cyanobenzylmercaptan on Gold: Surface Infrared Spectroscopic Characterization. *Phys. Chem. Chem. Phys.* **2010,** *12*, 4390-4399.

29. Peppard, D. F.; Mason, G. W.; Andrejasich, C. M., Variation of the pKA of (X)(Y)PO(OH) with X and Y in 75 and 95 per cent ethanol. *J. Inorg. Nucl. Chem.* **1965,** *27,* 697-709.

30. Franz, R. G., Comparisons of pKa and Log P Values of Some Carboxylic and Phosphonic Acids: Synthesis and Measurement. *AAPS Pharmsci.* **2001,** *3*, article 10.

31. Jaffé, H. H.; Freedman, L. D.; Doak, G. O., The Acid Dissociation Constants of Aromatic Phosphonic Acids. I. Meta and Para Substituted Compounds. *J. Am. Chem. Soc.* **1953,** *75*, 2209-2211.

32. Nagarajan, K.; Shelly, K. P.; Perkins, R. R.; Stewart, R., Arylphosphonic acids. I. Substituent effects on their First and Second Dissociations. *Can. J. Chem.* **1987,** *65*, 1729-1733.

33. Paramonov, P. B.; Paniagua, S. A.; Hotchkiss, P. J.; Jones, S. C.; Armstrong, N. R.; Marder, S. R.; Bredas, J.-L. Theoretical Characterization of the Indium Tin Oxide Surface and of Its Binding Sites for Adsorption of Phosphonic Acid Monolayers. *Chem. Mater.* **2008**, *20*, 5131-5133.

34. Kresse, G.; Furthmuller, J., Efficiency of Ab-Initio Total Energy Calculations for Metals and Semiconductors Using a Plane-Wave Basis Set. *Computational Materials Science* **1996,** *6*, 15-50.

35. Kresse, G.; Furthmuller, J., Efficient Iterative Schemes for Ab Initio Total-Energy Calculations Using a Plane-Wave Basis Set. *Phys. Rev. B.* **1996,** *54*, 11169-11186.

36. Blöchl, P. E., Projector Augmented Wave Method. *Phys. Rev. B.* **1994,** *50*, 17953-17979.

37. Perdew, J. P.; Burke, K.; Ernzerhof, M., Generalized Gradient Approximation Made Simple. *Phys. Rev. Lett.* **1996,** *77*, 3865-3868.

38. Frisch, M. J.; Trucks, G. W.; Schlegel, H. B.; Scuseria, G. E.; Robb, M. A.; Cheeseman, J. R.; Scalmani, G.; Barone, V.; Mennucci, B.; Petersson, G. A.; et al. Gaussian Development Version Revision H.13; Gaussian, Inc.: Wallingford, CT, **2010.**

39. Stephens, P. J.; Devlin, F. J.; Chabalowski, C. F.; Frisch, M. J., Ab Initio Calculation of Vibrational Absorption and Circular Dichroism Spectra Using Density Functional Force Fields. *J. Phys. Chem.* **1994**, *98*, 11623-11810

40. Becke, A. D., Density-Functional Thermochemistry. III. The Role of Exact Exchange. *J. Chem. Phys.* **1993**, *98*, 5468-5472.

41. Lee, C.; Yang, W.; Parr, R. G., Development of the Colle-Salvetti Correlation-Energy Formula into a Functional of the Electron Density. *Phys. Rev. B.* **1988**, *37*, 785-789.

42. W. Liang, S. A. Fischer, M. J. Frisch, X. Li, Energy-Specific Linear Response TDHF/TDDFT for Calculating High-Energy Excited States. *J. Chem. Theory Comput.*, **2011**, *7*, 3540-3547.

Appendix A: IZO Thin Film Fabrication and Characterization

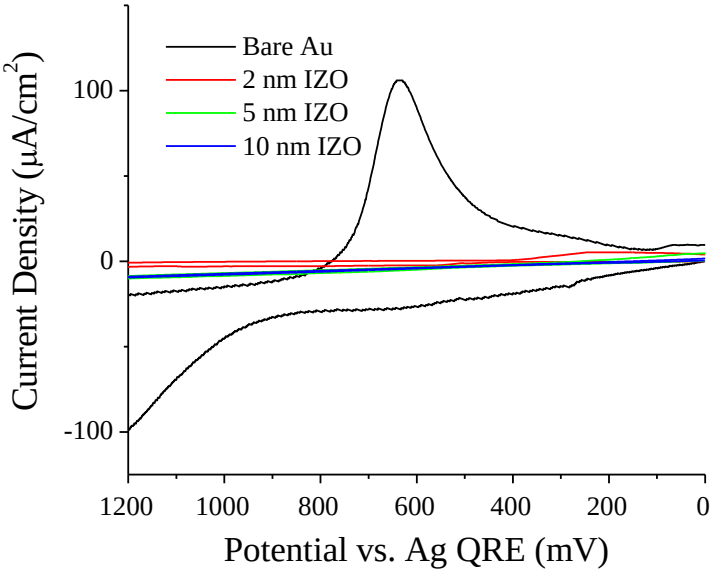

Figure A1. Cyclic voltammetry of oxidation of Au (black) and 2 (red), 5 (green), and 10 (blue) nm films of IZO on Au using 0.5 M K_2SO_4. Potential scan rate 50 mV/s.

Electrochemistry. Continuity of the thin IZO films on Au on glass was investigated using cyclic voltammetry. Samples were placed into a homemade Teflon electrochemical cell filled containing previously-degassed 0.500 M K_2SO_4 and cycled from 0 to +1.55 V versus a Ag wire quasi-reference electrode (QRE). Representative voltammograms for bare Au, and Au coated with IZO thin films of 2, 5, and 10 nm thicknesses are shown in Figure A1. These voltammograms demonstrate complete passivation of the underlying Au substrate at all IZO thicknesses based on the complete elimination of Au oxidation/reduction processes in the voltammetric response. This passivation is most easily recognized by the elimination of the Au oxide reduction wave at ~+0.60 V.

AFM. Conformity of these sputtered IZO films to the underlying Au-on-glass substrate was further confirmed with atomic force microscopy (AFM) on a Dimension 3100 (Nanoscope, Digitals Instruments, Santa Barbara, CA) instrument using tapping mode with ultrasharp tips (NSC15/no Al, MikroMasch, Wilsonville, OR) at a 1 Hz scan rate. AFM height images of bare Au substrates and Au substrates coated with IZO thin films of 2, 5, and 10 nm thicknesses are shown as Figure A2. Films were concluded to be conformal based on the similarity in appearance and RMS roughness values of the images of bare Au and the IZO-modified Au slides. RMS values of <2.0 nm were measured for all surfaces on a length scale of 3 μm. We believe the IZO on Au films are amorphous as they show no clear grain structure in AFM imaging, and produce conformal films as evidenced by the AFM (Figure A2) and electrochemistry results (Figure A1). AFM scans of the 100 nm thick IZO on glass substrates used in the NEXAFS experiments demonstrated roughness below the noise limit of our AFM (<0.5 nm RMS)

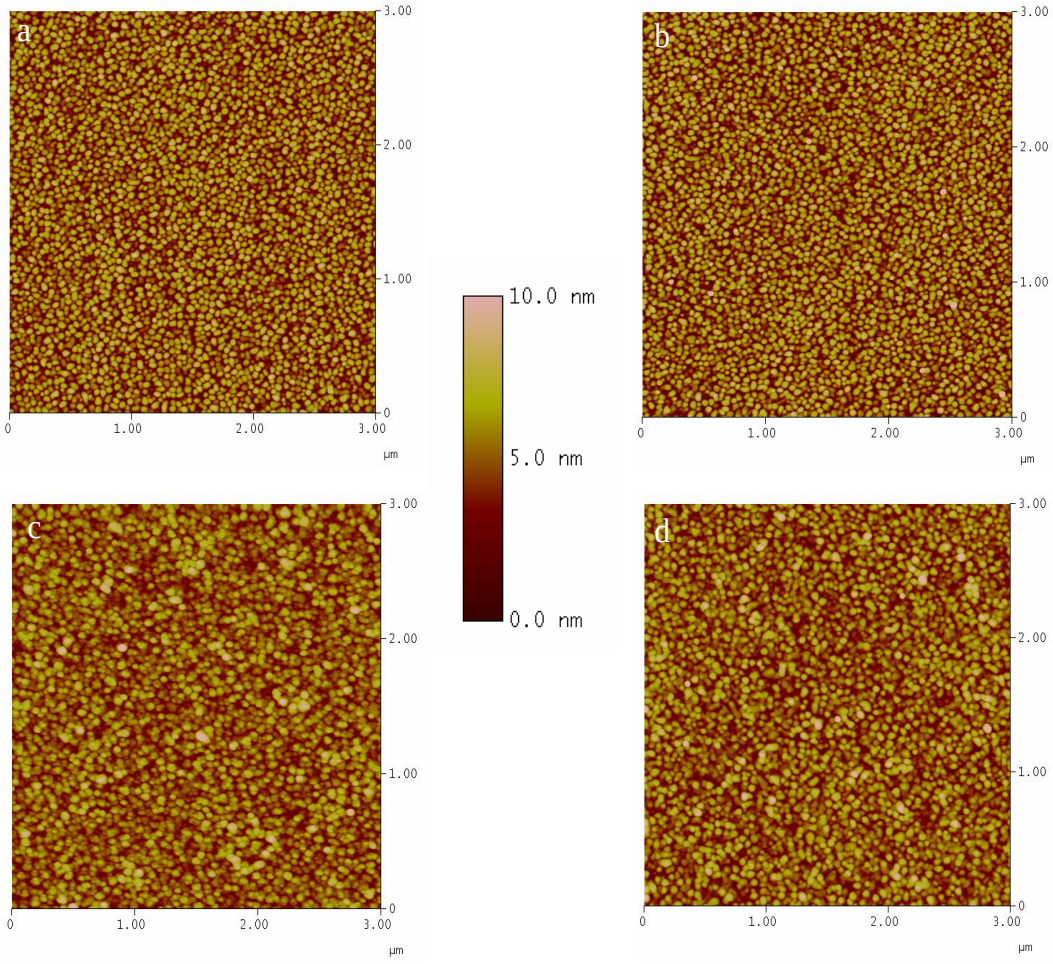

Figure A2. AFM tapping mode height images of a) bare Au, b) 2 nm IZO on Au, c) 5 nm IZO on Au, and d) 10 nm IZO on Au.

Appendix B: NEXAFS Spectra

The spectra in Figures B1-B20 are TEY spectra that have undergone the data processing described in the experimental section. For display purposes, these spectra have been roughly normalized using the automatic background subtraction routine autobks in Athena (http://dx.doi.org/10.1107/S0909049505012719, B. Ravel and M. Newville, *J. Synchrotron Rad.* **12**, pp 537--541 (2005)). In order to measure angular dependence, we decompose these spectra into a sum of Gaussian peaks and an edge step using our own custom software as discussed in the methodology section. The peak areas are then normalized using the height of the edge step during the peak fitting process.

Figures B1-B20. Processed TEY Spectra

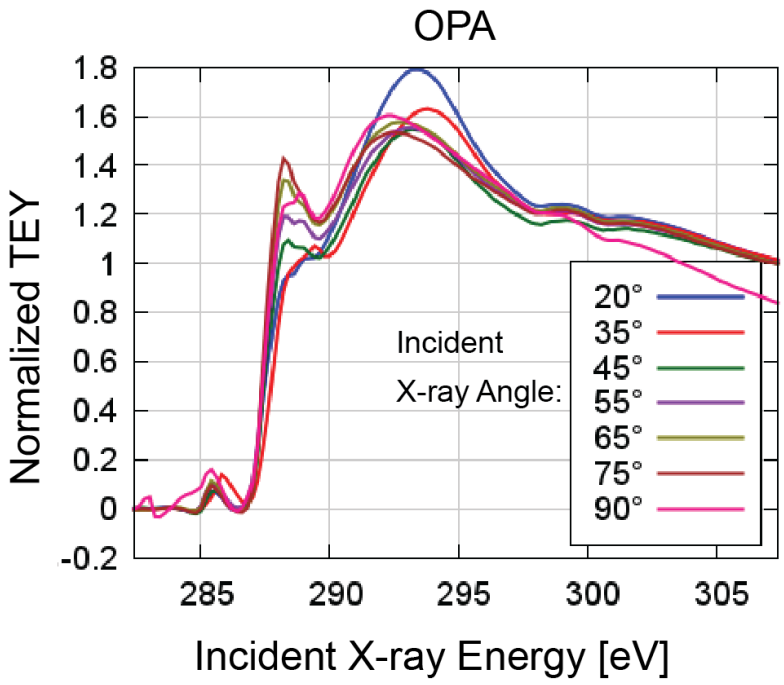

FigureB1.

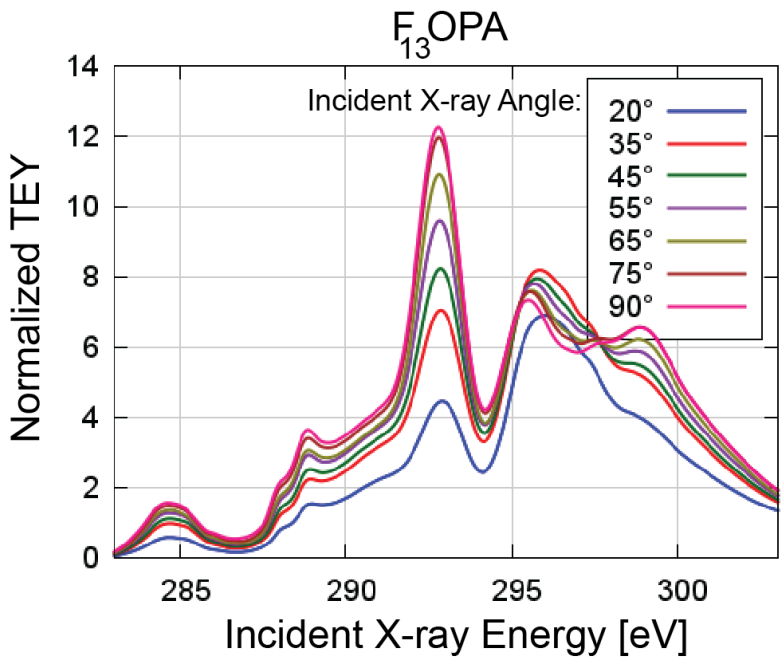

FigureB2.

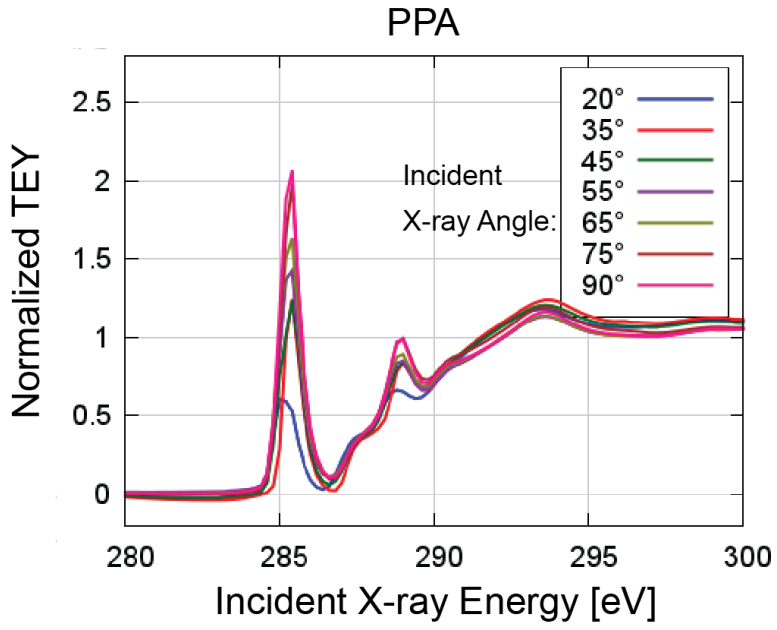

Figure B3.

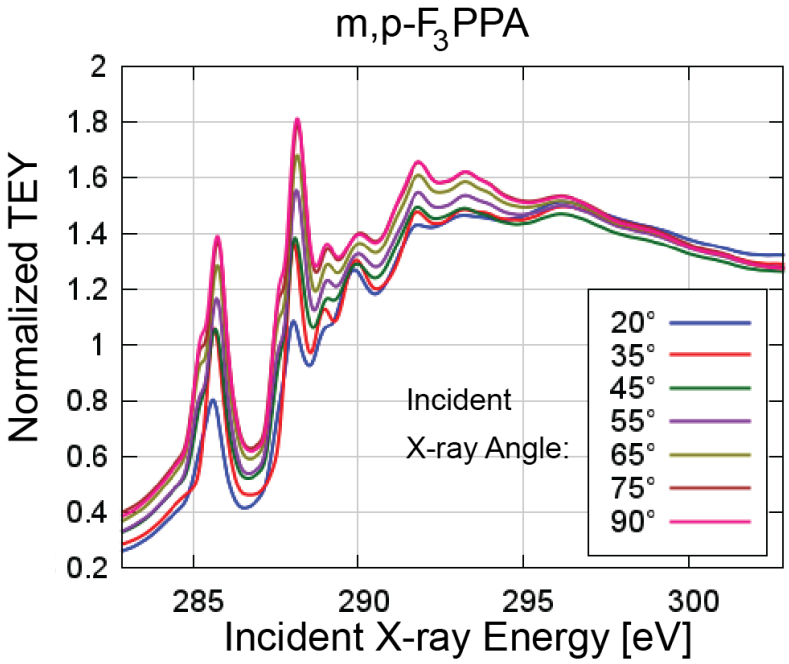

Figure B4

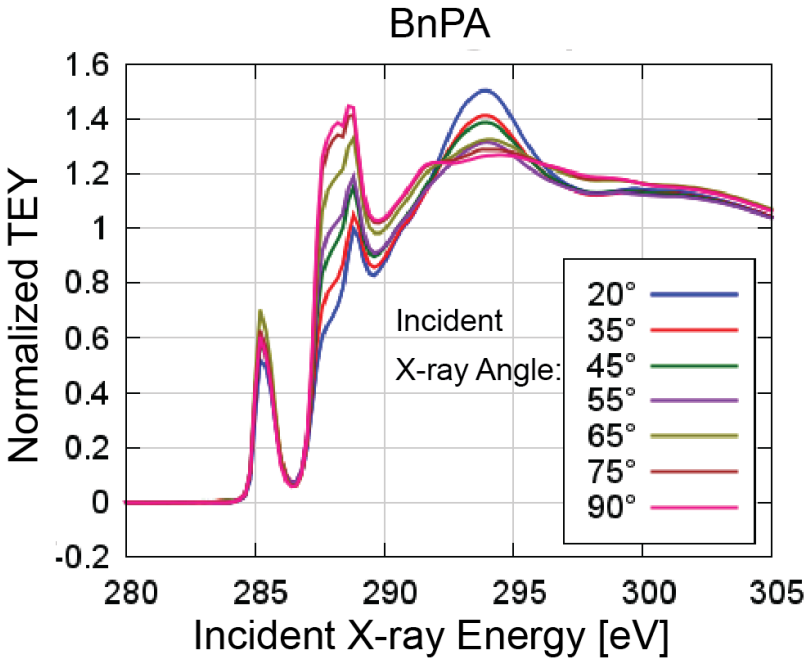

.

Figure B5.

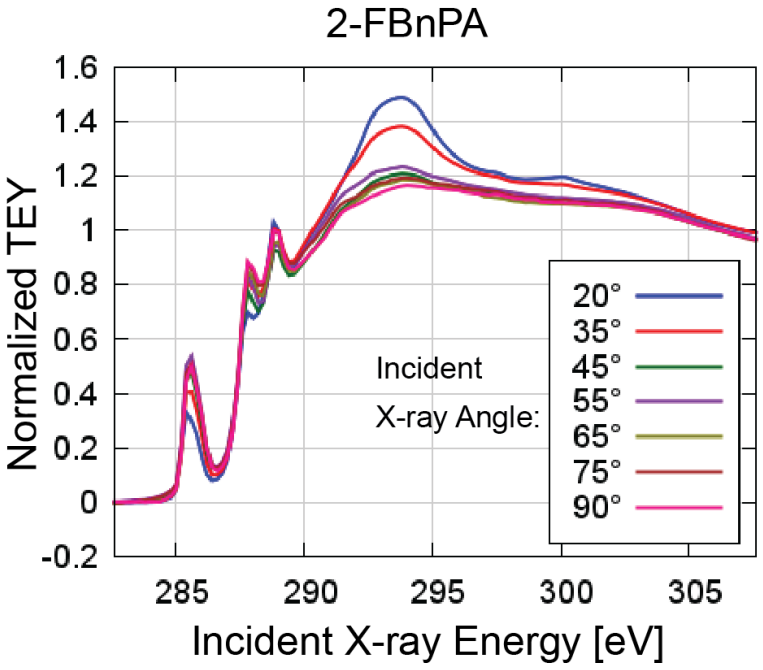

Figure B6.

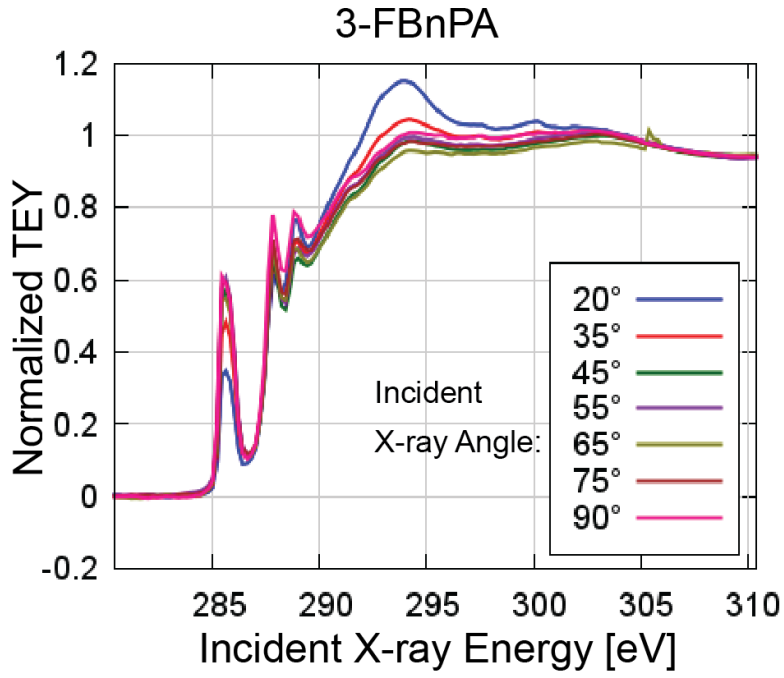

Figure B7.

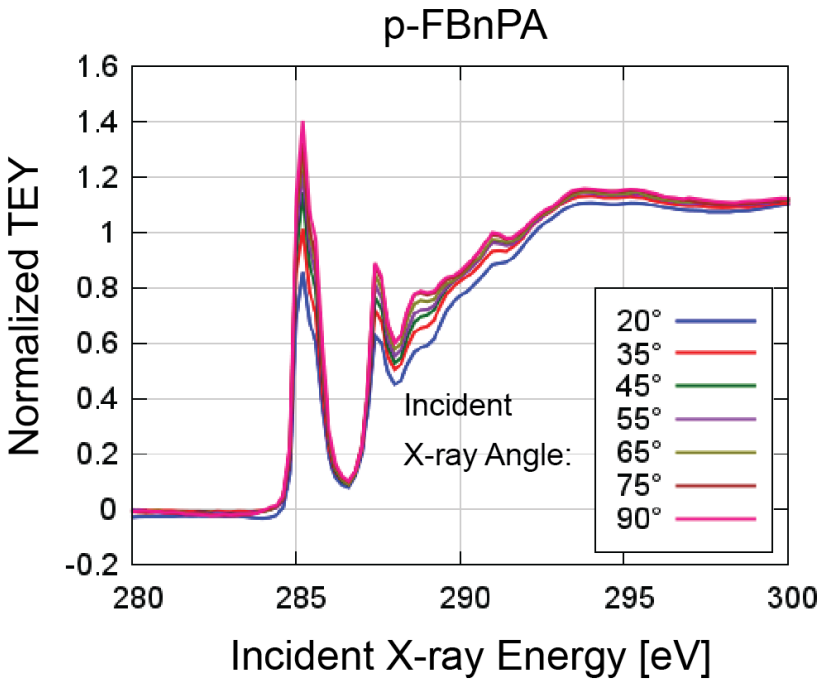

Figure B8.

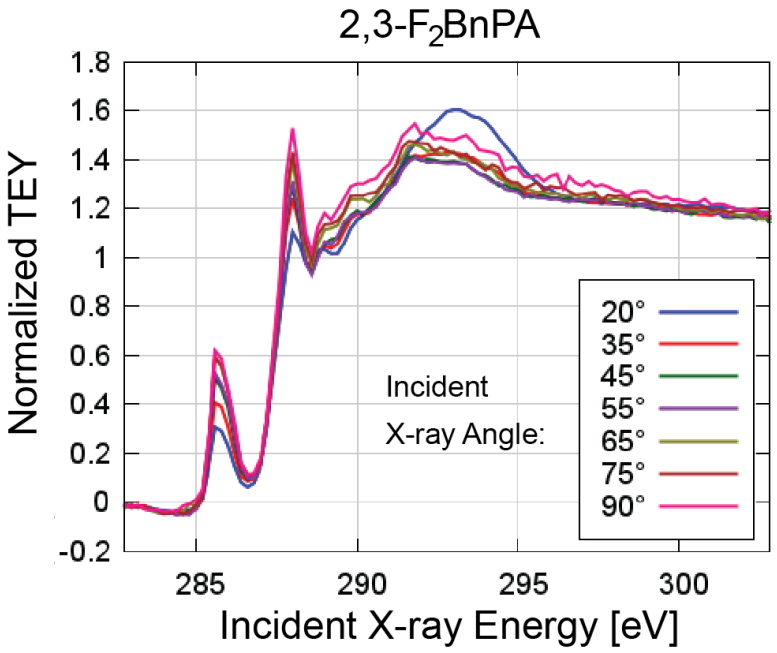

Figure B9.

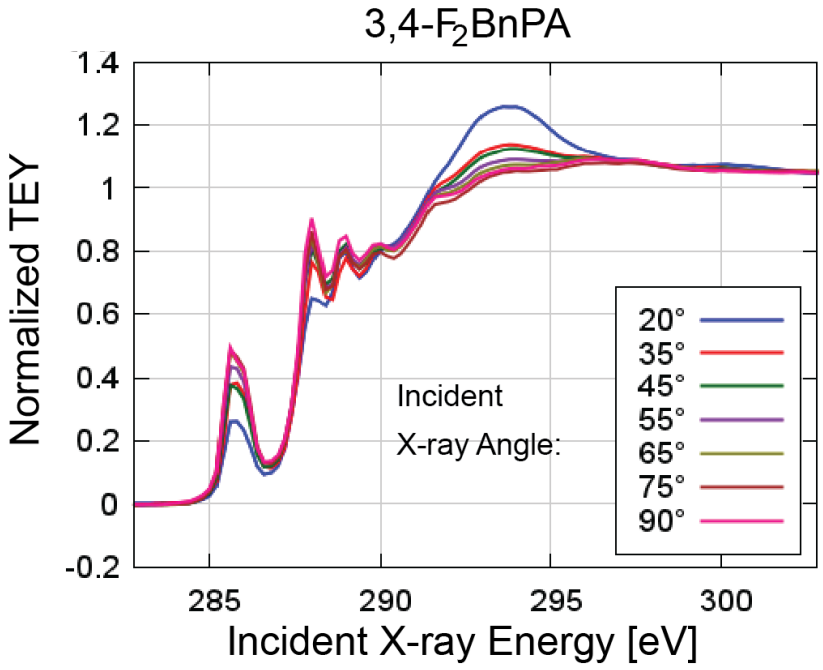

Figure B10.

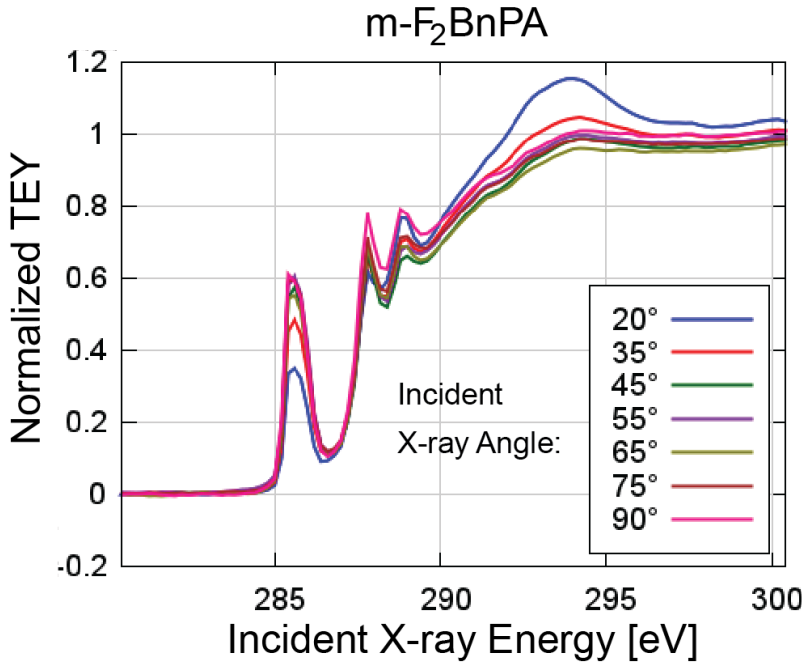

Figure B11.

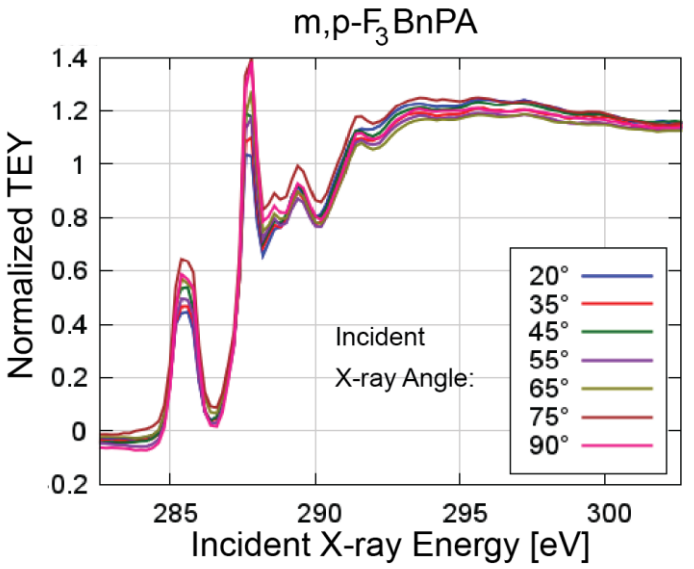

Figure B12.

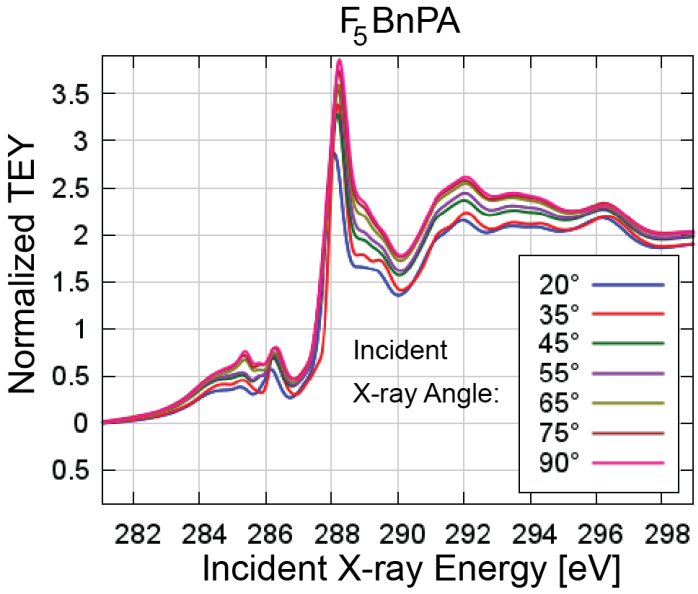

Figure B13.

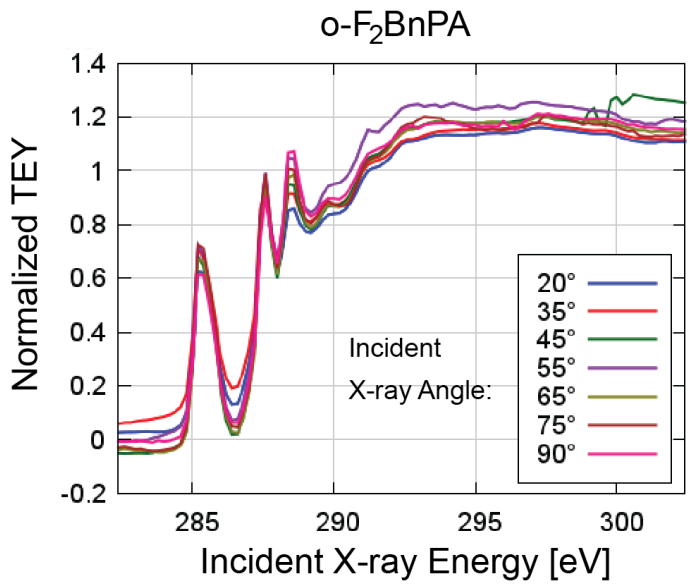

Figure B14.

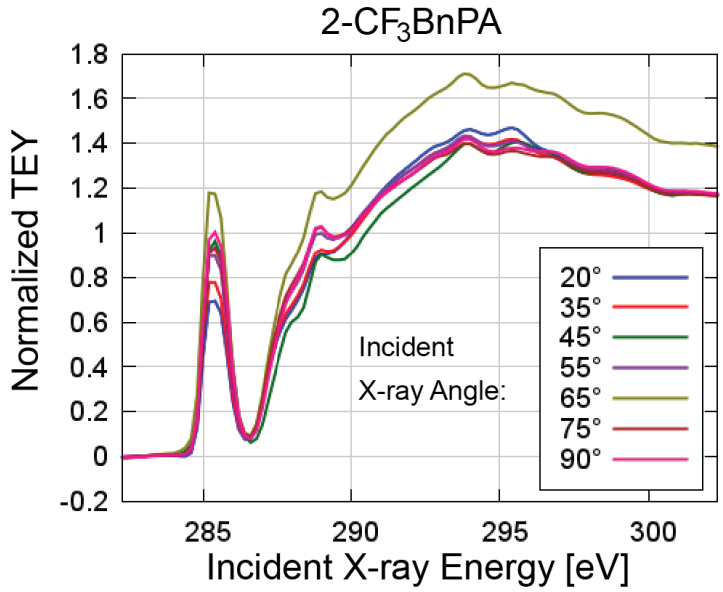

Figure B15.

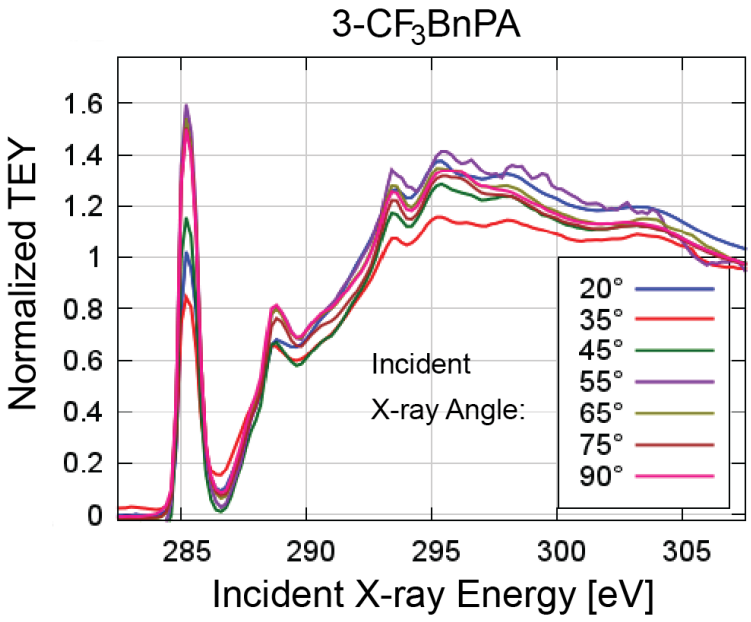

Figure B16.

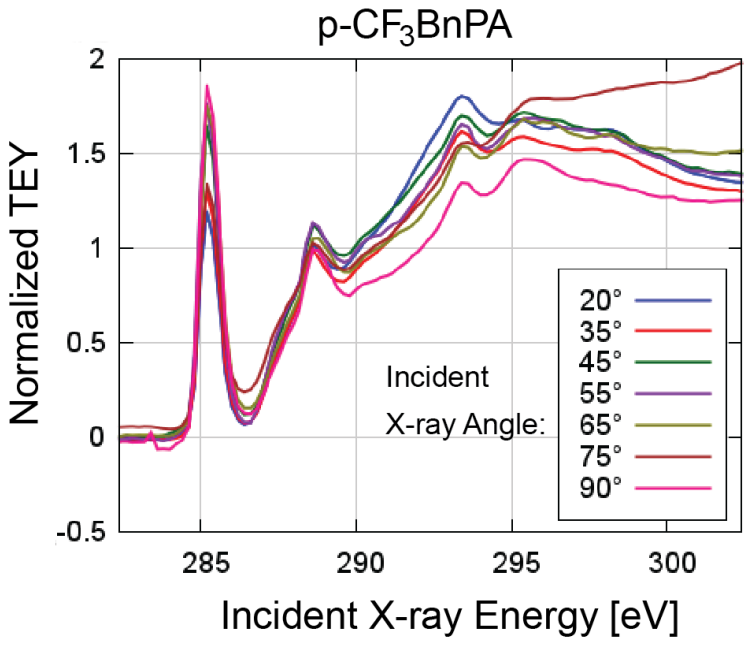

Figure B17.

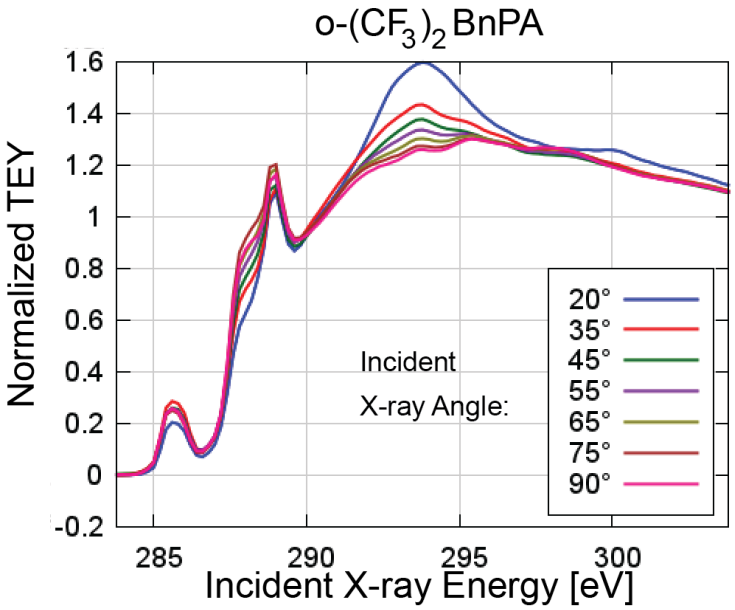

Figure B18.

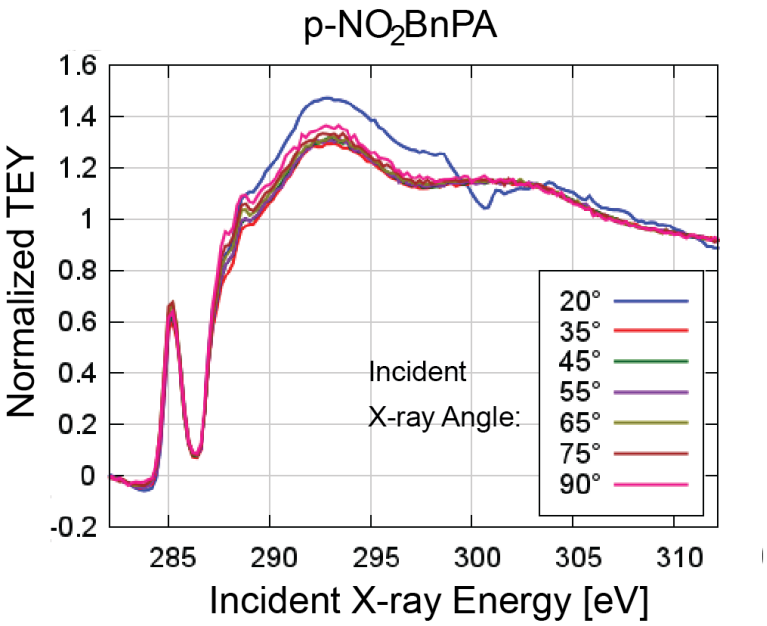

Figure B19.

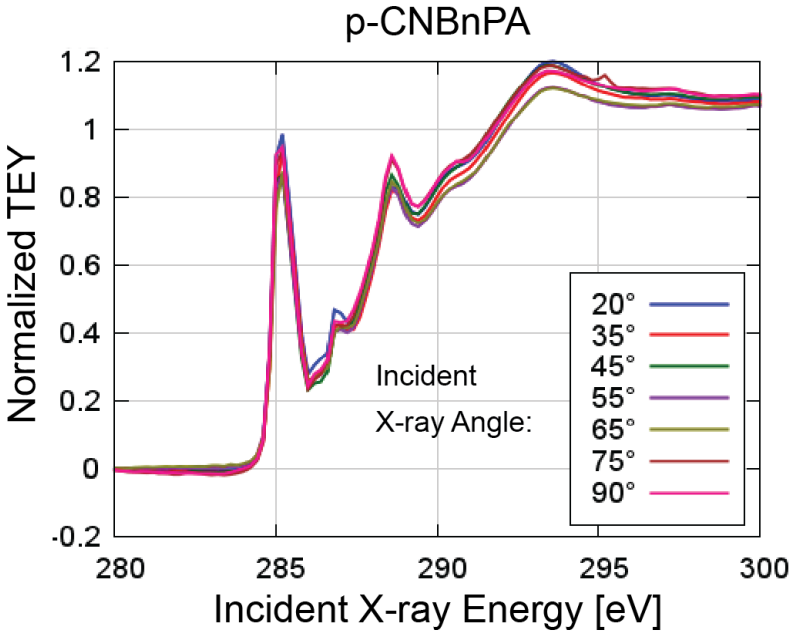
p-CNBnPA
Normalized TEY
1.2
1
0.8
0.6
0.4
0.2
0
-0.2
280
285
290
295
300
Incident X-ray Energy [eV]
Incident
X-ray Angle:
20°
35°
45°
55°
65°
75°
90°

Figure B20.

Appendix C: Publications and Curriculum Vitae

Education

2013 PhD: Department of Physics, University of Washington.
Thesis Advisor: David Ginger.

2009 B.S.E: Interdisciplinary Engineering, The Cooper Union for the Advancement of Science and Art

Publications: Journal Articles

In progress: Gliboff, M.; Sulas, D.; Nordlund, D.; de Quilettes, D. W.; Ginger D. S.; Resonant Auger Spectroscopy of Conjugated Donor-Acceptor Polymers to Compare LUMO Delocalization Effects.

2013: Gliboff, M.; Li, H.; Knesting, K. M.; Giordano, A. J.; Nordlund, D.; Seidler, G. T.; Brédas, J.-L.; Marder, S. R.; Ginger, D. S., Competing Effects of Fluorination on the Orientation of Aromatic and Aliphatic Phosphonic Acid Monolayers on Indium Tin Oxide. *J Phys. Chem C.* **2013**, *117*, 15139-15147

2013: Gliboff, M.; Sang, L.; Knesting, K. M.; Schalnat, M. C.; Mudalige, A.; Ratcliff, E. L.; Li, H.; Sigdel, A. K.; Giordano, A. J.; Berry, J. J.; Nordlund, D.; Seidler, G. T.; Brédas, J.-L.; Marder, S. R.; Pemberton, J. E.; Ginger, D. S., Orientation of Phenylphosphonic Acid Self-Assembled Monolayers on a Transparent Conductive Oxide: A Combined NEXAFS, PM-IRRAS, and DFT Study. *Langmuir***,** *29*, 2166-2174.

2012: Lin, H.-C.; Polaske, N. W.; Oquendo, L. E.; Gliboff, M.; Knesting, K. M.; Nordlund, D.; Ginger, D. S.; Ratcliff, E. L.; Beam, B. M.; Armstrong, N. R.; McGrath, D. V.; Saavedra, S. S., Electron-Transfer Processes in Zinc Phthalocyanine–Phosphonic Acid Monolayers on ITO: Characterization of Orientation and Charge-Transfer Kinetics by Waveguide Spectroelectrochemistry. *J. Phys. Chem. Lett*, *3*, 1154-1158.

Teaching Experience

2009-13: University of Washington, Department of Physics

Head Teaching Assistant: Mentored TAs and wrote exam questions for introductory calculus-based physics for undergraduates I-II.

Guest Lecturer and TA: Electricity and Magnetism I-II; Intermediate Classical Mechanics.

Teaching Assistant: Introductory algebra-based physics for undergraduates I-III (with lab component); Quantum Mechanics I-II;

Private Tutor: Introductory undergraduate-level physics courses.

2008: The Cooper Union for the Advancement of Science and Art, School of Engineering:

Teaching Assistant: Introductory physics with lab component.

Awards and Honors

2013: Department of Energy, Energy Frontier Research Center: Center for Interface Science: Solar Electric Materials Innovative Research Seed Award.

2008: National Science Foundation Research Experience for Undergraduates award, State University of New York at Stony Brook.

Professional Skills and Experience

Synchrotron techniques including soft x-ray spectroscopies, near-edge x-ray absorption fine structure, photoemission spectroscopy, and resonant photoemission and resonant Auger spectroscopies, extended x-ray absorption fine structure, working with ultra-high vacuum systems.

MATLAB, IFEFFIT, Adobe Illustrator, Avogadro, ChemDraw, Igor, awk, gnuplot and Microsoft Office.

Working collaboratively towards large-scale research goals as part of the Center for Interface Science: Solar Electric Materials, an Energy Frontier Research Center funded by the Department of Energy.

Conference Participation: Research Presented

2012 Resonant Photoemission Study of Conjugated Polymers, **Interface-to-face 3**. Oct 23-25.

Resonant Photoemission Study of Conjugated Polymers (poster), **LCLS/SSRL Annual Users' Meeting & Workshops.** Oct 3-6.

Orientation of Phenylphosphonic Acid Self-Assembled Monolayers on a Transparent Conductive Oxide: A Combined NEXAFS, PM-IRRAS, and DFT Study. **Surface Analysis.** June 19-22.

Broader Impacts

"Paws-on-science Husky weekend" Pacific Science Center, 2012.

Appendix D: NEXAFS Studies of Other Self-assembled Monolayers

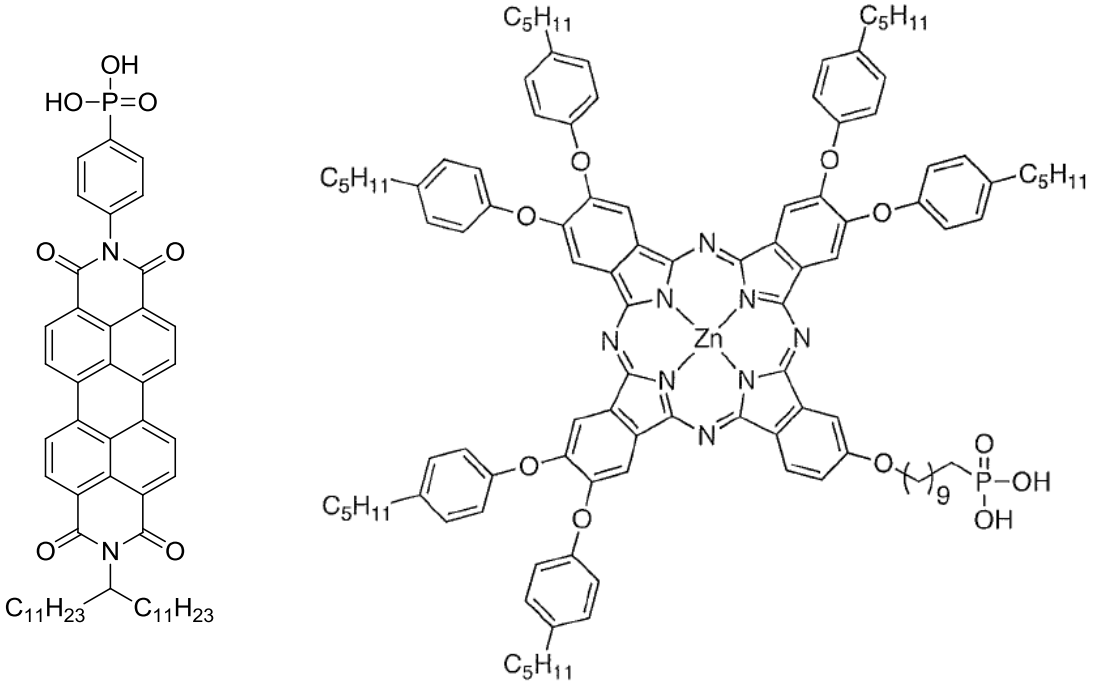

Figure D1. Additional SAMs studied using angular dependent NEXAFS: perylene diimide phosphonic acid(PDI-PA) (Left) and Zn Phtalocyanine-phosphonic acid(ZnPC-PA) (Right).

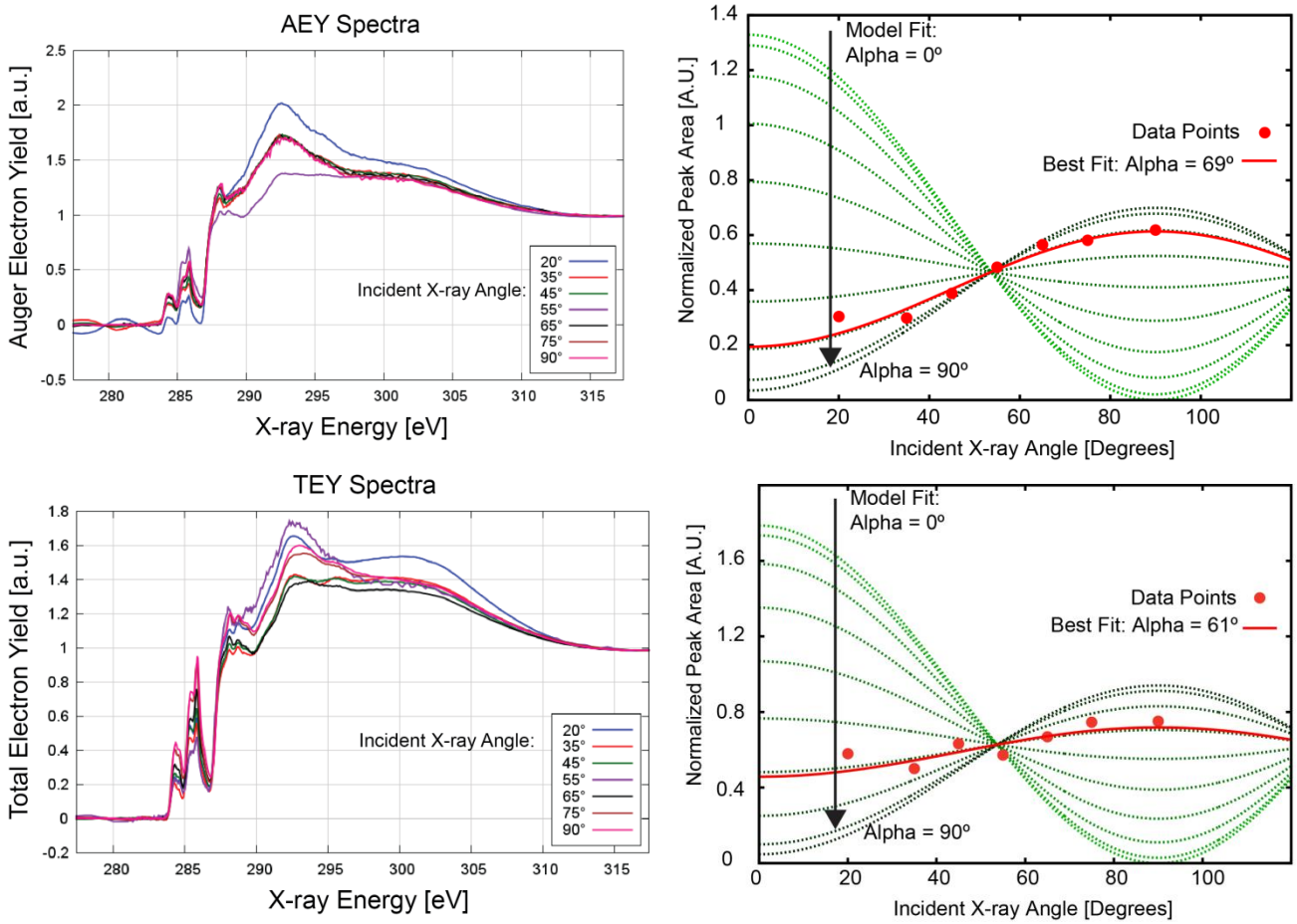

Figure D2. NEXAFS absorption spectra of PDI-PA SAMs. AEY and TEY spectra are shown on the upper left and lower left respectively. Angular dependence is performed on the C=C pi* features from 283 eV to 286.5 eV. The peak intensity for each data collection mode, along with a fit to equation 2.2 are given on the upper right and lower right.

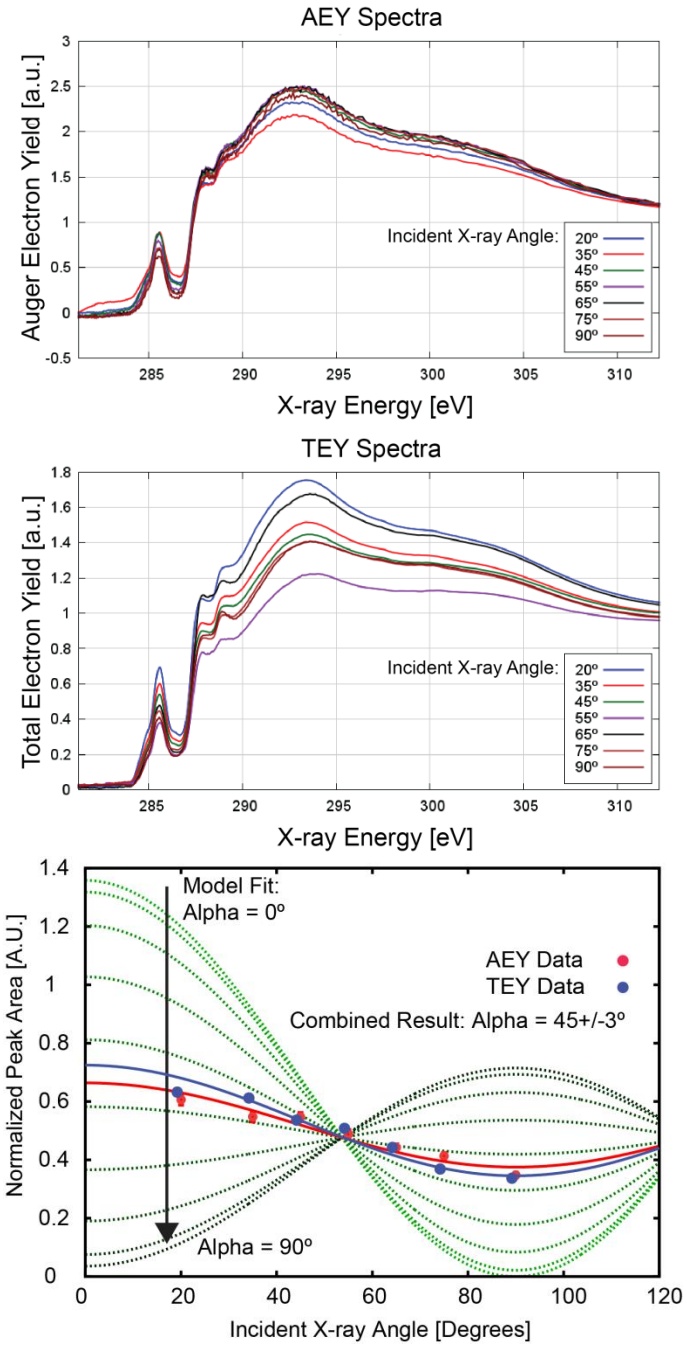

Figure D3. NEXAFS absorption spectra of Zn-(4) PA SAMs. AEY and TEY spectra are shown on the top and middle respectively. Angular dependence is performed on the C=C pi* features from 283 eV to 286.5 eV. The peak intensity for each data collection mode, along with a fit to equation 2.2 is given on the bottom.